First-principles study of the local spin texture in inversion symmetric crystals

Timo Kerremans

Department of Physics
University of Antwerp

Promotor: Prof. B. Partoens

May 2017

Abstract

Spin-baankoppelingseffecten zijn al bekend sinds de opkomst van de kwantummechanica en het belang ervan in kristallijne vaste stoffen werd in de jaren zestig onderzocht. Sindsdien is het algemeen aanvaard dat kristallen zonder inversie symmetrie spin polarisatie vertonen vanwege de spin-baan interactie tussen de elektronen en de ionen van het kristal. Dit effect, waarbij de spinontaarding van de bandenstructuur wordt opgeheven door spin-baan interacties, wordt het Dresselhaus effect genoemd wanneer het zijn oorsprong vindt in de bulk inversie asymmetrie (BIA) en wordt het Rashba effect genoemd wanneer het zijn oorsprong vind in het asymmetrisch zijn van de opsluitingspotentiaal (SIA) van 2D systemen of in heterostructuren. Beide effecten kunnen onderscheiden worden van elkaar doordat ze een eigen zgn. spintextuur hebben. Dit is een patroon dat de richting van de spins van de elektronen maken in de reciproke ruimte van het kristal, wat neerkomt op een vorm van spin-momentum locking waarbij de beweging en spin van een elektron met elkaar gekoppeld worden.

Wanneer naast Dresselhaus spintexturen ook Rashba spintexturen werden waargenomen in bulk materialen, werd duidelijk dat het beeld over spin-baan interacties in vaste stoffen niet compleet was. In 2014 publiceerde Zang et al. een paper waarin ze een nieuwe aanpak voorstellen om spin-baan interacties in vaste stoffen te beschrijven [Nat. Phys. **10**, 387]. Ze gingen uit van het feit dat de spin-baan interactie een lokaal effect is, en dus gekeken moet worden naar de lokale symmetrie van atomen, in plaats van de globale kristalstructuur. Uit deze redenering volgt dat ook in kristallen met inversie symmetrie, zgn. centrosymmetrische materialen, spin polarisatie kan plaatsvinden. Deze spin polarisatie vindt plaats op lokale sectoren in het materiaal die elkaars inversie partners zijn waardoor de richting van de polarisatie tegengesteld is en dus de totale spin polarisatie over het hele materiaal nul is. Deze lokale effecten worden naar analogie met hun bijhorende spintextuur het Dresselhaus-2 en Rashba-2 effect genoemd.

In deze thesis wordt op basis van symmetrie een theoretisch model opgesteld dat de karakteristieke eigenschappen van het D-2 en R-2 effect correct voorspellen. Het model wordt toegepast op twee centrosymmetrische materialen $LaOBiS_2$ en Bi_2Se_3, waarvan de laatste een topologische isolator is. De voorspelde gelokaliseerde spin polarisatie en bijhorende spintexturen worden met behulp van DFT berekeningen geverifieerd in bulk systemen van de overeenstemmende kristallen.

Daarna worden oppervlakken in het systeem in rekening genomen om enerzijds het topologische karakter van Bi_2Se_3 terug te vinden en anderzijds om te kijken of het D-2 en R-2 effect beïnvloed worden door de aanwezigheid van het oppervlak. Uit analyse van de DFT berekeningen blijkt dat aan het oppervlak het D-2 en R-2 effect verdwijnen en plaats

maken voor een netto spin polarisatie. Dit fenomeen is nog niet beschreven in de literatuur en zou heel interessant zijn voor spintronica. Concreet gaat het over centrosymmetrische materialen die in hun bulk lokale, elkaar opheffende spin polarisatie bezitten en aan het oppervlakte gepolariseerde toestanden die spin-momentum locking vertonen.

Tot slot worden toepassingen van de besproken spin polarisatie in spintronica onderzoek besproken en mogelijke voordelen van het R-2/D-2 effect t.o.v. het conventionele R-1/D-1 effect.

Dankwoord

Ik wil Prof. Bart Partoens bedanken voor zijn hulp en inzet als promotor voor deze thesis en wiens enthousiasme mij bij zowel elke vordering als obstakel dat we tegenkwamen wist te motiveren. Met een promotor als Bart zal ik met veel plezier terugdenken aan de vele uren onderzoek en overleg die resulteerden in dit eindwerk.

Mijn opleiding als fysicus zou niet hetzelfde zijn geweest als ik ze niet kon delen met mijn vriendin Ruth. De wandelingen en fietstochten waar je mij op meenam tussen het studeren door kwamen steeds als geroepen en de talloze interessante gesprekken over de leerstof motiveerde me om deze almaar grondiger te begrijpen. Je kritische kijk op de wereld blijft me dagelijks inspireren.

Ik wil ook mijn medestudent en bureaugenoot Andy bedanken voor het delen van zijn interessante gedachtegangen en zijn computer-gerelateerde hulp wanneer ik die nodig had. Hij was er voor de nodige afleiding tijdens lange bureau dagen.

Ik wil ook van de gelegenheid gebruik maken om mijn ouders, broer en zus te bedanken om mij onvoorwaardelijk te steunen en onvermoeid te blijven luisteren naar mijn ideeën en uiteenzettingen over hoe mooi de wereld eigenlijk in elkaar zit.

Als laatst wil ik de proffen bedanken die de opleiding fysica mogelijk maken en die me steeds wisten te boeien over talrijke uiteenlopende takken in de fysica.

Contents

Chapter 1

Introduction

1.1 The current understanding

The phenomenon of spin-orbit coupling between the electron's orbital motion and its spin degree of freedom has been known since Dirac came up with his Lorentz invariant equation of motion for the wavefunction, in 1928. This new interaction explained the extra splitting of the spectral lines that experimentalists observed in spectra of atomic gasses in which the atoms can be considered as free particles. However, it took until the late nineteen fifties before physicists began to understand the effects that spin-orbit interaction in solid state crystals would exhibit on the electronic properties of the material.

In 1955 G. Dresselhaus published the first paper on this matter[1], in which he derived general properties of the Hamiltonian that describes the spin-orbit interaction in crystals. Since then it is known that for crystals without a centre of inversion, spin-orbit coupling results in a lifting of the spin-degeneracy of the electronic bulk states. The lack of an inversion centre is important because if it were present, it follows from time reversal symmetry that the bulk states must be spin degenerate.

Dresselhaus' findings showed that due to bulk inversion asymmetry (BIA), solid state crystals can show spin polarization even in the absence of an external magnetic field.

A few years after Dresselhaus published his paper, Soviet physicist I. Rashba studied spin-orbit effects in two-dimensional crystals in an asymmetric external potential which is referred to as structural inversion asymmetry (SIA)[2]. Also in this case, the spin-orbit effects lead to spin-splitting in the electronic band structure and thus to spin polarization. Rashba derived a Hamiltonian describing the spin-orbit interaction in such systems and the effect he described is called the Rashba-effect.

Since then physicists experimentally verified and expanded on the idea that spin-orbit effects in crystals without a centre of inversion show spin polarization, without the presence of an external magnetic field. A distinction between the Dresselhaus effect and the Rashba effect was maintained, even though both phenomena stem from the same spin-orbit inter-action. The paradigm stated that the Dresselhaus effect occurs in bulk crystals with BIA whereas Rashba effect occurs in two-dimensional crystals with SIA, each with their own characteristics in spin texture.

However, recent experimental results showed that in some bulk materials with BIA, Rashba characteristics were present alongside the Dresselhauss effect[3],[4], which at first could not be explained. These experimental results indicated that the current understanding of spin-orbit effects in crystals was incomplete and the paradigm had to be changed.

Recently Zang et al. published a paper in which they take a different approach to spin-orbit effects in solid states[5],[6]. They put forward a view that starts with the consideration that spin-orbit interaction is a local phenomenon, anchored on the atomic sites of the crystal. Consequently, to understand its effects, they propose to use the local atomic site symmetries of the different atoms in the crystal's unit cell as a starting point, instead of the global space group symmetry. This view not only recovers the known Dresselhaus and Rashba effect in bulk crystals with BIA, but also predicts two hitherto unknown spin-orbit effects that manifest themselves in crystals that possess a centre of inversion, so called centrosymmetric crystals.

These new effects result in spin polarization that is localized on different real space sectors inside the crystal. For crystals with an inversion centre this results in the mutual cancellation of the localized spin polarization when summed over the crystal, making the entire crystal non-spin polarized. This hidden spin polarization has two variants called the Dresselhaus-2 and Rashba-2 effect, according to their global counterparts.

This new and more complete view on spin-orbit effects in solid state materials will be used as the starting point for a theoretical and first-principles study on spin-orbit effects in centrosymmetric materials, conducted in this thesis. Based on simple symmetry principles, a working model for bulk crystals that describes the hidden spin polarization will be derived and tested with DFT calculations on concrete examples.

Then, the effects of surfaces on these bulk effects are studied based on DFT calculations and symmetry properties. The results show that the presence of a surface for materials that show bulk hidden spin polarization leads to materials that exhibit spin polarized currents, without the need of external fields. These materials could be very important for spintronics research.

1.2 Outline of the Thesis

In order not to lose track of the bigger picture, a brief overview of what is covered in this thesis is given beforehand.

In chapter two the theoretical concepts are described in such detail that is needed to understand the nature of the topic under investigation and to set up the theoretical background to build up the model in chapter three. The origin of spin-orbit interaction and the conservative view on its effects in solid state crystals will be covered. Then, in contrast with the latter, a new point of view put forward by Zang et al.[5],[6] is explained and its predictions are contemplated on. The chapter ends with a section about topological insulation because of its intimate connection with spin-orbit effects, which will be studied in later chapters.

In chapter three a general, material independent model is constructed from simple symmetry considerations and which encapsulates both the old and new point of view on spin-orbit effects. By applying the model to two different centrosymmetric crystals with distinct symmetry, $LaOBiS_2$ and B_2Se_3, the hidden spin polarization predicted by Zang et al. is indeed retrieved, together with a prediction on a clear distinction between both bulk crystals based on their atomic site symmetry.

In chapter four and five, the predictions of the model are tested by performing DFT calculations on $LaOBiS_2$ and B_2Se_3 bulk systems. The resulting data is then processed, visualized and interpreted and are compared with the model predictions of chapter three.

Having established the presence of hidden spin polarization in the bulk systems, in chapter six the effects of surfaces are studied to investigate whether they affect the hidden spin polarizations. Specifically for the topological insulator B_2Se_3 the presence of a surface is crucial to reveal its topological character. Since the model of chapter three does not cover surfaces, the analysis in this chapter will be based on DFT results of slab systems and the obtained knowledge about hidden spin polarization in previous chapters.

Chapter seven contains a short description of the most commonly used experimental techniques that are used to observe band structures and spin polarizations. To end this chapter some possible applications of R-2/D-2 materials are speculated. Specifically their advantage over the conventionally used materials in the spintronics research. Very recently and during the writing of this thesis, the first papers on experimental observation of the proposed local, hidden spin polarization have been published[7],[8],[9]. These experimental results will be briefly discussed.

Chapter eight is the conclusive chapter where all the results of this thesis are recapitulated in a short overview.

Chapter 2

Theoretical background

2.1 Spin-Orbit interaction

In 1905 A. Einstein published his paper on Special Relativity which lead to a consistent way of transforming the Maxwell Equations between inertial reference frames. These transformations can be written in what are known as the Bernoulli-Joules equations[10]:

$$\vec{E}' = \gamma(\vec{E} + \vec{v} \times \vec{B}) - (\gamma - 1)(\vec{E} \cdot \vec{v})\hat{e}_v \tag{2.1}$$

$$\vec{B}' = \gamma(\vec{B} - \frac{\vec{v} \times \vec{E}}{c^2}) - (\gamma - 1)(\vec{B} \cdot \vec{v})\hat{e}_v \ . \tag{2.2}$$

Here, the magnetic and electric fields are transformed to a primed, inertial reference frame which has velocity $\vec{v} = |\vec{v}|\hat{e}_v$ and γ is the usual Lorentz-factor: $(1 - v^2/c^2)^{-1}$, with c the speed of light in vacuum.

The situation that will be of importance later in the thesis, is the one where the unprimed reference frame exhibits only an electric field, i.e. $\vec{B} = 0$. It follows from the second Bernoulli-Joules equation that any inertially moving observer will experience in addition to an electric field $\vec{E}'$, a magnetic field $\vec{B}' \sim -\vec{v} \times \vec{E}$ in its own frame of reference.

At the beginning of the quantum revolution, P. Dirac made an educated guess on how a relativistic Schrödinger equation should look like in order to satisfy Lorentz invariance. It turned out to be a working model and the equation became known as the Dirac Equation for charged spin 1/2 particles in an electro-magnetic field[11]:

$$\hat{H}\Psi = \Big[- eV(\vec{r}) + \beta mc^2 + \vec{\alpha} \cdot (c\vec{p} + e\vec{A}(\vec{r}))\Big]\Psi = E\Psi \tag{2.3}$$

In this equation, Ψ is a four component (bi-spinor) wavefunction and correspondingly, β and the components of $\vec{\alpha}$ are 4×4 matrices:

$$\beta = \begin{pmatrix} I_{2\times2} & 0 \\ 0 & -I_{2\times2} \end{pmatrix} \text{ and } \alpha_i = \begin{pmatrix} 0 & \sigma_i \\ \sigma_i & 0 \end{pmatrix} \ , \tag{2.4}$$

where σ_i are the Pauli matrices for $i = x, y, z$:

$$\sigma_x = \begin{pmatrix} 0 & 1 \\ 1 & 0 \end{pmatrix} \ , \sigma_y = \begin{pmatrix} 0 & -i \\ i & 0 \end{pmatrix} \text{ and } \sigma_z = \begin{pmatrix} 1 & 0 \\ 0 & -1 \end{pmatrix} \ . \tag{2.5}$$

To get insight in this equation it is useful to write the bi-spinor Ψ as a two-vector containing two spinors ψ and ϕ as its components. Doing this, the Dirac Equation for Ψ can be written as two coupled equation for ψ and ϕ. By eliminating ϕ and up to first order of v/c, the non-relativistic Schödinger equation, sometimes termed the Pauli equation, can be obtained for ψ:

$$\left[-E' + eV(\vec{r}) - \frac{1}{2m}\left(\vec{p} + \frac{e}{c}\vec{A}\right)^2 - \frac{e\hbar}{2mc}\vec{\sigma}\cdot\vec{B}\right]\psi = 0 \quad , \tag{2.6}$$

where $E' = E + mc^2$ and as usual $\vec{E} = \vec{\nabla}V$ and $\vec{B} = \vec{\nabla}\times\vec{A}$. This equation however, does not contain any useful information about the interaction between the spin of the electron and its motion. To retain the finer working of the spin of the electron, second order terms of v/c must be taken into account. After some more extended calculation, keeping orders up to v^2/c^2, the following equation is obtained:

$$\begin{aligned}\Big[-E' + eV(\vec{r}) - \frac{1}{2m}\left(\vec{p} + \frac{e}{c}\vec{A}\right)^2 + \frac{1}{4m^2c^2}(E' + eV(\vec{r}))^2 + \\ i\frac{e\hbar}{(2mc)^2}\vec{E}\cdot\vec{p} - \frac{e\hbar}{(2mc)^2}\vec{\sigma}\cdot(\vec{E}\times\vec{p}) - \frac{e\hbar}{2mc}\vec{\sigma}\cdot\vec{B}\Big]\psi = 0\end{aligned} \tag{2.7}$$

The first three terms can also be found in the non-relativistic Schrödinger equation. The fourth term is called the mass-velocity term and results in higher order terms in the kinetic energy. The fifth term has no classical analogon and is called the Darwin-term. The last two terms are the only ones that contain the spin-matrices $\vec{\sigma} = (\sigma_x, \sigma_y, \sigma_z)$ and thus are the ones that take the spin of the electron into account. The last term is the Zeeman term, which describes the coupling between the direction of the spin and the external magnetic field and was already present in the Pauli equation.

The term of interest, however, is the sixth term. This term describes the coupling between the spin $\vec{\sigma}$ and $(\vec{E}\times\vec{p})$. Remembering the second Bernoulli-Joules equation (2.2), $\vec{E}\times\vec{p}$ corresponds to an effective magnetic field $\vec{B}'$ that is observed due to Lorentz invariance of the Maxwell Equations. Concretely for this case it is the electron that observes a magnetic field $\vec{B}'$ because it moves in the electric field $\vec{E}$ of the positively charged nucleus to which it belongs. With this in mind, the term can be seen as an additional Zeeman term:

$$-\frac{e\hbar}{(2mc)^2}\vec{\sigma}\cdot(\vec{E}\times\vec{p}) = -\frac{\mu_B}{2mc}\vec{\sigma}\cdot(\vec{E}\times\vec{p}) \sim \vec{\sigma}\cdot\vec{B}' \ , \tag{2.8}$$

where μ_B is the Bohr magneton.

The motion of the electron around the nucleus has an angular momentum associated with it. Thus it should be possible to find a correspondence between its angular momentum and the effective magnetic field. Considering a spherical potential $V(r)$ of the nucleus:

$$\begin{aligned}\vec{\sigma}\cdot(\vec{E}\times\vec{p}) &= -\vec{\sigma}\cdot(\nabla V(r)\times\vec{p}) = -\frac{1}{r}\frac{dV}{dr}\vec{\sigma}\cdot(\vec{r}\times\vec{p}) & (2.9)\\ &= -\frac{1}{r}\frac{dV}{dr}(\vec{\sigma}\cdot\vec{L}) & (2.10)\end{aligned}$$

It is now clear that the spin of the electron couples with its orbital angular momentum around the nucleus, which is the reason why this term in the relativistic Hamiltonian is called the Spin-Orbit coupling term. This spin-orbit interaction (SOI) will play a major role in this thesis, especially the SOI in solid matter crystals, as it is of importance in recent discovered phenomena.

2.2 Spin-orbit interaction in solid matter crystals

In solid matter, electrons move in a periodic crystal structure. The energy levels of the individual atoms in the crystal hybridize due to the interaction between them, which leads to energy bands in the continuum limit. These bands are best depicted in a figure that plots the energy for specific $\vec{k}$-points in reciprocal space, where each $\vec{k}$-point corresponds to an electron state: $E(\vec{k})$.

Based on very general properties that crystals can posses, some characteristics of their band structure can be derived.

Time reversal symmetry
If by changing the arrow of time, i.e. $t \to -t$, the system undergoes no change, it is said to have time reversal symmetry. This is the case when, for example, no external or internal magnetic fields are present. Consider a crystal where time is reversed, then electrons trace back on their own trajectory, i.e. $\vec{k} \to -\vec{k}$ and spin up electrons ($\uparrow$) change their spin direction, becoming spin down electrons ($\downarrow$). The latter is obvious due to the fact that spin is described as an internal angular momentum. Consequently, when time reversal symmetry is present, the energy of an up electron moving in the $\vec{k}$-direction, equals the energy of a down electron moving in the opposite direction. Or

$$\epsilon(\uparrow, \vec{k}) = \epsilon(\downarrow, -\vec{k}) \ . \tag{2.11}$$

This is an expression of Kramer's theorem, which states that if time reversal symmetry is present, for each state $\vec{k}$, another state can be found at $-\vec{k}$ with the same energy but with opposite spin. Throughout this thesis only time reversal invariant systems will be considered.

Inversion symmetry
A crystal is said to have inversion symmetry if the entire crystal structure stays the same under a parity transformation $\vec{r} \to -\vec{r}$ and thus $\vec{k} \to -\vec{k}$. The inversion symmetry of a crystal structure can be reduced to the inversion symmetry of its unit cell and therefore it is sufficient to look only at the unit cell to determine inversion symmetry.

If a crystal has both time reversal symmetry and inversion symmetry it is easy to see that their band structure has the following property:

$$\epsilon(\uparrow, \vec{k}) = \epsilon(\downarrow, -\vec{k}) = \epsilon(\downarrow, \vec{k}) \quad , \tag{2.12}$$

where the second equality follows from spatial inversion symmetry. So the energy bands are spin degenerate and have $E(\vec{k}) = E(-\vec{k})$, meaning they are symmetric around $\vec{k} = 0$ (Γ-point).

2.2.1 Dresselhaus spin-orbit interaction

Consider a material with time reversal symmetry but *without* inversion symmetry, e.g. GaAs (zink blende structure) depicted in figure 2.1. In this case the bands will not be spin degenerate any more, leading to spin split bands which means one band per spin direction. The origin of this spin splitting is the spin-orbit interaction and it can be understood as follows. If the crystal lattice, or equivalently the unit cell, does not have inversion symmetry, then $V(\vec{r}) \neq V(-\vec{r})$. Consequently, an electron moving through the material will feel a potential gradient, which can be described as an electron moving through an electric field. The electron will be subject to a Lorentz transformed magnetic field in its own reference frame with which its spin will interact. This leads to a spin splitting similar to a Zeeman spin splitting of electrons around a nucleus.

The importance of this spin-orbit interaction in the bulk of solid matter was described by G. Dresselhaus in his 1953 paper[1]. He described the spin splitting of the bands, even in the absence of an external magnetic field and constructed an effective Hamiltonian for such materials. The exact form of the Hamiltonian depends on the specific band, but an important general characteristic is

$$\hat{H}_D \sim k^3 \ . \tag{2.13}$$

However, for high symmetric crystals, the cubic dependence can be reduced to a linear dependence, as will be shown further in this thesis.

Since then the spin splitting of bands due to spin-orbit interaction in materials that have bulk inversion asymmetry (BIA), is called the Dresselhaus effect. For reasons to become clear later-on in this thesis, the Dresselhaus effect will be abbreviated as the D-1 effect.

2.2.2 Rashba spin-orbit interaction

Another way to obtain a potential gradient is by considering a quasi two-dimensional material, such as a 2-D electron gas (2-DEG) and confine it by an asymmetric potential. By doing this a potential is obtained that can be expanded to get

$$\begin{aligned} V(\vec{r}) &= V_0 + \vec{\nabla} V(\vec{r}) \cdot \vec{r} + ... \\ &= V_0 - \vec{E}(\vec{r}) \cdot \vec{r} + ... \end{aligned} \tag{2.14}$$

Thus, up to lowest order, the asymmetric potential is characterized by an electric field. This is the field that the electrons feel and consequently experience a Lorentz transformed magnetic field in their own reference frame, leading to spin-orbit interaction. This interaction is present only due to the structural inversion asymmetry (SIA) of the confinement potential.

In 1956 Rashba and Byckov studied this problem and came up with an effective Hamiltonian to describe this spin-orbit interaction[2]:

$$\hat{H}_R = \alpha_R \vec{\sigma} \cdot (\vec{k} \times \vec{E}) \tag{2.15}$$

where α_R indicates the strength of the spin-orbit interaction. This Hamiltonian is similar to the general spin-orbit coupling term in the relativistic Hamiltonian (2.7). What is important to notice is that this general form of the Rashba Hamiltonian is linear in $\vec{k}$, as opposed to its Bulk analogy, $\hat{H}_D$. However, as mentioned before the latter can be reduced to a linear in $\vec{k}$ Hamiltonian if the symmetry of the bulk crystal is high enough.

The Rashba-Byckov Hamiltonian is also used to describe spin-orbit interaction at surfaces, since here the surface itself brings about a potential gradient. This spin-orbit interaction effect, will be called the R-1 effect to contrast it with the D-1 effect.

2.2.3 GaAs compound as example of band spinsplitting

The phenomenon of how spin-orbit interaction lifts spin degeneracy of the band structure will now be illustrated by a DFT calculation for the band structure of GaAs. This semi-conductor has the zinkblende crystal structure which has no center of inversion and is depicted in figure 2.1.

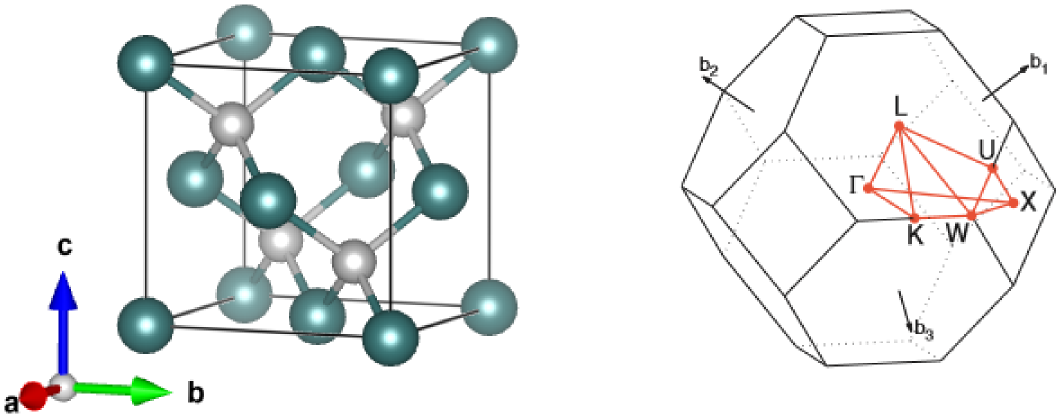

Figure 2.1: The GaAs zink blende (FCC cubic) crystal structure on the left and its corresponding first Brillouin zone on the right.

The band structure of GaAs is calculated both without spin-orbit interaction and with spin-orbit interaction. Later in this thesis more details on the DFT-formalism will become clear as it will be used to great extend. The result of the calculation is shown in figure 2.2.

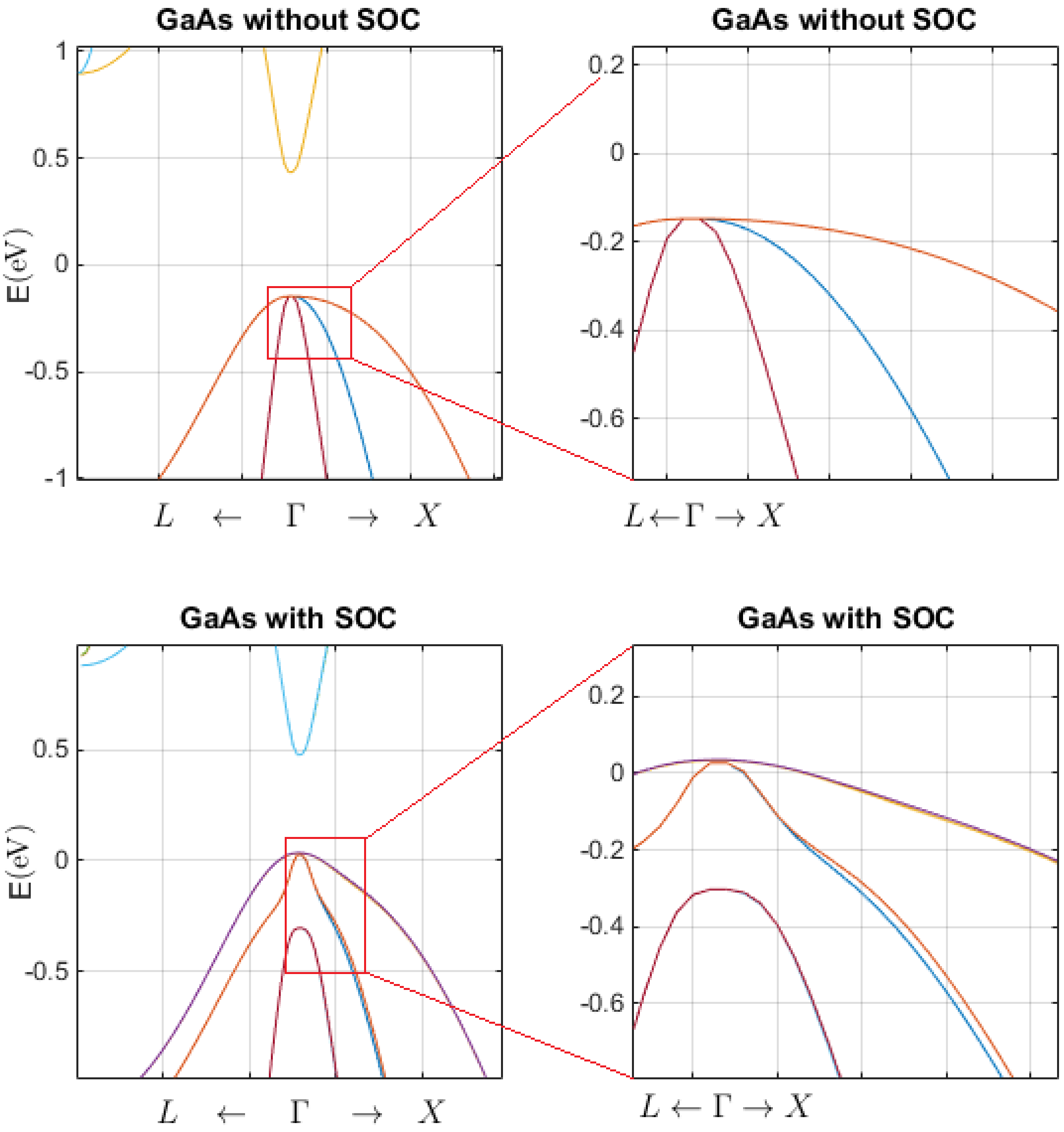

Figure 2.2: DFT calculated band structure of GaAs without (upper panel) and with spin-orbit coupling (lower panel).

From the previous figure it is clear that the degenerate bands indeed show splitting. However, it is important to realize that even though the large splitting at the Γ-point is due to spin-orbit interaction, it is not the spin degeneracy that is lifted here. Instead, this splitting has to do with the lifting of the orbital degeneracy which is a consequence of lowering the symmetry of the system due to spin-orbit interaction. This effect is similar to the atomic case where spin-orbit coupling lifts the orbital degeneracy due to the fact that the coupling between spin and orbital motion in a sense reduces the isotropy of the orbitals.

The two valence bands closest to the Fermi energy level in figure 2.2 are called the light-(upper) and heavy-(lower) hole bands. The band that is completely split off at the Γ-point is called the spin-orbit split off band. Even though the GaAs contains no inversion centre, the spin split bands have to remain degenerate in the $\vec{k} = 0$ (Γ)-point since this is a time reversal invariant point (2.11). These band splittings are very small and can only be seen when zoomed in around the Γ-point, depicted in the right panels of figure2.2. In a recent paper by F. Jaroslav et al. first-principles studies are performed in detail on the small spin splitting in GaAs-type materials[12] resulting in similar splittings as seen in figure 2.2.

2.2.4 Spin textures as fingerprint of D-1 and R-1

Both the D-1 and R-1 effects are characterized by their unique spin texture[13]. These are typical patterns the directions of the electrons' spin make in reciprocal $\vec{k}$-space. This means that for each state with given crystal-momentum $\vec{k}$ a specific spin direction is associated. The vector field obtained by the spin directions of all the $\vec{k}$-states in reciprocal space then form a pattern, which is called the spin texture of the crystal.

In this way, the presence of spin-orbit interaction in the form of D-1 and/or R-1 can be experimentally established by measuring the spin textures inside a material by means of spin-resolved ARPES, cfr chapter 7. On the other hand, the spin-orbit formalism can be used to predict specific spin textures and their strength in certain materials. This can lead to material design principles for the experimentalists to fabricate spin polarized materials, which are needed in various domains such as the research for spintronics[14].

In figure 2.3 the typical spin textures in reciprocal space of both Dresselhaus (a) and Rashba (b) effect are shown. Later on, these spin vector fields will be derived starting from a Hamiltonian that is constructed from general symmetry principles.

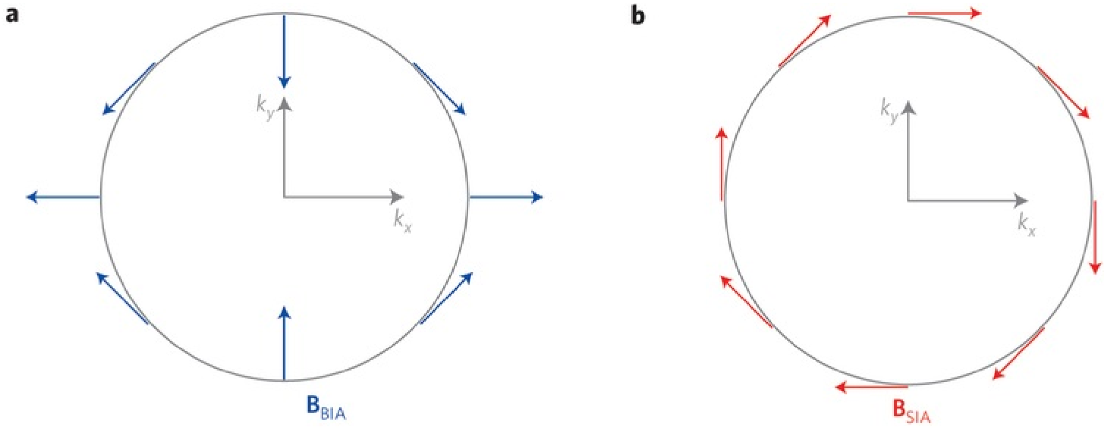

Figure 2.3: Spin textures in solid state matter due to spin-orbit interaction[13], manifested as the Dresselhaus effect (left) and the Rashba effect (right).

2.2.5 Remarks on the D-1 and R-1 classification

The distinction between the D-1 effect due to BIA and the surface R-1 effect due to SIA seems justified by the different nature of their spin textures. However, they both originate from the presence of a net potential gradient felt by the electrons, be it inside the bulk (BIA) or due to an external potential (SIA). Moreover, recent experimental studies have detected Rashba spin textures, as shown in figure 2.3, inside the bulk of layered materials[3],[4], showing that the Rashba effect is not limited to surface inversion asymmetry (SIA).

These observations show that the long standing model for spin-orbit effects in solid matter is not in agreement with experiment and that the overall understanding is not complete. This lead Zang et al. to create a new theory that unites the different spin textures in solid matter[5],[6]. By reconsidering the origin of the spin-orbit effects, they managed to construct a picture that not only explains the bulk R-1 effect but also predicts two new spin-orbit effects that were previously overlooked. This thesis will build upon this new way of looking at spin-orbit effects in solid matter.

2.3 Spin-orbit effects in centrosymmetric materials

Up until recently the paradigm concerning spin-orbit interaction was that this effect only came into play for materials without inversion symmetry[15]−[19]. Since for inversion symmetric materials $V(\vec{r}) = V(-\vec{r})$ holds and the electron will not feel a net potential gradient (or electric field) to interact with. As shown (2.12), this leads to spin degeneracy and more importantly, no net spin polarization that could be used for applications such as spintronics.

In 2014 Zang et al. published a paper where they put forward a more accurate picture to describe the different spin-orbit effects[5]. Their insight was that since spin-orbit interaction is a local effect, anchored on the atoms constituting the crystal, one should consider the atomic site symmetry instead of the crystal space group symmetry as a whole. Each set of atoms will thus have their own spin-orbit effects and the total spin-orbit spin texture will be the vector sum of the spins over the whole unit cell.

This new paradigm leads to a new, more accurate and unified classification of spin-orbit effects in solids, based on the atomic site symmetries, rather than on those of the unit cell. The different cases of spin-orbit effects that can occur in crystals will be discussed next and are schematically depicted in figure 2.4.

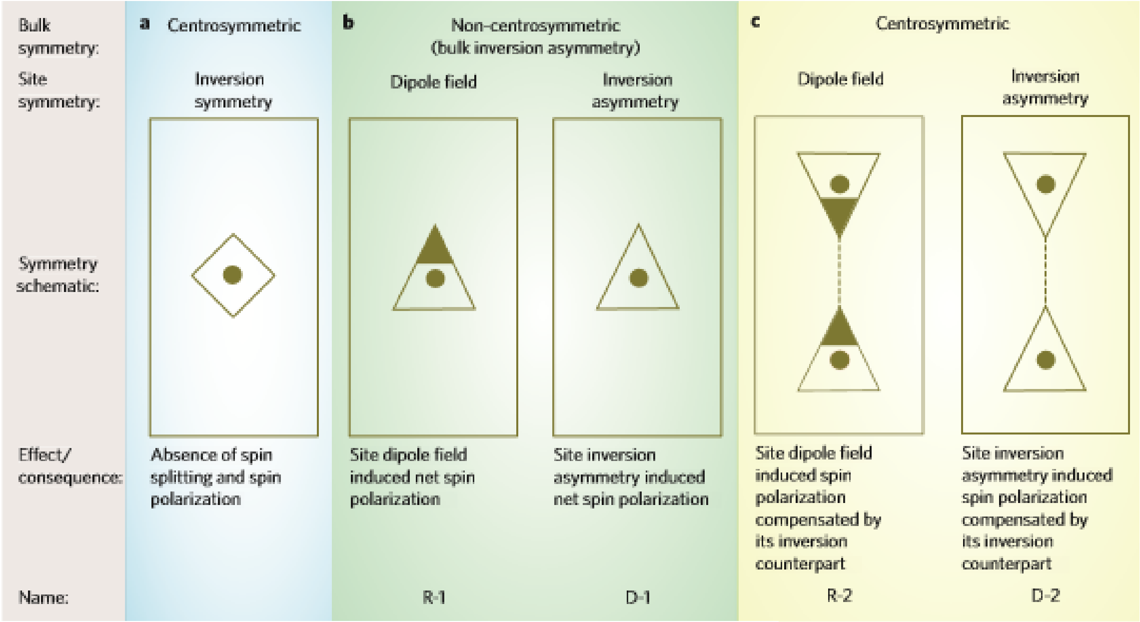

Figure 2.4: A schematic representation of the different symmetries a unit cell can have[5]. Blue, green and yellow indicate the space group symmetry of the unit cell, respectively centrosymmetric, non-centrosymmetric and centrosymmetric. The icons inside the rectangles represent the atomic site symmetry. Until recently only materials exhibiting the D-1 and R-1 effect were considered as spin polarized materials. The new approach to layered materials shows that D-2 and R-2 effects can also occur under the form of hidden, localized spin polarization.

2.3.1 Centrosymmetric unit cell with inversion symmetric atomic sites

When all the atomic sites have inversion symmetry, then the electrons will not feel a net potential gradient, disabling the possibility of spin-orbit effects for the atomic sites. Consequently, summing over atomic sites to obtain the total spin polarization of the crystal does not result in band spin-splitting and thus no net spin polarization. This case is schematically depicted in figure 2.4, a

Atomic sites with an inversion point are: $C_i, C_{2h}, D_{2h}, C_{4h}, D_{4h}, S_6, D_{3d}, C_{6h}, D_{6h}, T_h, O_h$. Here shönflies notation is used, the corresponding stereographs can be found in appendix I.
A centrosymmetric unit cell can be for example R$\bar{3}m$.

2.3.2 Non-centrosymmetric unit cell with inversion asymmetric atomic sites

When there is at least one atomic site present which has no inversion symmetry, electrons will experience spin-orbit interaction due to the induced potential gradient and spin polarization on these sites will occur. If in addition the unit cell is not centrosymmetric, then summing the spins of all the atomic sites will yield a non-zero result. The spin degeneracy of the bands will be lifted resulting in spin-split bands, which leads to a net spin polarization. This case can be identified with the Dresselhaus effect (D-1). This is consistent with previous experiments, since without BIA, the sum over atomic sites will not yield a non-zero result.

An additional restriction has to be made here, to contrast with the next case. Materials will show a pure D-1 effect only if none of the atomic sites induces a polar field. Such a field is made possible if there is a unique anisotropic axis or direction present in the unit cell. This case is depicted in figure 2.4, b, right panel.

Atomic sites without inversion and non-polar are: $D_2, D_3, D_4, D_6, S_4, D_{2d}, C_{3h}, D_{3h}, T, T_d$ and O. A non-centrosymmetric unit cell can be for example F$\bar{4}$3m.

2.3.3 Non-centrosymmetric unit cell with polar atomic sites

This case is very similar to the previous case, with the only difference that now at least one atomic site must have an induced polar field due to an unique anisotropic axis[6]. This polar field results in a potential gradient that can be compared to the one at the surface of the material. This is why the presence of such a polar field can be associated with the Rashba effect. However, when summing over all the atomic sites the dipoles can either add up to zero, leading to a pure D-1 effect, or result in a non-zero dipole field, leading to the R-1 effect. Note that the R-1 effect is consequently always accompanied by a D-1 effect. This case is depicted in figure 2.4, b, left panel.

Atomic sites without inversion and with an induced polar field: $C_1, C_2, C_3, C_4, C_6, C_{1v}, C_{2v}, C_{3v}, C_{4v}$ and C_{6v}.

2.3.4 Centrosymmetric unit cell with inversion asymmetric atomic sites

In the latter two cases the non-centrosymmetric unit cell ensures that the asymmetry of the atomic sites gets translated to the whole crystal structure, leading to the already known D-1 and R-1 effects. However, the new paradigm that Zang et al. propose allows for two new situations that translate to hitherto unknown effects.

Consider the case where the unit cell is centrosymmetric and at least one atomic site lacks an inversion point. This combination is only possible if the asymmetric atomic site has an inversion partner so that taken together, they are inversion symmetric, leading to a centrosymmetric unit cell. This means that an electron can feel a potential gradient localized on a specific atomic site, leading to spin-orbit effects. However, when summed over all the atomic sites, the spin-orbit effects of one atomic site are cancelled by the spin-orbit interaction that an electron feels at the inversion partner. Consequently, even though the material has *localized* spin textures and polarization, these add up to zero when the whole crystal is considered. This is why these mutually cancelling spin-orbit effects are often called hidden spin-orbit effects[13].

If all the atomic sites are non-polar the effect described will be called the D-2 effect, in analogy with D-1. The atomic sites that facilitate the D-2 effect are evidently the same as the ones for the D-1 effect. This case is depicted in figure 2.4 ,c, right panel.

2.3.5 Centrosymmetric unit cell with polar atomic sites

This case is again very similar to the previous case. In addition to a centrosymmetric unit cell and asymmetric atomic sites that have inversion partners, at least one of the atomic sites allows for a net polar field. As with the R-1 effect, two situations can occur when summing over the atomic sites. Either the atomic site polar fields add up to zero, resulting in a pure D-2 effect, or the polar fields do not add up to zero, which will accordingly be called the R-2 effect.

Just as with the D-2 effect, the atomic site symmetries that allow for the R-2 effect are the same that can facilitate the R-1 effect. This case is depicted in figure 2.4 c, left panel.

2.4 Hidden localized spin polarization

According to (2.12), the band structure of D-2 and R-2 materials are spin degenerate due to the centre of inversion and time reversal symmetry. However, even though the bands are not spin split, different spin polarizations are localized on different places in the crystal. Being spatially separated from each other, on a point-by-point basis they will not cancel each other. Only when the crystal as a whole is considered it will look as if there is no spin polarization. These are local effects are to be expected since they stem from spin-orbit interaction, which is itself a local phenomenon.

This qualitative discussion shows that localized spin polarization is present in centrosymmetric materials. This means that a whole class of materials that have been overlooked in the research for spin polarized materials are now ready to experiment on. Moreover, materials that were thought to be non-spin active, such as the centrosymmetric Silicon crystal, should indeed show hidden spin-polarization[5].

2.5 Topological Insulation

Topological insulation is a new quantum state that solid matter can exhibit which has been an increasingly promising topic in solid state research. Materials that possess such states are called topological insulators and do not belong to the class of insulators, conductors or semi-conductors. Instead, topological insulators act like insulators in their bulk but have conducting surface states. Moreover, these surface states are very robust in the way that they are topologically protected. The latter means that to create or eliminate the presence of such surface states something fundamental has to change, much in the same way as to deform a sphere into a torus, the sphere has to be punctuated.

In terms of solid state theory, topological insulators have a band structure which is schematically depicted in figure 2.5. It shows that only two single channel bands close the band gap and cross each other at the Fermi energy level, forming what is called a Dirac cone. The conducting states that are associated with the Dirac cone are localized at the surface (edge) of the three-(two-)dimensional material, making them conducting surface states.

The robustness of these states comes from the fact that they are topologically protected by the presence of time-reversal symmetry, which remains present in many circumstances. This means, in analogy with the sphere-torus transition, that the conducting surface states will be present as long as time-reversal symmetry in the system holds.

Another well known phenomenon in topological insulators is that the conducting (surface) electron states have their spin and crystal momentum locked to each other, which is referred to as spin-momentum locking. This means that each of the two conducting channels that bridges the band gap has its own preferred spin direction. Since the crystal momentum k is proportional to $\frac{\partial E}{\partial k}$, it is clear that one spin direction is connected to one conducting channel, as seen in figure 2.5. Spin-momentum locking in topological insulators results in spin polarized surface currents, which is a much wanted property concerning spintronics.

The spin-momentum locking in many topological systems indicates that spin-orbit interactions play a crucial role in the formation of the topological surface states. As discussed, spin-orbit interactions couple the orbital motion of the electron to its spin. In the next part of the thesis, it is shown that spin-orbit interaction in layered crystals with strong interlayer coupling exhibit a band inversion. This means that the valence or conduction band have their curvature inverted around a time-symmetric point, figure 5.2, section 5.1.1. This band inversion is seen as one of the defining properties of topological insulators and is directly coupled to spin-orbit interactions.

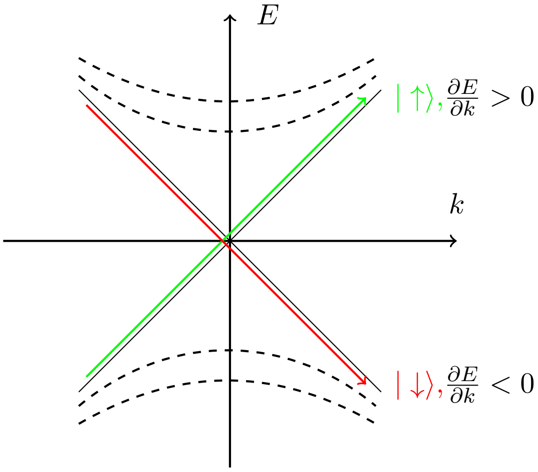

Figure 2.5: Schematic representation of the band structure of a topological insulator. The dashed bands are the insulating bulk bands that exhibit a band gap. The single channel conducting bands form a cone and associated with states that are localized on the surface of the material. The spin-momentum property is made visible with the different colors.

Because spin-orbit effects play a fundamental role in the existence of topological insulation, it is interesting to look at the topological surface states together with the discussed local spin effects which are both a consequence of spin-orbit interaction. This analysis will be based on first-principles calculations and will give more insight in both phenomena present in layered topological insulators.

First, however, in the next chapter of this thesis the new, hidden spin-orbit effects are investigated by constructing an effective Hamiltonian based on atomic symmetry that should both capture the D-2 and R-2 effect in layered materials. First- principles studies on the model predicted spin textures of compounds LaOBiS2 and the topological insulator Bi2Se3 will show a very clear signature of these hidden spin-polarization.

Chapter 3

Model Hamiltonian for D-2 and R-2 materials

In this chapter a working model will be derived to investigate the discussed hidden spin polarization under the form of both the D-2 and R-2 effect. To do this, first a Hamiltonian that describes the D-1 and R-1 will be constructed based on general non-centrosymmetric symmetries (BIA). It will be used to obtain the typical spin textures that arise from these spin-orbit effects. Afterwards this Hamiltonian is used to describe the spin-orbit interaction in a single atomic layer without an inversion centre, leading to D-1 and R-1 effects. Then a bulk crystal will be constructed by putting these single atomic layers on top of each other in such a way that the crystal becomes centrosymmetric. Consequently the D-1 and R-1 effects vanish but depending on the coupling between the layers, localized spin textures should still be present.

Such a model for layered materials has already been partially constructed for the $\mathrm{LaOBiS_2}$ compound by Zang et al.[6] However, even though their predicted spin textures are in agreement with the DFT calculations for the valence band, it does not predict anything about the conduction band nor is it based on general symmetry principles.

The model constructed here will address this incompleteness by starting from very general symmetry properties, laying at the base of the compensating D-2 and R-2 effects. The model will then be used to study layered materials with weak coupling, such as $\mathrm{LaOBiS_2}$ and strong coupling, such as $\mathrm{Bi_2Se_3}$, to investigate whether localized spin textures are present in the form of D-2 and R-2 effects.

3.1 General Hamiltonian for C_{2v} symmetry

As discussed, because a polar atomic site symmetry always implies site asymmetry (see figure 2.4), the R-1 effect will always be accompanied by the D-1 effect. This is why it is sufficient to search for a model that obeys R-1 conditions. The R-1 effect is expected to originate from atomic sites in the crystal that have a point symmetry group which allows for a net polar field on that site. A general, low symmetry point group that satisfies this condition is C_{2v}. This symmetry group consists of a rotation about the z-axis over 180° and two perpendicular mirror planes along the xz- and yz-plane. The z-axis is the unique anisotropic axis that facilitates the polar field. A graphical representation of symmetry point groups can be found in appendix I.

The lowest order Hamiltonian that is invariant under the C_{2v} symmetry operations, and that describes the spin-orbit interaction, can be written down as

$$H_{SO} \sim (\alpha x^2 + \beta y^2) \times z \quad , \tag{3.1}$$

which can be easily checked, with α and β constants of proportionality. This Hamiltonian can be rewritten by considering that the following quantities transform in the same manner under reflection and rotation:

$$\begin{aligned} k_x &\sim x \\ k_y &\sim y \\ \sigma_x &\sim yz \\ \sigma_y &\sim -xz \end{aligned} \tag{3.2}$$

The first two assertions are true because k_x and k_y are polar vectors. The last two can be verified by noting that spin, $\sigma_{x,y}$, is an angular momentum and should transform like a pseudovector, just like orbital angular momentum $L_{x,y}$. On its turn, L_x transforms like $p_y z$, which in turn transforms like yz. A more satisfying explanation for the last two equivalences in transformation goes as follows.

Because both spin and orbital angular momentum are pseudovectors, they should transform in the same manner under rotations and reflections. Thus, to understand how spin transforms, it is necessary to calculate how orbital angular momentum transforms under rotation.

The components of the $\vec{L}$ pseudovector, L_x and L_y, transform like normal vectors under rotations. This means it transforms under the rotation matrix

$$R(\theta) = \begin{pmatrix} \cos(\theta) & -\sin(\theta) \\ \sin(\theta) & \cos(\theta) \end{pmatrix} \quad , \tag{3.3}$$

which leads to the following transformation relations

$$\begin{cases} L_x^R = L_x \cos(\theta) - L_y \sin(\theta) \\ L_y^R = L_x \sin(\theta) + L_y \cos(\theta) \end{cases}$$

where the z-component of $\vec{L}$ remains the same, as should be under rotation about the z-axis. For xz and yz, the normal coordinate rotation transformation holds, giving

$$\begin{cases} (xz)^R = (x \cos(\theta) - y \sin(\theta))z \\ (yz)^R = (x \sin(\theta) + y \cos(\theta))z \end{cases}$$

Here, the z-coordinate again remains the same after rotation.

If both transformations are to be compared, the relation between both $L_{x,y}$ and x, y should be taken into account. From its definition $\vec{L} = \vec{r} \times \vec{p}$, it follows that $\vec{L} \perp \vec{r}$. Thus both vectors can be rotated into each other by the following rotation

$$\begin{pmatrix} L_x \\ L_y \end{pmatrix} = \alpha \begin{pmatrix} \cos(\varphi) & -\sin(\varphi) \\ \sin(\varphi) & \cos(\varphi) \end{pmatrix}_{\varphi=\frac{\pi}{2}} \begin{pmatrix} x \\ y \end{pmatrix} = \alpha \begin{pmatrix} -y \\ x \end{pmatrix} \quad , \tag{3.4}$$

with α a proportionality constant. This relation can be used to substitute in the transformation formulas for L_x and L_y:

$$\begin{cases} L_x^R = L_x\cos(\theta) - L_y\sin(\theta) = -\alpha(y\cos(\theta) + x\sin(\theta)) \\ L_y^R = L_x\sin(\theta) + L_y\cos(\theta) = \alpha(x\cos(\theta) - y\sin(\theta)) \end{cases}$$

From these expressions it is now very clear that, for $\alpha < 0$, indeed L_x and L_y transform like resp. yz and $-xz$ under rotation about the z-axis over an angle θ. Finally, as mentioned before, since spin $\vec{\sigma}$ and orbital angular momentum $\vec{L}$ are both angular momenta, they should transform in the same way under rotations. This results in the transformations for σ_x and σ_y in (3.2).

Having established the transformation equivalences, they can be substituted in H_{SO}, leading to the following expression:

$$H_{SO} \sim (-\alpha k_x\sigma_y + \beta k_y\sigma_x) \quad . \tag{3.5}$$

It can be easily checked by matrix multiplication that this expression is indeed invariant under all the symmetry operation of the C_{2v}-symmetry group.

The Hamiltonian can be further written in its symmetric and antisymmetric part with respect to interchanging x and y:

$$\begin{aligned} H_{SO} &\sim \frac{1}{2}(-\alpha+\beta)(k_x\sigma_y + k_y\sigma_x) + \frac{1}{2}(-\alpha-\beta)(k_x\sigma_y - k_y\sigma_x) \\ &= \gamma_D(k_x\sigma_y + k_y\sigma_x) + \alpha_R(k_x\sigma_y - k_y\sigma_x) \end{aligned} \tag{3.6}$$

From this final expression it is clear that the total spin-orbit Hamiltonian for a general C_{2v} system, can be written as the sum of two symmetrically inequivalent parts.

The first term is invariant under the symmetries of the D_{2d} point group, appendix I, which is non-polar. Because D_{2d} does not allow for a net polarization on the atomic site, this term cannot be attributed to the Rashba effect. Instead, it must originate from the Dresselhaus effect. The proportionality constant γ_D is accordingly called the Dresselhaus constant. This shows that indeed based on symmetry, the R-1 effect is always accompanied by the D-1 effect.

It is worth to note here that in literature the Dresselhaus Hamiltonian is often written as[14],[15] $H_D \sim (k_x\sigma_x - k_y\sigma_y)$ instead of (3.6). This form can be obtained from the symmetric part of the Hamiltonian in (3.6), by performing a unitary transformation

$$U = \begin{pmatrix} 1 & 0 \\ 0 & i \end{pmatrix}$$

on σ_x and σ_y, which gives $U\sigma_x U^\dagger = \sigma_y$ and $U\sigma_y U^\dagger = -\sigma_x$, connecting both forms.

The second term in (3.6) is invariant under the symmetries of the C_{4v} point group which does allow for a net polarization, appendix I. It follows that this term is attributed to the Rashba contribution of the spin-orbit interaction. Thus, α_R is accordingly called the Rashba constant.

The extend to which both terms are present in the real H_{SO} (3.6) is highly material and band dependent and should be determined by experiment or detailed analysis of first-principle calculations. A good signature of the degree in which both are present is the spin texture that the material exhibits. For instance, when a pure helical spin texture is present, γ_D will be negligible and only the Rashba term will contribute according to figure 2.3.

These spin textures belonging to both effects can now be derived by calculating the eigenvalues and corresponding eigenvectors for $H_{tot} = H_{kin} + H_{SO}$, where H_{kin} corresponds to the kinetic energy, by means of diagonalizing the Hamiltonian matrix:

$$\begin{aligned} H_{kin} + H_{SO} &= \begin{pmatrix} \epsilon_k & \gamma_D(k_y - ik_x) - \alpha_R(k_y + ik_x) \\ \gamma_D(ik_x + k_y) + \alpha_R(-k_y + ik_x) & \epsilon_k \end{pmatrix} \\ &= \begin{pmatrix} \epsilon_k & -i\gamma_D k e^{i\varphi} - i\alpha_R k e^{-i\varphi} \\ i\gamma_D k e^{-i\varphi} + i\alpha_R k e^{i\varphi} & \epsilon_k \end{pmatrix} \quad , \end{aligned} \tag{3.7}$$

where $H_{kin} = \epsilon_k I_{2\times2}$ with ϵ_k the energy of the mean field single particle energies of the electron without the presence of spin-orbit coupling. This leads to the eigenenergies

$$E_\pm = \epsilon_k \pm k\sqrt{\gamma_D^2 + \alpha_R^2 - 2\gamma_D\alpha_R\cos(2\varphi)} \tag{3.8}$$

and corresponding eigenstates

$$\psi_\pm = \begin{pmatrix} \pm\frac{i(\gamma_D e^{i\varphi} + \alpha_R e^{-i\varphi})}{\sqrt{(\gamma_D^2 + \alpha_R^2 - 2\gamma_D\alpha_R\cos(2\varphi)}} \\ 1 \end{pmatrix} \tag{3.9}$$

It is clear that for the general case, both Dresselhaus and Rashba effects are present and couple with each other. To confirm the initial claim that γ_D and α_R indeed indicate the Dresselhauss and Rashba terms, the spin texture of the above eigenstates is now calculated in the limiting cases where one of the two parameters goes to zero.

Rashba limit: $\gamma_D \rightarrow 0$

The eigenstates and eigenenergies become

$$\psi_\pm = \begin{pmatrix} \pm i e^{-i\varphi} \\ 1 \end{pmatrix} \quad , E_\pm = \epsilon_k \pm \alpha_R k \quad . \tag{3.10}$$

The spin texture can be easily obtained by calculating the expectation values of the spin operator: $\langle \psi_\pm \mid \sigma_{x,y,z} \mid \psi_\pm \rangle$, giving

$$\begin{aligned} \psi_+ \quad &: \quad \langle\sigma\rangle_+ = \begin{pmatrix} \sin(\varphi) \\ -\cos(\varphi) \\ 0 \end{pmatrix} \\ \psi_- \quad &: \quad \langle\sigma\rangle_- = \begin{pmatrix} -\sin(\varphi) \\ \cos(\varphi) \\ 0 \end{pmatrix} \end{aligned}$$

The results show helical spin texture which typical for a pure Rashba effect. The spin texture for the ψ_- eigenstate is depicted in figure 3.1, left.

Dresselhauss limit: $\alpha_R \to 0$
The eigenstates and eigenenergies become

$$\psi_\pm = \begin{pmatrix} \pm i e^{i\varphi} \\ 1 \end{pmatrix} \quad , E_\pm = \epsilon_k \pm \gamma_D k \quad . \tag{3.11}$$

The spin texture can, again, be easily obtained by the same procedure as before, giving

$$\begin{aligned} \psi_+ \quad &: \quad \langle\sigma\rangle_+ = \begin{pmatrix} -\sin(\varphi) \\ -\cos(\varphi) \\ 0 \end{pmatrix} \\ \psi_- \quad &: \quad \langle\sigma\rangle_- = \begin{pmatrix} \sin(\varphi) \\ \cos(\varphi) \\ 0 \end{pmatrix} \end{aligned}$$

This spin texture can be seen as a fingerprint of a pure Dresselhauss effect and for the ψ_- eigenstate is depicted on figure 3.1, right.

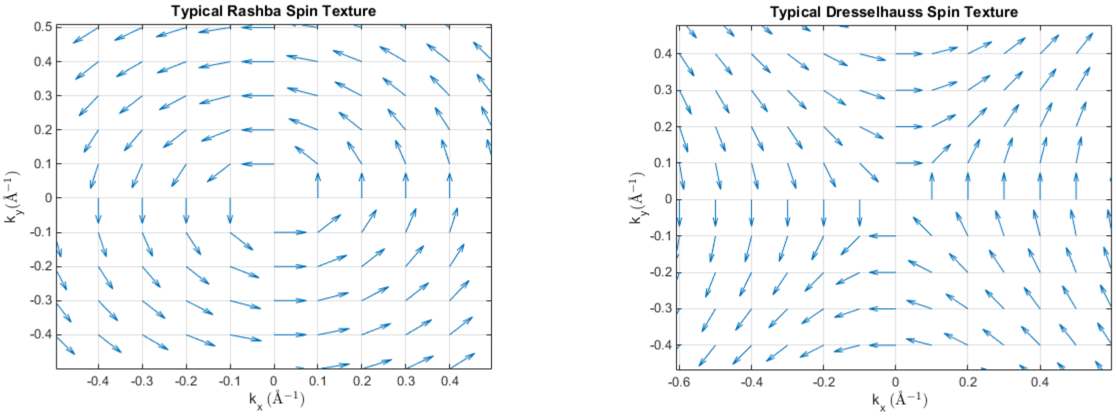

Figure 3.1: Two typical spin textures of the Rasbha (left) and Dresselhaus (right) effect. In the most general case, both are present and the resulting spin texture will be a mixture of both. These spin textures can give a hint of which effect is dominant in a given material.

3.2 General Hamiltonian for C_{3v} symmetry

Another low and general symmetry is C_{3v}. Whereas C_{2v} represented even (two- or four-fold) symmetry, C_{3v} represents three- or six-fold symmetry which are both very distinct symmetry classes. Because many crystals have trigonal or hexagonal unit cells, it is worth also considering C_{3v} symmetry.

Thus a Hamiltonian that describes materials that belong to this symmetry group will be constructed. It will turn out that only a small modification of the C_{2v} Hamiltonian (3.6) is needed in order to make it C_{3v} invariant. C_{3v} is a polar symmetry group which consists of rotations over $3\pi/2$ along the unique anisotropic axis together with three mirror planes parallel to this axis and at an angle of $3\pi/2$ to each other. The stereograph of this symmetry group is shown in appendix I.

In the case of C_{3v} symmetry, x^2 and y^2 are not separately invariant under all C_{3v} symmetry operations (as was the case for C_{2v}). Instead only combinations of $(x^2 + y^2)$ and z are left invariant. This can be understood by considering that rotations and mirror planes through the origin leave planar square distances invariant. These assertions are verified by the character table of the C_{3v} symmetry group, found in many group theory books[20].

Knowing this, the only modification that the C_{2v} Hamiltonian (3.6) needs is $\alpha = \beta$ in order to make it C_{3v} invariant:

$$H_{SO} \sim \alpha(x^2 + y^2) \times z \quad . \tag{3.12}$$

From here on, the same reasoning can be done as for the C_{2v} case. Now, however, since $\alpha = \beta$ only the Rashba-term will remain, leading to the following spin-orbit interaction Hamiltonian

$$H_{SO} = \alpha_R(k_x\sigma_x - k_y\sigma_y) \quad . \tag{3.13}$$

Consequently, this model states that in materials in which atomic sites have C_{3v} symmetry only Rashba spin textures are present and Dresselhaus spin-orbit interaction is not allowed, which is a clear falsifiable prediction.

3.3 Modelling of the LaOBiS$_2$ crystal

Now that a general Hamiltonian to describe D-1 and R-1 spin orbit interaction is constructed, it can be used to derive a model that predicts the hidden spin polarization in layered materials. To illustrate the existence of the D-2 and R-2 effect in a real system, the model will be used to describe the spin-orbit interaction in the layered material LaOBiS$_2$. The model Hamiltonian, that will be based on (3.6) should show that even though the energy spectrum is spin degenerate, these opposite spins are nonetheless spatially localized on different real space sectors, which are inversion partners.

LaOBiS$_2$ is a layered material with symmetry space group P4/nmm, making it an inversion symmetric material with a unique anisotropical axis along the z-direction, which facilitates a local polar symmetry group. Figure 3.2 shows the crystal structure of the LaOBiS$_2$ crystal. Here, the purple, yellow, green and red atoms respectively stand for Bi(C_{4v}), S(C_{4v}), La(C_{4v}) and O(S_4), where atomic site symmetry groups are stated within parentheses[5]. Three inequivalent layers that constitute the material can be observed. A LaO layer is coupled on both sides in the z-direction to two BiS$_2$ layers. The latter form inversion partners and are labelled A and B. Many such tri-layer systems are bound by Van Der Waals interaction to make up the whole material.

The interesting feature about this material is that the two BiS$_2$ layers, labelled A and B, are each other's inversion partners and on their own exhibit a polarization in the z-direction. The latter is due to the fact that both Bi and S atoms that constitute the layer have C_{4v} (polar) symmetry.

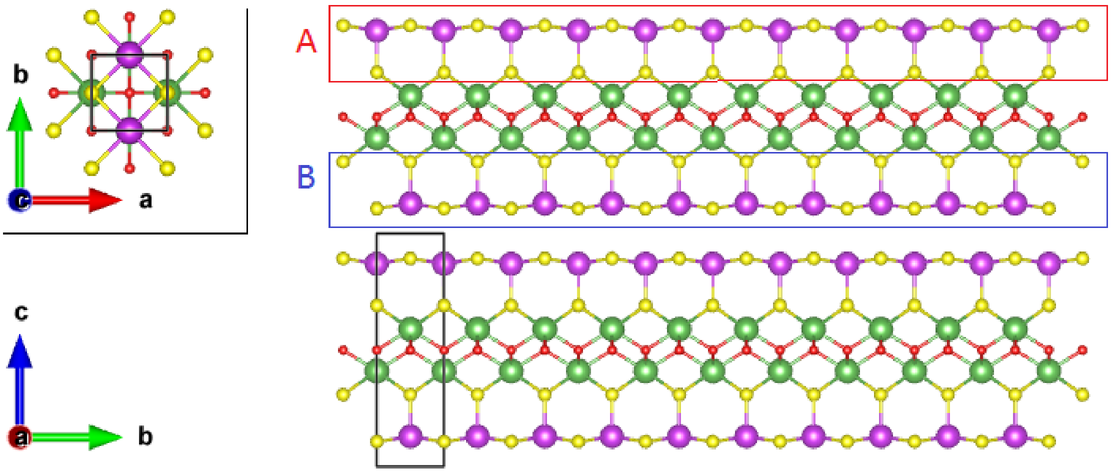

Figure 3.2: Two tri-layer systems that, when stacked in the z-direction, will form bulk $LaOBiS_2$ (P4/nmm). The conventional unit cell is visible at the left of the lower layer. In the upper tri-layer, both BiS_2 layers are labelled A and B, which are each other's inversion partners. A top view along the unique anisotropic direction is shown in the upper left corner.

In what follows it will be shown that, using the H_{SO} (3.6) interaction for C_{2v} symmetry, the individual BiS_2 layers exhibit a very clear R-1 and D-1 effect. When both layers (inversion partners) are brought together to form the crystal, the total spin polarization will vanish, leading to a zero net spin polarization and a degenerate energy spectrum. Nonetheless, the localized spin polarization on the different real space sectors might remain, which would be exactly the D-2 and R-2 effect.

The full model entails both the Dresselhaus term and the Rashba term in H_{SO}, i.e. $\neg(\gamma_D = \alpha_R = 0)$. However, keeping both terms results in eigenvalues that are very extended and do not give much insight, appendix II. Instead considering both terms separately is more feasible and gives clearer predictions on the spin texture of the material. In the next sections a full calculation for the Rashba term will be given ($\gamma_D = 0$) and the results of the Dresselhaus term are stated, knowing that the calculation is completely analogous.

3.4 One BiS_2 layer with polar structural asymmetry

Contrary to $LaOBiS_2$ as a whole, one BiS_2 layer does not have inversion symmetry, therefore it is expected that it has a net spin polarization that lifts the spin degeneracy of the system. Both atom sites have C_{4v} symmetry which allows for a strong electric polarization. This feature is already a strong indicator for R-1, and thus inevitably D-1 effects.

The Rashba behaviour is obtained by taking into account the spin-orbit interaction with

H_{SO} (3.6), where γ_D will be neglected. The total Hamiltonian for layer A becomes

$$\begin{aligned} H_A &= H_{kin} + H_{SO} \\ &= -\frac{\hbar^2}{2m}\nabla^2 + \alpha_R(k_y\sigma_x - k_x\sigma_y) \quad . \end{aligned} \tag{3.14}$$

It is important to keep in mind that α_R indicates the magnitude of the spin-orbit interaction and should be proportional to the intrinsic electric field, E_{in}, that induces the spin-orbit coupling. Later in the thesis it is shown that for the A layer, E_{in} points in the negative z-direction which leads to the relative minus sign compared to (3.6). Evidently, its inversion partner B will not have this minus sign due to E_{in} pointing in the positive z-direction.

This equation can be solved for the eigenenergy and -states of a single layer by diagonalizing the corresponding matrix:

$$H_A = \begin{pmatrix} \epsilon_k & \alpha_R(k_y + ik_x) \\ \alpha_R(k_y - ik_x) & \epsilon_k \end{pmatrix} = \begin{pmatrix} \epsilon_k & i\alpha_R k e^{-i\varphi} \\ -i\alpha_R k e^{i\varphi} & \epsilon_k \end{pmatrix} \tag{3.15}$$

Here, $k_x = k\cos(\varphi)$ and $k_y = k\sin(\varphi)$, with φ the angle of the crystal momentum $\vec{k}$ in the xy-plane and ϵ_k again the eigenenergy of the single particle in the lattice, without taking spin-orbit coupling into account, proportional to k^2. This results in eigen energies

$$E_\pm(k) = \epsilon_k \pm \alpha_R k \quad , \tag{3.16}$$

with corresponding eigenstates

$$\begin{aligned} \psi_+^{(A)} &= \frac{1}{\sqrt{2}}\begin{pmatrix} ie^{-i\varphi} \\ 1 \end{pmatrix} \\ \psi_-^{(A)} &= \frac{1}{\sqrt{2}}\begin{pmatrix} -ie^{-i\varphi} \\ 1 \end{pmatrix} \quad . \end{aligned} \tag{3.17}$$

It is clear that the spin-orbit interaction has lifted the spin degeneracy from the system's spectrum. This is also made visible in figure 3.3 by plotting $E_\pm(k)$ in the absence of spin-orbit interaction ($\alpha_R = 0$) and when spin-orbit interaction is present.

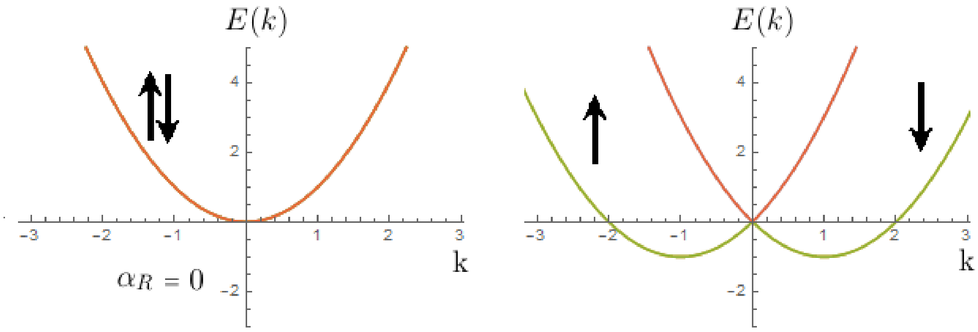

Figure 3.3: Band splitting due to the presence of spin-orbit effects in solid matter, with arbitrary units.

The spin structure of the BiS_2 layer is straightforward to calculate by evaluating the expectation values of the spin components $\langle \psi_\pm \mid \sigma_{x,y,z} \mid \psi_\pm \rangle$. This gives, after trivial calculations, the following result which represents the characteristic Rashba helical spin texutes:

$$\begin{aligned} \langle \sigma \rangle_{\psi_+} &= \begin{pmatrix} \sin(\varphi) \\ -\cos(\varphi) \\ 0 \end{pmatrix} \\ \langle \sigma \rangle_{\psi_-} &= \begin{pmatrix} -\sin(\varphi) \\ \cos(\varphi) \\ 0 \end{pmatrix} \end{aligned}$$

All of the above calculations can be done analogously for the case where the Rashba term is neglected and only Dresselhaus effects are taken into account. The results are similar, from

$$H_A = H_{kin} + H_{SO} = \begin{pmatrix} \epsilon_k & \gamma_D(k_y - ik_x) \\ \gamma_D(k_y + ik_x) & \epsilon_k \end{pmatrix}$$

the eigenenergies, eigenstates and spin expectation values can be obtained:

$$E_\pm(k) = \epsilon_k \pm \gamma_D k, \quad \psi_\pm^{\mathrm{A}} = \frac{1}{\sqrt{2}} \begin{pmatrix} \pm i e^{+i\varphi} \\ 1 \end{pmatrix}, \quad \langle \sigma \rangle_{\psi_\pm} = \pm \begin{pmatrix} \sin(\varphi) \\ \cos(\varphi) \\ 0 \end{pmatrix}$$

It is important for the next section to note that the above calculations were performed for the A-layer. If instead layer B is considered, due to the polar electric field pointing in the opposite direction, the signs of the eigenenergy and eigenstates also become opposite, e.g. $E_\pm^B = E_\mp^A$, likewise for the spin expectation values.

These results show that the model predicts both D-1 and R-1 effects, resulting in a net spin polarization on each of the single BiS_2 layers. The extent to which both spin textures are present needs to be determined by experiment or DFT calculations which will be done explicitly in chapter four of this thesis.

3.5 Two BiS_2 layers as inversion partners

To look for the hidden spin polarizations effects, more than one BiS_2 layer is needed to ensure global inversion symmetry. The bulk $LaOBiS_2$ crystal is built up by stacking atomic layers in the z-direction. There are two possible, inequivalent ways to pair up two BiS_2 layers (as can be seen on figure 3.2). The first one is where the BiS_2 inversion partners are separated by the LaO layer. However, this separating layer acts like a buffer, which makes the direct interaction between both BiS_2 layers negligible[6]. The second option on the other hand, is to consider the inversion partner that is directly bound with the Van Der Waals interaction. In principle both interaction directions need to be taken into account if it is not a priori known if one is negligible. This general treatment is done in next section for the topological insulator Bi_2Se_3.

Mathematically, the model for LaOBiS$_2$ as a whole translates into the use of the following Hamiltonian that preserves the layered character of the crystal.

$$H_{BL} = \begin{pmatrix} H_A & T \\ T & H_B \end{pmatrix}$$

Here, $H_{A,B}$ are the Hamiltonian matrices of BiS$_2$ layer A and B, respectively, treated in the previous section. Again, it is important to note that the sign of spin-orbit parameters α_R and γ_D are opposite in H_A and H_B due to opposite internal electric fields.

$T = t_k I_{2\times 2}$ is a two-by-two matrix that represents the coupling between the two BiS$_2$ layers through the Van Der Waals interaction with coupling strength t_k. Again, the full calculation will be given for the Rashba term ($\gamma_D = 0$) whereas for the Dresselhaus term only the results will be stated. The complete matrix and eigenvalues can be found in appendix II.

3.5.1 Hidden Rashba spin polarization: R-2

The total Hamiltonian matrix that needs to be solved for the eigenvalues and -states looks as follows:

$$H_{BL} = \begin{pmatrix} \epsilon_k & \alpha_R(k_y + ik_x) & t_k & 0 \\ \alpha_R(k_y - ik_x) & \epsilon_k & 0 & t_k \\ t_k & 0 & \epsilon_k & -\alpha_R(k_y + ik_x) \\ 0 & t_k & -\alpha_R(k_y - ik_x) & \epsilon_k \end{pmatrix} \tag{3.18}$$

Diagonalizing gives the spectrum of the system

$$E_\pm = \epsilon_k \pm \sqrt{\alpha_R^2 k^2 + t_k^2} \tag{3.19}$$

and the eigenstates

$$\Psi_1^- = \frac{1}{\sqrt{2}} \begin{pmatrix} -1 \\ -\frac{i\alpha_R k e^{i\varphi}}{\sqrt{\beta}} \\ \frac{t_k}{\sqrt{\beta}} \\ 0 \end{pmatrix}, \Psi_2^+ = \frac{1}{\sqrt{2}} \begin{pmatrix} 0 \\ \frac{t_k}{\sqrt{\beta}} \\ -\frac{i\alpha_R k e^{-i\varphi}}{\sqrt{\beta}} \\ 1 \end{pmatrix},$$

$$\Psi_3^- = \frac{1}{\sqrt{2}} \begin{pmatrix} 0 \\ \frac{t_k}{\sqrt{\beta}} \\ -\frac{i\alpha_R k e^{-i\varphi}}{\sqrt{\beta}} \\ -1 \end{pmatrix}, \Psi_4^+ = \frac{1}{\sqrt{2}} \begin{pmatrix} 1 \\ -\frac{i\alpha_R k e^{i\varphi}}{\sqrt{\beta}} \\ \frac{t_k}{\sqrt{\beta}} \\ 0 \end{pmatrix}, \tag{3.20}$$

with $\beta = \alpha_R^2 k^2 + t_k^2$. The superscript $\pm$ above each eigenstate denotes which eigenenergy the state belongs to. It is immediately clear that each energy level has become twofold degenerate, in contrast to the single BiS$_2$ layer. The spin-orbit interaction itself splits the energy levels, whereas the coupling of the two layers results in a doubly degenerate energy. It is important to note that because the states are two-by-two degenerate, any linear combination of them results in new, equivalent eigenstates. The states above however have been specifically constructed for reasons that will become clear later on.

The spectrum (3.19) is depicted in figure 3.4 for different values for the spin-orbit interaction parameter α_R and the coupling strength t_k.

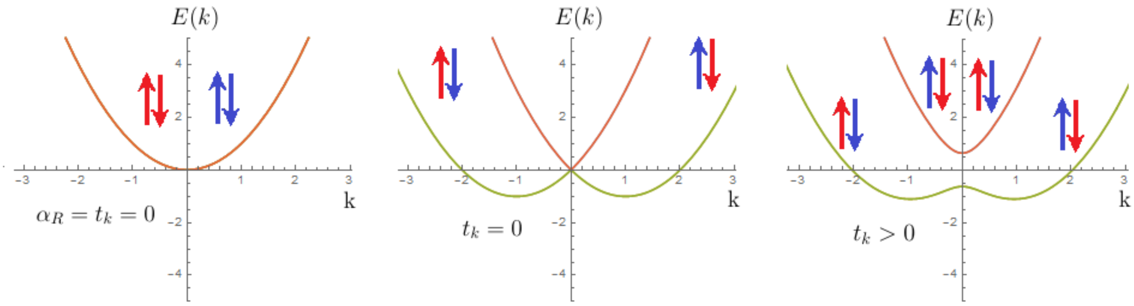

Figure 3.4: three cases of the spectrum of Bulk LaOBiS$_2$ around the $\vec{k} = 0$ (Γ) point.

It is clear that the spin-orbit interaction reduces the four-fold degeneracy of the two layer system to doubly degenerate bands, which are still spin degenerate. However, the model should predict, and indeed it will, that even though the bands are spin degenerate, those spins are spatially separated and localized on the different sectors. The coupling between the layers opens a gap. Because in LaOBiS$_2$ the inversion partners are coupled by Van Der Waals interaction, thus $t_k \approx 0$ the band structure is expected to look like the middle case in figure 3.4. This is indeed the case (see figure 4.1, section 4.1.1).

Due to the layer-preserving form of H_{BL} (3.18), it is expected that the first and last two components of each eigenstate in (3.20) correspond to the first and second BiS$_2$ layer, respectively. Thus the spin of each bi-layer eigenstate can be separated in the spin of the first two components (first layer) and second two components (second layer). The expectation values can again be calculated by evaluating $\langle \Psi^{\pm}_{i,\mathrm{I}} \mid \sigma_{x,y,z} \mid \Psi^{\pm}_{i,\mathrm{I}} \rangle$, for the first two components of the i^{th} eigenstate and $\langle \Psi^{\pm}_{i,\mathrm{II}} \mid \sigma_{x,y,z} \mid \Psi^{\pm}_{i,\mathrm{II}} \rangle$ for the second two components, together with their limit when t_k goes to zero:

$$\begin{array}{rcl}
\Psi^{-}_{1,\mathrm{I}}: & \left[-\frac{\alpha_R k}{\sqrt{\beta}}\sin(\varphi), \frac{\alpha_R k}{\sqrt{\beta}}\cos(\varphi), -\frac{1}{2}\frac{t_k^2}{\beta}\right] & \rightarrow [-\sin(\varphi), \cos(\varphi), 0] \\
\Psi^{-}_{1,\mathrm{II}}: & \left[0, 0, -\frac{1}{2}\frac{t_k^2}{\beta}\right] & \rightarrow [0,0,0] \\
 & & \\
\Psi^{+}_{2,\mathrm{I}}: & \left[0, 0, \frac{1}{2}\frac{t_k^2}{\beta}\right] & \rightarrow [0,0,0] \\
\Psi^{+}_{2,\mathrm{II}}: & \left[-\frac{\alpha_R k}{\sqrt{\beta}}\sin(\varphi), \frac{\alpha_R k}{\sqrt{\beta}}\cos(\varphi), \frac{1}{2}\frac{t_k^2}{\beta}\right] & \rightarrow [-\sin(\varphi), \cos(\varphi), 0] \\
 & & \\
\Psi^{-}_{3,\mathrm{I}}: & \left[0, 0, \frac{1}{2}\frac{t_k^2}{\beta}\right] & \rightarrow [0,0,0] \\
\Psi^{-}_{3,\mathrm{II}}: & \left[\frac{\alpha_R k}{\sqrt{\beta}}\sin(\varphi), -\frac{\alpha_R k}{\sqrt{\beta}}\cos(\varphi), \frac{1}{2}\frac{t_k^2}{\beta}\right] & \rightarrow [\sin(\varphi), -\cos(\varphi), 0] \\
 & & \\
\Psi^{+}_{4,\mathrm{I}}: & \left[\frac{\alpha_R k}{\sqrt{\beta}}\sin(\varphi), -\frac{\alpha_R k}{\sqrt{\beta}}\cos(\varphi), -\frac{1}{2}\frac{t_k^2}{\beta}\right] & \rightarrow [\sin(\varphi), -\cos(\varphi), 0] \\
\Psi^{+}_{4,\mathrm{II}}: & \left[0, 0, -\frac{1}{2}\frac{t_k^2}{\beta}\right] & \rightarrow [0,0,0]
\end{array}$$

This result is already a strong clue of the presence of the R-2 effect in the system. It shows that the degenerate states Ψ_2^+ and Ψ_4^+ (and also Ψ_1^- and Ψ_3^-) of the bi-layer system have opposite spin texture, and are mixed by the strength of coupling t_k between the layers. Moreover, the value of t_k determines the z-component of the spin, which vanishes as $t_k \to 0$, resulting in a pure Rashba spin texture, localized on each real space layer. The case where the coupling becomes small is realistic due to the Van Der Waals interaction.

To make this all more visible, the eigenstates of the bi-layer system (3.20) are given in the limiting case where t_k approaches zero.

$$\Psi_1^- \to \frac{1}{\sqrt{2}}\begin{pmatrix} -1 \\ -ie^{i\varphi} \\ 0 \\ 0 \end{pmatrix} = \begin{pmatrix} \psi_-^{(\mathrm{A})} \\ 0 \end{pmatrix} \quad , \Psi_2^+ \to \frac{1}{\sqrt{2}}\begin{pmatrix} 0 \\ 0 \\ -ie^{-i\varphi} \\ 1 \end{pmatrix} = \begin{pmatrix} 0 \\ \psi_+^{(\mathrm{B})} \end{pmatrix} \quad ,$$

$$\Psi_3^- \to \frac{1}{\sqrt{2}}\begin{pmatrix} 0 \\ 0 \\ -ie^{-i\varphi} \\ -1 \end{pmatrix} = \begin{pmatrix} 0 \\ \psi_-^{(\mathrm{B})} \end{pmatrix} \quad , \Psi_4^+ \to \frac{1}{\sqrt{2}}\begin{pmatrix} 1 \\ -ie^{i\varphi} \\ 0 \\ 0 \end{pmatrix} = \begin{pmatrix} \psi_+^{(\mathrm{A})} \\ 0 \end{pmatrix} \quad ,$$

where, $\psi_\pm^{A/B}$ are the Rashba one-layer eigenstates (3.17).

This gives a clear image that the first and last two components of the bi-layer eigenstates are indeed corresponding to BiS$_2$ layer A and B, respectively. Consequently, the spinvectors of the bi-layer system eigenstates reduce to the spinvectors of the individual BiS$_2$ layers, showing a localized, pure Rashba spin texture. As mentioned before this would not necessarily be the case for any set of eigenvectors of the system. The eigenstates used here are specifically constructed linear combinations such that they preserve the layered structure and reduce accordingly, just to make the interpretation easier.

In order to obtain the spin expectation values for a specific BiS$_2$-layer as a whole, the corresponding components of the degenerate states have to be added after weighing them by their corresponding density. For example, for the BiS$_2$ A-layer, $\Psi_{1,I}^-$ and $\Psi_{3,I}^-$ need to be weighed and added. This is where the strength of these specifically constructed eigenstates comes into play, because they make the weighing of the spin components of each state very convenient due to their structure. For example to consider the limit $t_k \to 0$ it suffices to look at each $\Psi_{i,I/II}^\pm$ separately because in this limit the weights of the eigenvectors are either one or zero.

The limit of very strong coupling $t_k \to \infty$ is also considered. For each layer, by summing the corresponding components, it is clear that the z-component always vanishes identically. The x- and y-components always have a factor $1/\sqrt{\beta} \equiv 1/t_k$, which vanishes as t_k becomes very large. This shows that for large coupling between the layers not only the spin polarization of the entire crystal vanishes but also each layer on its own does not exhibit any spin texture.

In conclusion: this model clearly shows that each energy level of the bi-layer system is spin degenerate. In the case of weak coupling, these degenerate spin states correspond to Rashba spin textures which are localized in real space on each BiS$_2$ layer that are each other's inversion partner. Moreover, the helical spin textures are opposite in sign, making them cancel each other when summed over the entire unit cell. In the case of strong coupling the spin textures on each of the layers also vanishes. These properties together form the R-2 effect.

3.5.2 Hidden Dresselhaus spin polarization: D-2

The same results can be obtained when only the Dresselhaus term is considered, i.e. $\alpha_R = 0$.

The Hamiltonian matrix (3.18) now becomes

$$H_{BL} = \begin{pmatrix} \epsilon_k & -\gamma_D(k_y - ik_x) & t_k & 0 \\ -\gamma_D(k_y + ik_x) & \epsilon_k & 0 & t_k \\ t_k & 0 & \epsilon_k & \gamma_D(k_y - ik_x) \\ 0 & t_k & \gamma_D(k_y + ik_x) & \epsilon_k \end{pmatrix},$$

which leads to eigenvalues

$$E_{pm} = \epsilon_k \pm \sqrt{\gamma_D^2 k^2 + t_k^2} = \epsilon_k \pm \sqrt{\beta} \tag{3.21}$$

and eigenstates, with their corresponding limit when $t_k \to 0$

$$\begin{aligned}
\Psi_1^- &= \frac{1}{\sqrt{2}} \begin{pmatrix} 1 \\ \frac{i\gamma_D k e^{-i\varphi}}{\sqrt{\beta}} \\ -\frac{t_k}{\sqrt{\beta}} \\ 0 \end{pmatrix} \to \frac{1}{\sqrt{2}} \begin{pmatrix} 1 \\ ie^{-i\varphi} \\ 0 \\ 0 \end{pmatrix} = \begin{pmatrix} \psi_-^{(\mathrm{A})} \\ 0 \end{pmatrix} \\
\Psi_2^+ &= \frac{1}{\sqrt{2}} \begin{pmatrix} 0 \\ -\frac{t_k}{\sqrt{\beta}} \\ \frac{i\gamma_D k e^{i\varphi}}{\sqrt{\beta}} \\ -1 \end{pmatrix} \to \frac{1}{\sqrt{2}} \begin{pmatrix} 0 \\ 0 \\ ie^{i\varphi} \\ -1 \end{pmatrix} = \begin{pmatrix} 0 \\ \psi_+^{(\mathrm{B})} \end{pmatrix} \\
\Psi_3^- &= \frac{1}{\sqrt{2}} \begin{pmatrix} 0 \\ -\frac{t_k}{\sqrt{\beta}} \\ \frac{i\gamma_D k e^{i\varphi}}{\sqrt{\beta}} \\ 1 \end{pmatrix} \to \frac{1}{\sqrt{2}} \begin{pmatrix} 0 \\ 0 \\ ie^{i\varphi} \\ 1 \end{pmatrix} = \begin{pmatrix} 0 \\ \psi_-^{(\mathrm{B})} \end{pmatrix} \\
\Psi_4^+ &= \frac{1}{\sqrt{2}} \begin{pmatrix} -1 \\ \frac{i\gamma_D k e^{-i\varphi}}{\sqrt{\beta}} \\ -\frac{t_k}{\sqrt{\beta}} \\ 0 \end{pmatrix} \to \frac{1}{\sqrt{2}} \begin{pmatrix} -1 \\ ie^{-i\varphi} \\ 0 \\ 0 \end{pmatrix} = \begin{pmatrix} \psi_+^{(\mathrm{A})} \\ 0 \end{pmatrix}
\end{aligned}$$

This time, $\psi_\pm^{A/B}$ are the Dresselhaus one-layer eigenstates (3.18).

The spin expectation values become

$$
\begin{array}{rcl}
\Psi^{-}_{1,\mathrm{I}}: & \left[\frac{\gamma_D k}{\sqrt{\beta}}\sin(\varphi), \frac{\gamma_D k}{\sqrt{\beta}}\cos(\varphi), \frac{1}{2}\frac{t_k^2}{\beta}\right] & \rightarrow [\sin(\varphi), \cos(\varphi), 0] \\
\Psi^{-}_{1,\mathrm{II}}: & \left[0, 0, \frac{1}{2}\frac{t_k^2}{\beta}\right] & \rightarrow [0, 0, 0] \\
& & \\
\Psi^{+}_{2,\mathrm{I}}: & \left[0, 0, -\frac{1}{2}\frac{t_k^2}{\beta}\right] & \rightarrow [0, 0, 0] \\
\Psi^{+}_{2,\mathrm{II}}: & \left[\frac{\gamma_D k}{\sqrt{\beta}}\sin(\varphi), \frac{\gamma_D k}{\sqrt{\beta}}\cos(\varphi), -\frac{1}{2}\frac{t_k^2}{\beta}\right] & \rightarrow [\sin(\varphi), \cos(\varphi), 0] \\
& & \\
\Psi^{-}_{3,\mathrm{I}}: & \left[0, 0, -\frac{1}{2}\frac{t_k^2}{\beta}\right] & \rightarrow [0, 0, 0] \\
\Psi^{-}_{3,\mathrm{II}}: & \left[-\frac{\gamma_D k}{\sqrt{\beta}}\sin(\varphi), -\frac{\gamma_D k}{\sqrt{\beta}}\cos(\varphi), -\frac{1}{2}\frac{t_k^2}{\beta}\right] & \rightarrow [-\sin(\varphi), -\cos(\varphi), 0] \\
& & \\
\Psi^{+}_{4,\mathrm{I}}: & \left[-\frac{\gamma_D k}{\sqrt{\beta}}\sin(\varphi), -\frac{\gamma_D k}{\sqrt{\beta}}\cos(\varphi), \frac{1}{2}\frac{t_k^2}{\beta}\right] & \rightarrow [-\sin(\varphi), -\cos(\varphi), 0] \\
\Psi^{+}_{4,\mathrm{II}}: & \left[0, 0, \frac{1}{2}\frac{t_k^2}{\beta}\right] & \rightarrow [0, 0, 0]
\end{array}
$$

The same discussion as the one for the Rashba states applies here. It is clear that the degenerate states have opposite, Dresselhaus spin texture but that these are localized on a different $\mathrm{BiS_2}$ layer. Both spin textures are mixed by the coupling between the layers with strength t_k. Because both layers are each other's inversion partner, summing over the whole crystal yields a zero spin polarization. However, local spin textures on the different sectors remain, leading to the predicted D-2 effect of hidden, compensating spin polarization.

As mentioned before, this observation by looking at each $\Psi^{\pm}_{i,\mathrm{I/II}}$ separately is possible due to the specifically constructed eigenstates that result in the zero values for the x- and y-components of some spin expected values. This also results in the feature that in the strong coupling limit, $t_k \rightarrow \infty$, the spin texture on each layer separately vanishes.

The constructed Hamiltonian thus predicts D-2 and R-2 behaviour in the layered $\mathrm{LaOBiS_2}$ material. However, as stated at the beginning of the discussion, in this case only one sided coupling was taken into account. Also, the coupling between the two inversion partners can be considered weak in $\mathrm{LaOBiS_2}$ since they are coupled by Van Der Waals interaction. In the next discussion, the model will be generalized by considering $\mathrm{Bi_2Se_3}$, in which the inversion partners will be bound by atomic layers.

3.6 Modelling two-sided coupled layer

3.6.1 Modelling the crystal

Bi_2Se_3 is a layered compound that has been studied extensively due to its experimentally verified topological surface states[21]. It has space group $R\bar{3}m$, making it a centrosymmetric bulk crystal. The material is built up of quintuple layers (QLs), bound by weak Van Der Waals interaction. Each QL itself is a layered structure consisting of two atomic Bi-layers and three atomic Se-layers which alternate each other. The layers that are each others inversion partners are two BiSe-layers, which are separated by a single Se-layer and all together form one quintuple layer (QL). Because the Bi- and Se-atoms in the inversion partners both have the polar C_{3v} atomic site symmetry, it is expected that each QL has hidden spin polarization only in the form of the R-2 effect, since the model predicted that C_{3v} symmetry does not allow for Dresselhaus spin textures (section 3.2).

In figure 3.5 the Bi_2Se_3 crystal structure is shown with its hexagonal unit cell. Two full QLs are visible, each consisting of five atomic layers. The inversion partners for one QL layer are indicated by A and B.

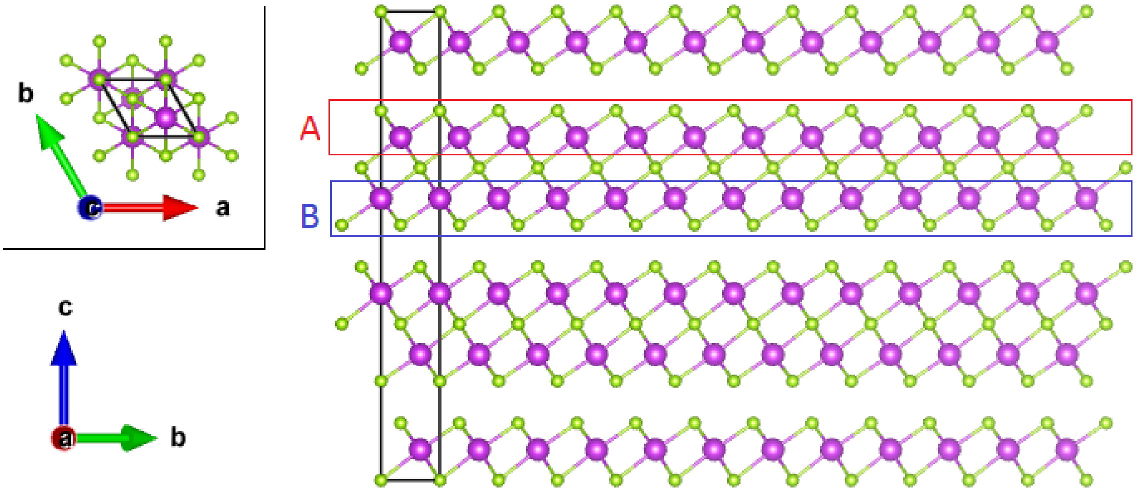

Figure 3.5: The layered structure of Bi_2Se_3 with a hexagonal unit cell, where the purple and yellow atoms correspond to respectively Bi and Se atoms. Two full QLs, of which each exists of five atomic layers, are separated by weak Van Der Waals interaction. The single atom layers within a QL are tightly bound together. The inversion partners, labelled A and B, are the two BiSe-layers which have C_{3v}-symmetry and are separated by a single Se-layer which has D_{3d}-symmetry. The unique anisotropic axis that ensures a polar atomic site symmetry is the c-axis along which the crystal shows its trigonal symmetry.

3.6.2 BiSe-layer system

The purpose is to construct a Hamiltonian that models the inversion partners A and B together with coupling on both sides of each BiSe-layer. The model should also be an extension to the Hamiltonian (3.18) used to describe both the atomic layers with polar atomic site symmetry and the LaOBiS2 bulk system. Considering the layered structure of the Bi2Se3 compound, the extension of (3.18) is straightforward:

$$H_{BL} = \begin{pmatrix} H_B & U & 0 & T \\ U & H_A & T & 0 \\ 0 & T & H_B & U \\ T & 0 & U & H_A \end{pmatrix} \quad .$$

Here, H_B and H_A are the 2×2 matrices that describe respectively layer B and A. The coupling matrices are $U = u_k I_{2\times2}$, which describes coupling between layer B and A through the Van Der Waals gap, and $T = t_k I_{2\times2}$ describes the coupling of layer A with B though the Selenium mono-layer.

This Hamiltonian clearly captures the two-sided coupling between inversion partners and is an extension of the previous model. The following procedure is analogous to the one followed for the LaOBiS$_2$ system, be it much more extensive. However, for Bi$_2$Se$_3$ only the Rashba term is possible and no calculations need to be done for the Dresselhaus case, since it is not allowed by the C_{3v} symmetry to exist.

3.6.3 Hidden spin polarization: R-2

If H$_{BL}$ is completely written out for the Rashba case, a rather extensive Hamiltonian matrix is obtained which is put in appendix II.

To obtain the eigenvalues and eigenstates this 8×8 Hamiltonian has to be diagonalized. A tedious calculation shows that the eigenvalues are given by

$$E_{\pm\pm} = \epsilon_k \pm \sqrt{\alpha_R^2 k^2 + (t_k \pm u_k)^2} = \epsilon_k \pm \sqrt{\beta_\pm} \quad ,$$

where $\beta_\pm$ is defined as $\alpha_R^2 k^2 + (t_k \pm u_k)^2$. Compared to the one-sided coupling case for the LaOBiS$_2$ system with coupling strength t_k, the two-sided coupling induces another degeneracy characterized by the coupling strength u_k. The band structure will now depend on these two coupling parameters u_k and t_k and depending on their relative strength, different situations can occur, figure 3.6.

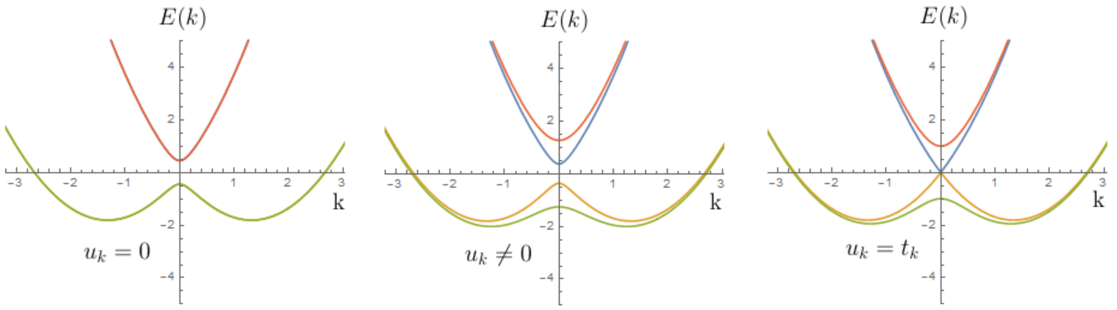

Figure 3.6: Energy dispersion in the case of coupling on both sides. The left panel represents coupling on one side,the middle panel coupling on both sides with no special relation between both coupling parameters and the right panel shows the dispersion when both coupling strengths are equal. Arbitrary units are used.

Once the eigenvalues are known, the eigenstates can be calculated and are shown below together with corresponding eigenenergy they belong to.

$$\begin{aligned}
\Psi_1 &= \frac{1}{2}\left(\frac{t_k-u_k}{\sqrt{\beta_-}} \;,0 \;,1 \;,\frac{i\alpha_R k e^{-i\varphi}}{\sqrt{\beta_-}} \;,-\frac{t_k-u_k}{\sqrt{\beta_-}} \;,0 \;,-1 \;,-\frac{i\alpha_R k e^{-i\varphi}}{\sqrt{\beta_-}}\right)^T \rightarrow E_{--} \\
\Psi_2 &= \frac{1}{2}\left(-1 \;,\frac{i\alpha_R k e^{-i\varphi}}{\sqrt{\beta_-}} \;,-\frac{t_k-u_k}{\sqrt{\beta_-}} \;,0 \;,1 \;,-\frac{i\alpha_R k e^{-i\varphi}}{\sqrt{\beta_-}} \;,\frac{t_k-u_k}{\sqrt{\beta_-}} \;,0\right)^T \rightarrow E_{--} \\
\Psi_3 &= \frac{1}{2}\left(-\frac{i\alpha_R k e^{i\varphi}}{\sqrt{\beta_-}} \;,1 \;,0 \;,-\frac{t_k-u_k}{\sqrt{\beta_-}} \;,\frac{i\alpha_R k e^{i\varphi}}{\sqrt{\beta_-}} \;,-1 \;,0 \;,\frac{t_k-u_k}{\sqrt{\beta_-}}\right)^T \rightarrow E_{+-} \\
\Psi_4 &= \frac{1}{2}\left(0 \;,\frac{t_k-u_k}{\sqrt{\beta_-}} \;,-\frac{i\alpha_R k e^{i\varphi}}{\sqrt{\beta_-}} \;,-1 \;,0 \;,-\frac{t_k-u_k}{\sqrt{\beta_-}} \;,\frac{i\alpha_R k e^{i\varphi}}{\sqrt{\beta_-}} \;,1\right)^T \rightarrow E_{+-} \\
\Psi_5 &= \frac{1}{2}\left(\frac{t_k-u_k}{\sqrt{\beta_+}} \;,0 \;,1 \;,\frac{i\alpha_R k e^{-i\varphi}}{\sqrt{\beta_+}} \;,-\frac{t_k-u_k}{\sqrt{\beta_+}} \;,0 \;,-1 \;,-\frac{i\alpha_R k e^{-i\varphi}}{\sqrt{\beta_+}}\right)^T \rightarrow E_{-+} \\
\Psi_6 &= \frac{1}{2}\left(-1 \;,\frac{i\alpha_R k e^{-i\varphi}}{\sqrt{\beta_+}} \;,-\frac{t_k-u_k}{\sqrt{\beta_+}} \;,0 \;,1 \;,-\frac{i\alpha_R k e^{-i\varphi}}{\sqrt{\beta_+}} \;,\frac{t_k-u_k}{\sqrt{\beta_+}} \;,0\right)^T \rightarrow E_{-+} \\
\Psi_7 &= \frac{1}{2}\left(-\frac{i\alpha_R k e^{i\varphi}}{\sqrt{\beta_+}} \;,1 \;,0 \;,-\frac{t_k-u_k}{\sqrt{\beta_+}} \;,\frac{i\alpha_R k e^{i\varphi}}{\sqrt{\beta_+}} \;,-1 \;,0 \;,\frac{t_k-u_k}{\sqrt{\beta_+}}\right)^T \rightarrow E_{++} \\
\Psi_8 &= \frac{1}{2}\left(0 \;,\frac{t_k-u_k}{\sqrt{\beta_-}} \;,-\frac{i\alpha_R k e^{i\varphi}}{\sqrt{\beta_+}} \;,-1 \;,0 \;,-\frac{t_k-u_k}{\sqrt{\beta_+}} \;,\frac{i\alpha_R k e^{i\varphi}}{\sqrt{\beta_+}} \;,1\right)^T \rightarrow E_{++} \quad (3.22)
\end{aligned}$$

At first glance these eigenstates do not give much insight. However, due to the layered structure of the Hamiltonian, eigenstates should exist where every two components of each eigenstate should correspond to one layer of the four-layer system (B-A-B-A). By reducing the four coupled layers to four uncoupled ones, it is expected to retrieve, per layer, the eigenstates of the one-layer system (3.17). As was the case for the LaOBiS$_2$ system, this procedure is also done to make sure that one of each pair of degenerate states has a spin expectation value $\langle\sigma_x\rangle = \langle\sigma_y\rangle = 0$ in the upper or lower layer. As discussed, this enables the possibility to study the spin evolution as a function of the coupling strengths by looking at only one of the two degenerate states.

To retrieve this specific set of eigenstates some extensive work has to be done. By using the following transformation on the eigenstates, which commutes with the Hamiltonian, thus preserving the eigenstates properties

$$\Lambda = \frac{\sqrt{2}}{2}\begin{pmatrix} I_{2\times2} & 0 & I_{2\times2} & 0 \\ 0 & -I_{2\times2} & 0 & I_{2\times2} \\ I_{2\times2} & 0 & -I_{2\times2} & 0 \\ 0 & I_{2\times2} & 0 & I_{2\times2} \end{pmatrix} \quad ,$$

and letting $u_k \rightarrow 0$ the desired set of eigenstates is obtained. If then $t_k \rightarrow 0$, the following states are obtained.

$$\Psi_1 = \begin{pmatrix} 0 \\ \psi_-^{(2)} \\ 0 \\ 0 \end{pmatrix}, \Psi_2 = \begin{pmatrix} 0 \\ 0 \\ \psi_-^{(3)} \\ 0 \end{pmatrix}, \Psi_3 = \begin{pmatrix} 0 \\ 0 \\ \psi_+^{(3)} \\ 0 \end{pmatrix}, \Psi_4 = \begin{pmatrix} 0 \\ \psi_+^{(2)} \\ 0 \\ 0 \end{pmatrix}$$

$$\Psi_5 = \begin{pmatrix} 0 \\ 0 \\ 0 \\ \psi_-^{(4)} \end{pmatrix}, \Psi_6 = \begin{pmatrix} \psi_-^{(1)} \\ 0 \\ 0 \\ 0 \end{pmatrix}, \Psi_7 = \begin{pmatrix} \psi_+^{(1)} \\ 0 \\ 0 \\ 0 \end{pmatrix}, \Psi_8 = \begin{pmatrix} 0 \\ 0 \\ 0 \\ \psi_+^{(4)} \end{pmatrix}$$

These are still 8-component eigenstates, only with **0** and $\psi_\pm^i$ two-component vectors. The $\psi_\pm^i$ are exactly the earlier obtained eigenstates for a single atomic layer (3.17). Here the superscript denotes the layer within the system, with (1,3) representing B-layers and (2,4) representing A-layers. The subscript denotes the corresponding eigenenergy, which is also in correspondence with the one-layer eigenenergies (taking into account the sign difference between A and B-layers).

Having established that the components of the eigenstates correspond two-by-two to the different layers of the B-A-B-A system, the spin can be evaluated per layer. This can be done by calculating the spin expectation values of each two components, $\langle\Psi_i|\sigma_{x,y,z}|\Psi_i\rangle$, leading to the following spinvectors together with their decoupling limit $t_k = u_k \to 0$:

$$\begin{aligned}
\Psi_1: \quad & \left(0 \quad ,0 \quad ,-\tfrac{1}{4}\tfrac{(t_k-u_k)^2}{\beta_-}\right) && \to (0,0,0) \\
& \left(\tfrac{\alpha_R k}{\sqrt{\beta_-}}\sin(\varphi) \quad ,-\tfrac{\alpha_R k}{\sqrt{\beta_-}}\cos(\varphi) \quad ,-\tfrac{1}{4}\tfrac{(t_k-u_k)^2}{\beta_-}\right) && \to (\sin(\varphi),-\cos(\varphi),0) \\
& \left(0 \quad ,0 \quad ,-\tfrac{1}{4}\tfrac{(t_k-u_k)^2}{\beta_-}\right) && \to (0,0,0) \\
& \left(\tfrac{\alpha_R k}{\sqrt{\beta_-}}\sin(\varphi) \quad ,-\tfrac{\alpha_R k}{\sqrt{\beta_-}}\cos(\varphi) \quad ,-\tfrac{1}{4}\tfrac{(t_k-u_k)^2}{\beta_-}\right) && \to (\sin(\varphi),-\cos(\varphi),0) \\
\Psi_2: \quad & \left(-\tfrac{\alpha_R k}{\sqrt{\beta_-}}\sin(\varphi) \quad ,\tfrac{\alpha_R k}{\sqrt{\beta_-}}\cos(\varphi) \quad ,\tfrac{1}{4}\tfrac{(t_k-u_k)^2}{\beta_-}\right) && \to (-\sin(\varphi),\cos(\varphi),0) \\
& \left(0 \quad ,0 \quad ,\tfrac{1}{4}\tfrac{(t_k-u_k)^2}{\beta_-}\right) && \to (0,0,0) \\
& \left(-\tfrac{\alpha_R k}{\sqrt{\beta_-}}\sin(\varphi) \quad ,\tfrac{\alpha_R k}{\sqrt{\beta_-}}\cos(\varphi) \quad ,\tfrac{1}{4}\tfrac{(t_k-u_k)^2}{\beta_-}\right) && \to (-\sin(\varphi),\cos(\varphi),0) \\
& \left(0 \quad ,0 \quad ,\tfrac{1}{4}\tfrac{(t_k-u_k)^2}{\beta_-}\right) && \to (0,0,0) \\
\Psi_3: \quad & \left(0 \quad ,0 \quad ,-\tfrac{1}{4}\tfrac{(t_k-u_k)^2}{\beta_-}\right) && \to (0,0,0) \\
& \left(\tfrac{\alpha_R k}{\sqrt{\beta_-}}\sin(\varphi) \quad ,-\tfrac{\alpha_R k}{\sqrt{\beta_-}}\cos(\varphi) \quad ,-\tfrac{1}{4}\tfrac{(t_k-u_k)^2}{\beta_-}\right) && \to (\sin(\varphi),-\cos(\varphi),0) \\
& \left(0 \quad ,0 \quad ,-\tfrac{1}{4}\tfrac{(t_k-u_k)^2}{\beta_-}\right) && \to (0,0,0) \\
& \left(\tfrac{\alpha_R k}{\sqrt{\beta_-}}\sin(\varphi) \quad ,-\tfrac{\alpha_R k}{\sqrt{\beta_-}}\cos(\varphi) \quad ,-\tfrac{1}{4}\tfrac{(t_k-u_k)^2}{\beta_-}\right) && \to (\sin(\varphi),-\cos(\varphi),0)
\end{aligned}$$

$$
\begin{array}{lll}
\Psi_4: & \left(0 \quad ,0 \quad ,\frac{1}{4}\frac{(t_k-u_k)^2}{\beta_-}\right) & \rightarrow (0,0,0) \\
& \left(-\frac{\alpha_R k}{\sqrt{\beta_-}}\sin(\varphi) \quad ,\frac{\alpha_R k}{\sqrt{\beta_-}}\cos(\varphi) \quad ,\frac{1}{4}\frac{(t_k-u_k)^2}{\beta_-}\right) & \rightarrow (-\sin(\varphi),\cos(\varphi),0) \\
& \left(0 \quad ,0 \quad ,\frac{1}{4}\frac{(t_k-u_k)^2}{\beta_-}\right) & \rightarrow (0,0,0) \\
& \left(-\frac{\alpha_R k}{\sqrt{\beta_-}}\sin(\varphi) \quad ,\frac{\alpha_R k}{\sqrt{\beta_-}}\cos(\varphi) \quad ,\frac{1}{4}\frac{(t_k-u_k)^2}{\beta_-}\right) & \rightarrow (-\sin(\varphi),\cos(\varphi),0) \\
\Psi_5: & \left(0 \quad ,0 \quad ,\frac{1}{4}\frac{(t_k+u_k)^2}{\beta_+}\right) & \rightarrow (0,0,0) \\
& \left(\frac{\alpha_R k}{\sqrt{\beta_+}}\sin(\varphi) \quad ,-\frac{\alpha_R k}{\sqrt{\beta_+}}\cos(\varphi) \quad ,\frac{1}{4}\frac{(t_k+u_k)^2}{\beta_+}\right) & \rightarrow (\sin(\varphi),-\cos(\varphi),0) \\
& \left(0 \quad ,0 \quad ,\frac{1}{4}\frac{(t_k+u_k)^2}{\beta_+}\right) & \rightarrow (0,0,0) \\
& \left(\frac{\alpha_R k}{\sqrt{\beta_+}}\sin(\varphi) \quad ,-\frac{\alpha_R k}{\sqrt{\beta_+}}\cos(\varphi) \quad ,\frac{1}{4}\frac{(t_k+u_k)^2}{\beta_+}\right) & \rightarrow (\sin(\varphi),-\cos(\varphi),0) \\
\Psi_6: & \left(-\frac{\alpha_R k}{\sqrt{\beta_+}}\sin(\varphi) \quad ,\frac{\alpha_R k}{\sqrt{\beta_+}}\cos(\varphi) \quad ,\frac{1}{4}\frac{(t_k+u_k)^2}{\beta_+}\right) & \rightarrow (\sin(\varphi),-\cos(\varphi),0) \\
& \left(0 \quad ,0 \quad ,\frac{1}{4}\frac{(t_k+u_k)^2}{\beta_+}\right) & \rightarrow (0,0,0) \\
& \left(-\frac{\alpha_R k}{\sqrt{\beta_+}}\sin(\varphi) \quad ,\frac{\alpha_R k}{\sqrt{\beta_+}}\cos(\varphi) \quad ,\frac{1}{4}\frac{(t_k+u_k)^2}{\beta_+}\right) & \rightarrow (-\sin(\varphi),\cos(\varphi),0) \\
& \left(0 \quad ,0 \quad ,\frac{1}{4}\frac{(t_k+u_k)^2}{\beta_+}\right) & \rightarrow (0,0,0) \\
\Psi_7: & \left(\frac{\alpha_R k}{\sqrt{\beta_+}}\sin(\varphi) \quad ,-\frac{\alpha_R k}{\sqrt{\beta_+}}\cos(\varphi) \quad ,-\frac{1}{4}\frac{(t_k+u_k)^2}{\beta_+}\right) & \rightarrow (\sin(\varphi),-\cos(\varphi),0) \\
& \left(0 \quad ,0 \quad ,-\frac{1}{4}\frac{(t_k+u_k)^2}{\beta_+}\right) & \rightarrow (0,0,0) \\
& \left(\frac{\alpha_R k}{\sqrt{\beta_+}}\sin(\varphi) \quad ,-\frac{\alpha_R k}{\sqrt{\beta_+}}\cos(\varphi) \quad ,-\frac{1}{4}\frac{(t_k+u_k)^2}{\beta_+}\right) & \rightarrow (\sin(\varphi),-\cos(\varphi),0) \\
& \left(0 \quad ,0 \quad ,-\frac{1}{4}\frac{(t_k+u_k)^2}{\beta_+}\right) & \rightarrow (0,0,0) \\
\Psi_8: & \left(0 \quad ,0 \quad ,-\frac{1}{4}\frac{(t_k+u_k)^2}{\beta_+}\right) & \rightarrow (0,0,0) \\
& \left(-\frac{\alpha_R k}{\sqrt{\beta_+}}\sin(\varphi) \quad ,\frac{\alpha_R k}{\sqrt{\beta_+}}\cos(\varphi) \quad ,-\frac{1}{4}\frac{(t_k+u_k)^2}{\beta_+}\right) & \rightarrow (-\sin(\varphi),\cos(\varphi),0) \\
& \left(0 \quad ,0 \quad ,-\frac{1}{4}\frac{(t_k+u_k)^2}{\beta_+}\right) & \rightarrow (0,0,0) \\
& \left(-\frac{\alpha_R k}{\sqrt{\beta_+}}\sin(\varphi) \quad ,\frac{\alpha_R k}{\sqrt{\beta_+}}\cos(\varphi) \quad ,-\frac{1}{4}\frac{(t_k+u_k)^2}{\beta_+}\right) & \rightarrow (-\sin(\varphi),\cos(\varphi),0)
\end{array}
\tag{3.23}
$$

These spin expectation values are very similar to the ones obtained for the one sided coupling system of $\mathrm{LaOBiS_2}$. The degenerate eigenstates, $\Psi_{1,2}, \Psi_{3,4}, \Psi_{5,6}$ and $\Psi_{7,8}$, show opposite spin texture, but localized on different layers of the inversion pair. Now, both t_k and u_k couple the spin textures, inducing a z-component to the spin. When the spin expectation values are reduced to the case of four uncoupled layers, pure localized Rashba spin textures emerge, with opposite sign, depending on the layer. Thus, when summed over the entire crystal the spin textures will cancel each other and no net spin polarization will be observed.

Again, when the spin expectation value of an entire layer is considered, it is clear that in the strong coupling limit, $t_k \to \infty$ or $u_k \to \infty$, the spin textures vanish on each layer separately.

3.7 Synthesis of the model and its predictions

So far a model has been constructed based on very broad symmetries to describe materials containing C_{2v} or C_{3v} atomic site symmetry groups. The model Hamiltonian was then applied to example materials for both symmetry groups to predict specific spin textures.

For $\mathrm{LaOBiS_2}$ the C_{2v}-model is applicable and predicts spin polarization, localized on two $\mathrm{BiS_2}$-layers which form inversion partners. This localized spin polarization manifests itself in both Rashba (R-2) and Dresselhaus (D-2) spin textures.

For the topological insulator $\mathrm{Bi_2Se_3}$ the C_{3v}-model is applicable and predicts that only Rashba localized spin textures will be present on the two BiSe-layers (R-2), whereas Dresselhaus spin textures are not allowed by the symmetry of inversion layers.

In the next two chapters of this thesis these predictions will be tested by means of Density Functional Theory (DFT) in bulk materials. Concretely the Rashba and/or Dresselhaus spin textures will be looked for, as well as their spatial localization on the inversion partners inside the material.

Chapter 4

First-principle studies for $LaOBiS_2$

All of the first-principles calculations were done using Density Function Theory (DFT) within the Vienna Ab Initio Simulation Package (VASP)[22]. Crystal structures are built and visualized by means of the free software VESTA. The data output is handled by MATLAB. In all the figures the units will be the same: energies will be in eV and reciprocal $\vec{k}$-space will be in units of Å^{-1}.

The details of the specific DFT calculations and the parameters used, as well as a short explanation on what that different parameters stand for, are given in appendix III.

4.1 The bulk $LaOBiS_2$ system

The first step is to find the exact lattice parameters and atomic positions of the crystal. For $LaOBiS_2$, the initial values for these parameters are the experimental values used from [23]. Then a relaxation is performed on lattice parameters and atomic position by iteratively adjusting the parameters and for each set of parameters minimizing the total energy.

The latter is done by a calculation that starts from the ensemble of atomic charge distributions and then iteratively converges to lower the total energy in the unit cell while lattice parameters and atomic positions are kept constant during this loop. Once convergence is reached the resulted charge distribution is the lowest energetic one for these specific lattice parameters and atomic positions. The final values are given in tabel (4.1).

Lattice parameters in $\mathring{A}$			
a=b	4.03		
c	13.99		
Atomic position in relative coordinates			
La_1	(0.5,0,0.411246)	Bi_2	(0.5,0,0.869595)
La_2	(0,0.5,0.588754)	S_1	(0.5,0,0.106295)
O_1	(0.5,0.5,0.5)	S_2	(0,0.5,0.893704)
O_2	(0,0,0.5)	S_3	(0,0.5,0.308752)
Bi_1	(0,0.5,0.13405)	S_4	(0.5,0,0.691248)

Table 4.1: Table with converged values of the $LaOBiS_2$ crystal. Values truncated.

These values are used for all further calculations concerning the $LaOBiS_2$ crystal. The unit cell that is used is the tetragonal unit cell which is depicted in figure 3.2.

Once the relaxed lattice parameters and atomic position are known, the band structure and spin expectation values can be obtained.

4.1.1 Band structure

Once the charge distribution has converged it can be used to calculate the band structure along a specific path in the crystal's brillouin zone, which is depicted in figure 4.2, right panel. First, the band structure along the Γ-X-M-Γ-Z-R-A-Z path will be calculated and plotted for two different cases in order to see the difference induced by spin-orbit coupling effects. The first band is plotted without spin-orbit coupling and the second with spin-orbit coupling explicitly taken into account for the calculations.

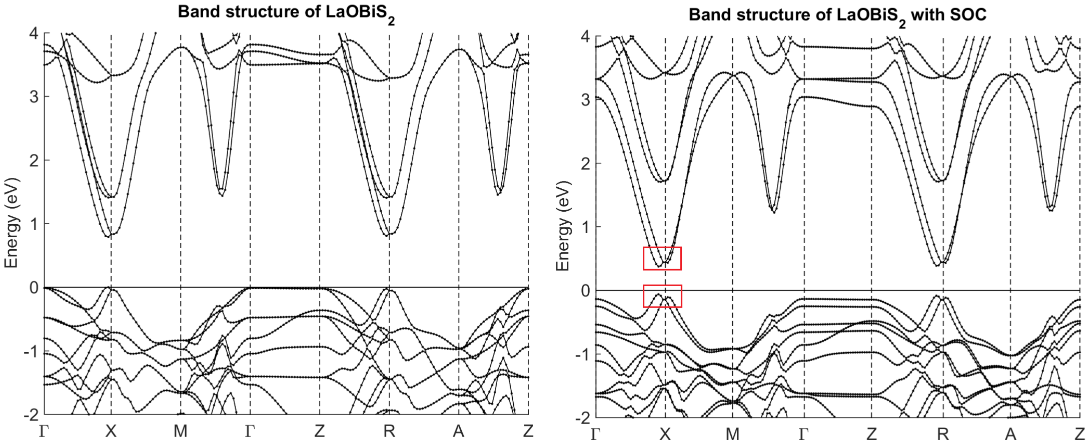

Figure 4.1: Band structure of $LaOBiS_2$ without (left panel) and with (right panel) spin-orbit coupling. The band splitting is most clear around the X, M, R and A points. In order to study this splitting more thoroughly, the bands around the X-point will be analysed (framed area on the left panel). The zero of energy is chosen to be the fermi energy level at the top of the valence band.

It is clear that when spin-orbit coupling is turned on, certain bands undergo splitting. Even though some degeneracy of the bands is lifted by the spin-orbit interaction, each band is still twofold degenerate and still represents two spin polarized states. The band splitting follows from the lifted spin degeneracy of each BiS_2 sector separately. However, since they are brought together as inversions partners, each band represents two sectors and the sign of the spin splitting will differ for each sector due to the electric field pointing in opposite direction. This results in each band containing two states with opposite spin.

This reasoning lies at the basis of the hidden spin polarization effects and is earlier schematically given by figure 2.4. It is exactly this that will be verified in the next section by investigating the spin textures of split bands around the X-point, in the framed area on figure 4.1.

4.1.2 Conduction Band

The first band that will be investigated is the conduction band of the calculation including the spin-orbit interaction, around the X-point; figure 4.1, right panel, top framed area. This band consists of the two split bands that cross at the X-point. Because the spin texture is expected to be three-dimensional (x-, y- and z-component), plotting a two-dimensional band surface centred around the X-point is convenient in order to visualize the spin vector field on an energy surface.

This 2-D energy surface is obtained by considering various paths in the Brillouin zone that cross in the X-point and calculating the band structure for each of these paths. The paths used for bulk LaOBiS$_2$ are the paths shown in figure 4.2, left panel, in the $k_z = 0$-plane. Since figure 4.1 shows almost no dispersion along the Γ-Z path in the three-dimensional Brillouin zone, any parallel plane to the Γ-X-M-plane could be used.

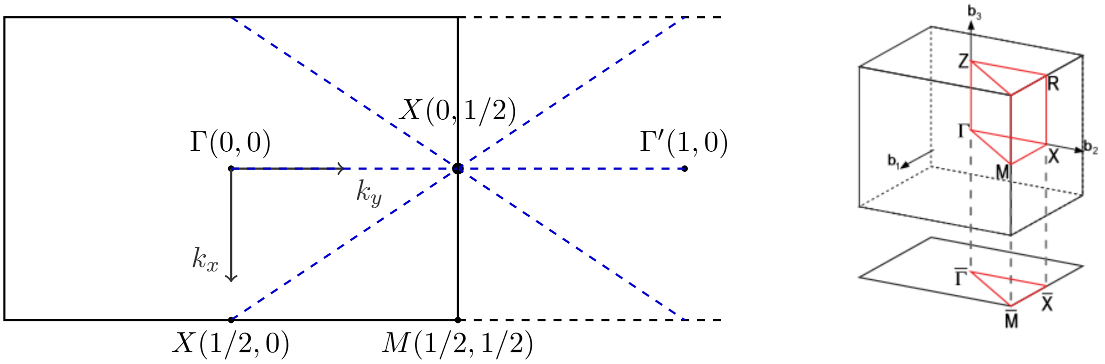

Figure 4.2: The left panel is a schematic representation of the paths used to calculate a band-surface in the $k_z = 0$-plane. The right panel represents the full Brillouin zone of the LaOBiS$_2$ unit cell and the direction in which the unit cell is projected, from Zhang et al.**source**

The conduction band along each path in $\vec{k}$-space can then be plotted in a three-dimensional plot with (k_x, k_y) for the $(x$-$y)$-plane and with the calculated energy $E(k_x, k_y)$ on the z-axis. The sampled points along the different paths are then linearly interpolated to result in a conduction band-surface. For the paths used as shown in figure 4.2, figure 4.3 shows the result for the conduction band-surface of bulk LaOBiS$_2$.

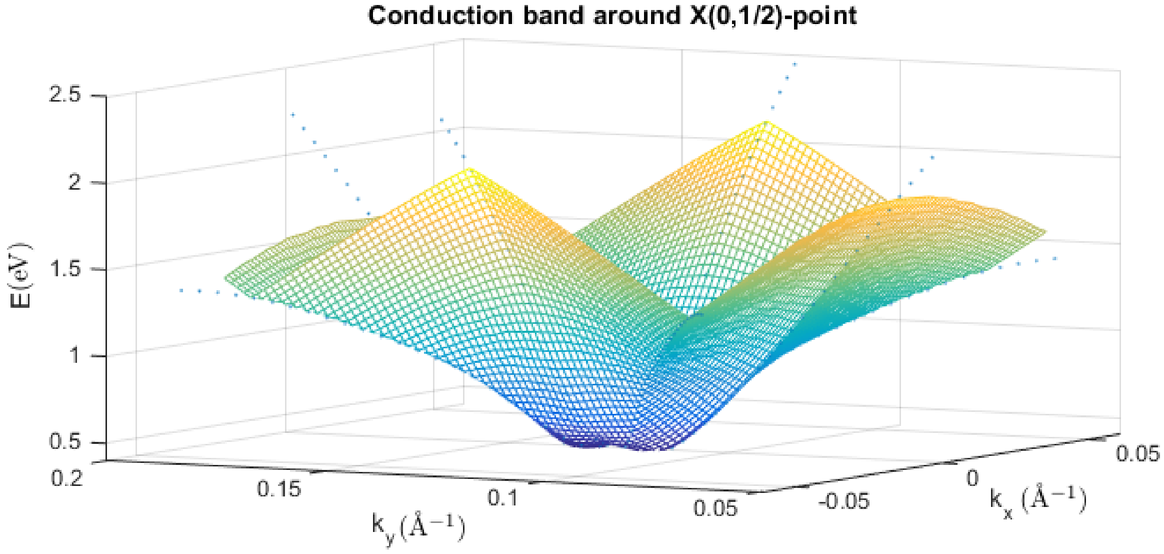

Figure 4.3: Three-dimensional conduction band-surface of bulk LaOBiS$_2$, centred around the X-point, obtained by linear interpolation between the calculated Brillouin zone paths.

To visualize the spin vector field on this surface, the spin data first has to be extracted from the VASP output files through a Matlab script. For each point (k_x, k_y) along the paths in the projected Brillouin zone, the components of the spin expectation value of that state can be represented by a vector. Because every $\vec{k}$-point on the degenerate band-surface represents two states, two spin vectors will be present, one for each degenerate state.

The result is shown in figure 4.4. It represents the conduction band-surface on which two spin vector fields are plotted, one field for each degenerate state, with its own color (red, blue).

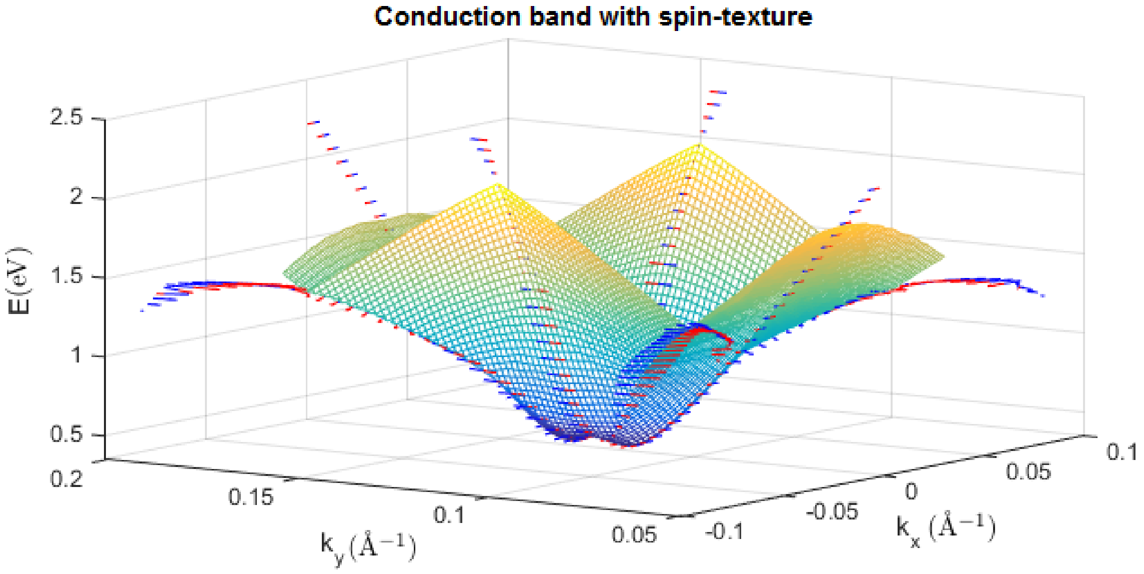

Figure 4.4: Three-dimensional band structure of the LaOBiS$_2$ bulk conduction band with the spin expectation values for each state, represented as a vector field.

This kind of three-dimensional representation is very insightful if it can be rotated in a Matlab environment, however it is not that useful as a static figure. To have a clear overview of the spin texture, the three-dimensional representation of figure 4.4 is projected along the z-axis. The band-surface becomes a contour-plot and the spin vector field becomes two-dimensional, losing its information about the z-component. However, the three-dimensional representation in figure 4.4 shows that close to the X-point, the spin vector field has no z-component at all, so no information will be lost in the process.

This new and more insightful representation is depicted in figure 4.5

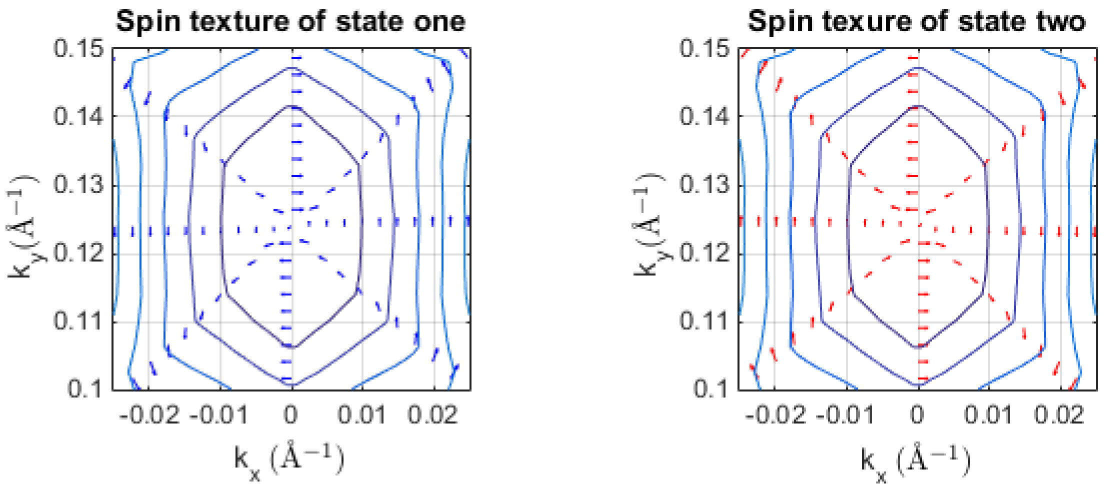

Figure 4.5: Projected representation of the conduction band surface with the spin vector fields plotted on top of it.

These plots show that the calculation indeed results in spin polarization for both degenerate states separately, with each spin state having opposite sign. Moreover, the spin texture is in agreement with figure 3.1, right panel, which represents the Dresselhaus spin-orbit effect. However, caution is called for because the resulted spin texture could be a coincidence in the following way.

As noted in the model, any linear combination of the two degenerate states is also an eigenstate of the system. Which linear combination is obtained by the DFT calculation is not a priori known. Thus the resulted spin texture in figure 4.5 could very well be obtained by using a specific linear combination that results in eigenstates which are not representative for both inversion partners.

This is crucial since the model predicts a hidden spin polarization in the form of compensating, localized spin textures. So, what still needs to be checked is whether the observed spin textures are indeed from eigenstates that are localized on the different inversion sectors (opposing BiS_2-layers) and cancel each other out when summed over the entire unit cell.

4.1.3 Localized spin textures

VASP allows for calculations that project the total wavefuction on the atomic sites constituting the unit cell. This is done by looking at what portion of the charge density is located in a radius around a specific ion. This site projection of the total wavefunction can be used to check whether the eigenstates resulting in the obtained spin textures in figure 4.5 are indeed localized on the inversion partner BiS_2-layers.

The following figure shows the contribution of the degenerate states to each atomic layer.

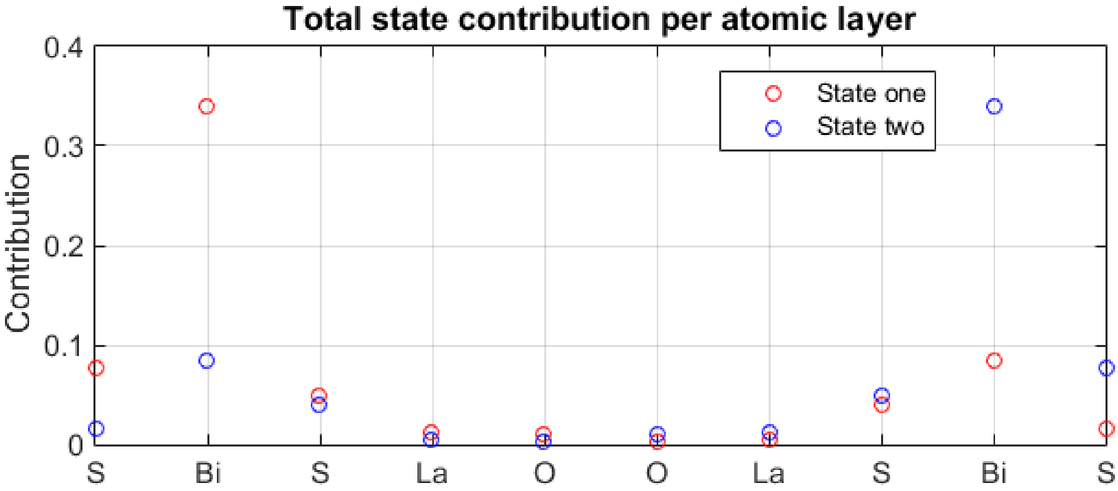

Figure 4.6: Contribution per atomic layer to the first degenerate state of the conduction band. Localization of state two on the bottom BiS_2-layer, more specifically on the Bi atom.

It is clear that both states, which have their own Dresselhaus spin textures, are mainly attributed to the corresponding BiS_2 layers, which are each others inversion partners. This shows that the eigenstates used by VASP are indeed localized and thus both spin textures are as well localized on the BiS_2 sectors, as is predicted by the model. Also note the symmetry between both distributions of the states as it will be of importance later on when surfaces are taken into account.

A supplementary way to verify the localized nature of the spin textures makes use of the possibility to calculate and plot the spin textures for each layer separately. In this way it can be directly verified which layers exhibit Dresselhaus spin texture are which ones do not exhibit spin textures at all.

Three different figures will be represented in the same manner as figure 4.5, which is a contour plot of the energy with the spin vector field projected on it. The first, second and third figure, 4.7, 4.8 and 4.9, are the spin textures of both degenerate states, belonging to the top BiS_2-, LaO- and bottom BiS_2-layers, respectively, weighted by their density on each atom. Of these layers, the top and bottom BiS_2-layers are considered to be inversion partners.

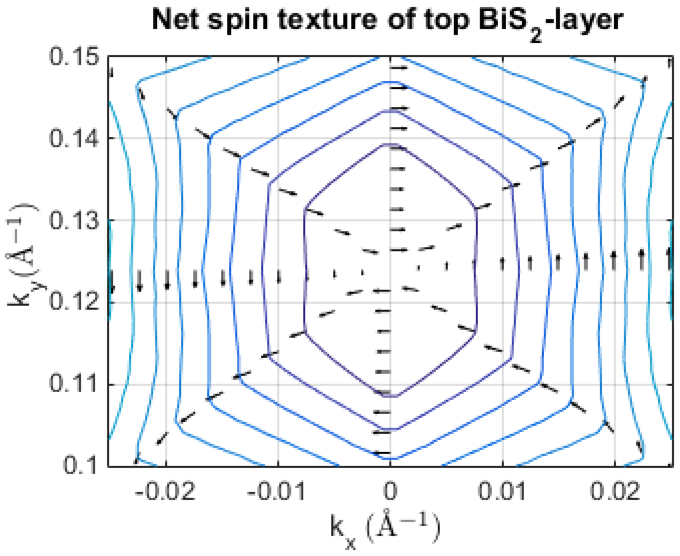

Figure 4.7: Total summed spin texture of both degenerate conduction band states attributed to the top BiS$_2$-layer of the unit cell. Clear Dresselhaus spin texture can be seen that is in correspondence to the first state, figure 4.5, left panel.

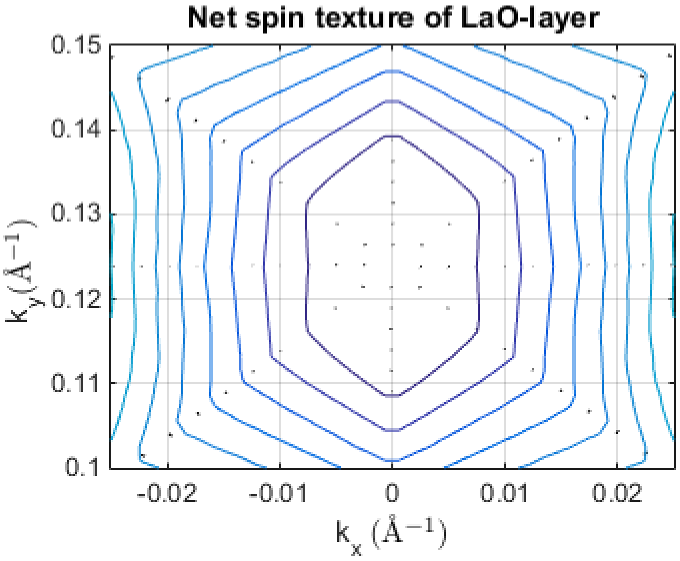

Figure 4.8: Total summed spin texture of both degenerate conduction band states attributed to the LaO-layer of the unit cell. Neither of both states show any significant spin texture.

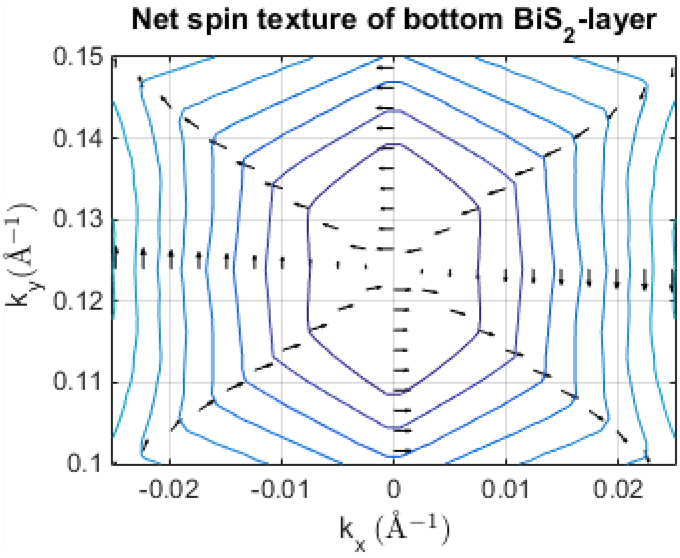

Figure 4.9: Total summed pin texture of both degenerate conduction band states attributed to the bottom BiS$_2$-layer of the unit cell. Clear Dresselhaus spin texture can be seen that is in correspondence to the second state, figure 4.5, right panel.

These results confirm the previously shown spatial separation between both spin textures. This is again in agreement with the model constructed in this thesis to predict hidden spin polarization.

The last aspect of the D-2 effect that needs to be checked is whether the net spin polarization vanishes when summed over the spins of both states in the entire unit cell. With the tools used to visualize previous results this can be easily done and results in the figure 4.10.

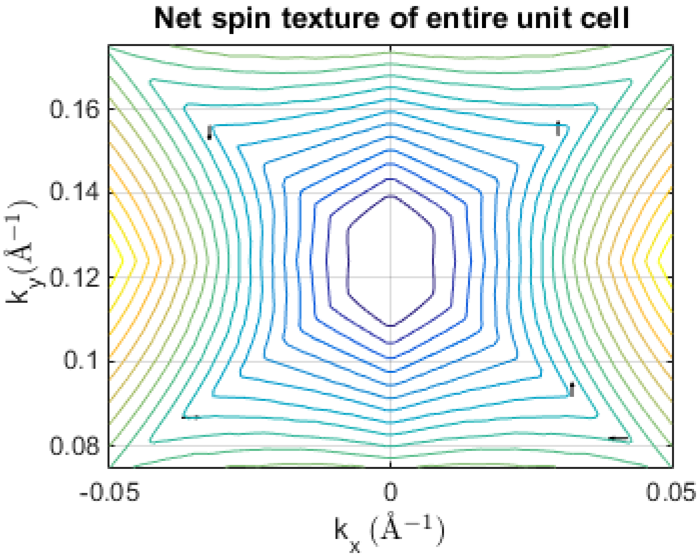

Figure 4.10: Net spin polarization when summed over the spins of both degenerate states belonging to the conduction band. It is clear that both spin textures cancel each other perfectly.

It is immediately clear that there is no total spin texture present. Thus, Dresselhaus spin textures cancel each other out when combined, leading to a zero spin polarization attributed to the conduction band eigenstates. Together with the fact that both spin textures are localized on spatially separated sectors, it can be concluded that for the conduction band a very distinct D-2 effect is observed. This is in agreement with the prediction of the model for C_{2v} atomic sites such as the BiS_2 inversion partners.

However, the model also allows for the R-2 effect which is not present in the conduction band eigenstates. As an illustration of the R-2 effect and the fact that spin textures can depend strongly on the specific type of band, the valence band of the bulk $LaOBiS_2$ system is studied. The same calculations can be done and similar analysis will lead to a clear hidden spin polarization, this time in the form of the R-2 effect.

4.1.4 Valence Band

Now, the valence band will be investigated for hidden spin polarization. Concerning the DFT calculations themselves, nothing changes, the chosen paths in the Brillouin zone are the same as for the conduction band, see figure 4.2. The only difference is the bands chosen from figure 4.1, right panel. The valence band crosses at the X-point and is a combination of two spin-orbit split bands.

The same steps are followed to obtain visualizations that give insight in the spin texture of both degenerate states that belong to the valence band. First the band structure around the X-point is calculated along different lines in $\vec{k}$-space, depicted in figure 4.2. Then, using Matlab, a linear interpolation is used to make an energy band-surface centred around the X-point. For the valence band the band-surface is depicted in figure 4.11.

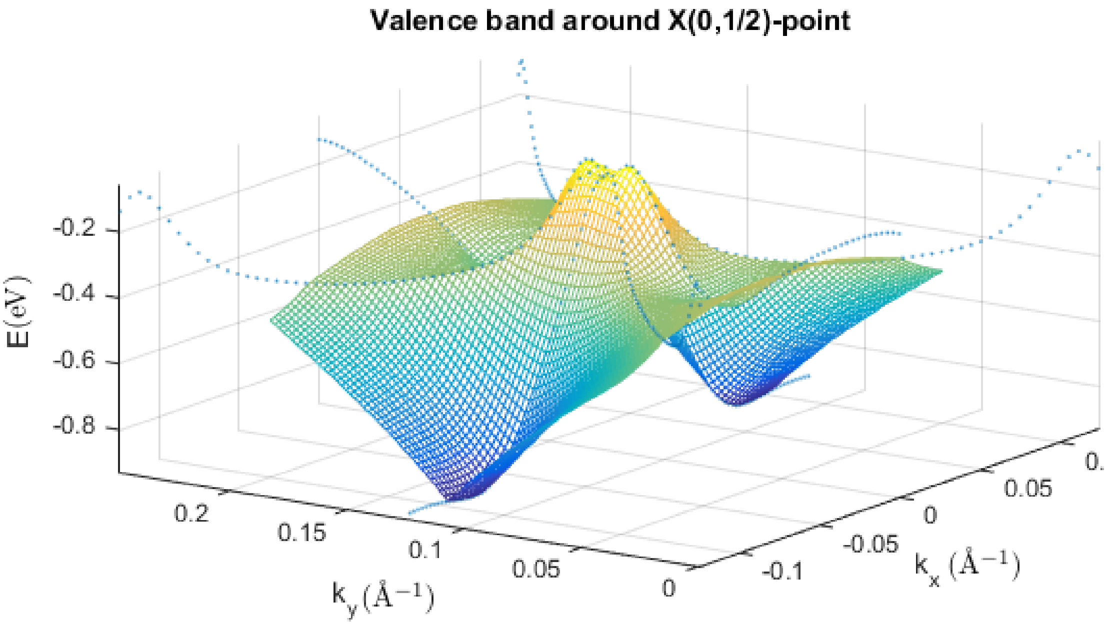

Figure 4.11: Three-dimensional valence band-surface of bulk $LaOBiS_2$, centred around the X-point, obtained by linear interpolation between the calculated Brillouin zone paths.

Next, the spin components of each point along the Brillouin zone paths are visualized as a three-component vector plotted on the band-surface. This is done for both degenerate eigenstates which are coloured red and blue for respectively the first and second state. In this way a spin vector field is obtained, shown in figure 4.12.

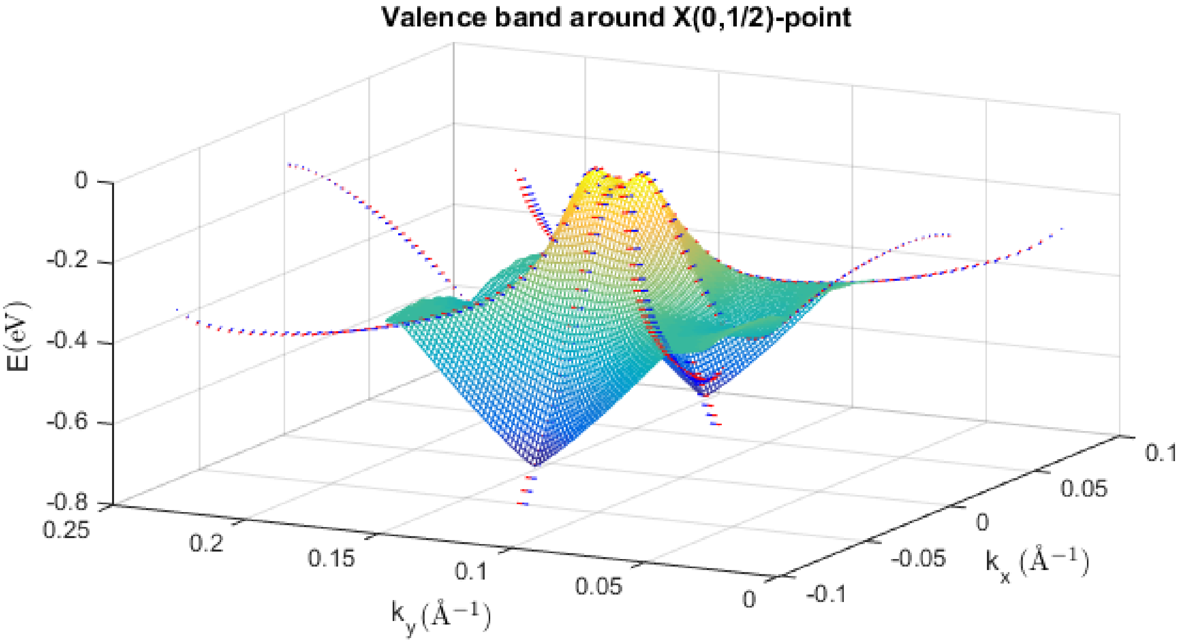

Figure 4.12: Valence band-surface of $LaOBiS_2$ with spin vector field for both degenerate states plotted on top of it. The red and blue arrows correspond to resp. the first and second eigenstate.

These results already show the spin degeneracy of each band. To get a better insight in how the spin texture of both eigenstates looks like, the energy band and the spin vector field are projected onto the (k_x-k_y)-plane. Using the functionality of Matlab to rotate the three-dimensional figure 4.12, it can be seen that in the neighbourhood of the X-point, the spin vectors have a zero z-component, thus no information about the spin is lost by projecting. The result is shown in figure 4.13.

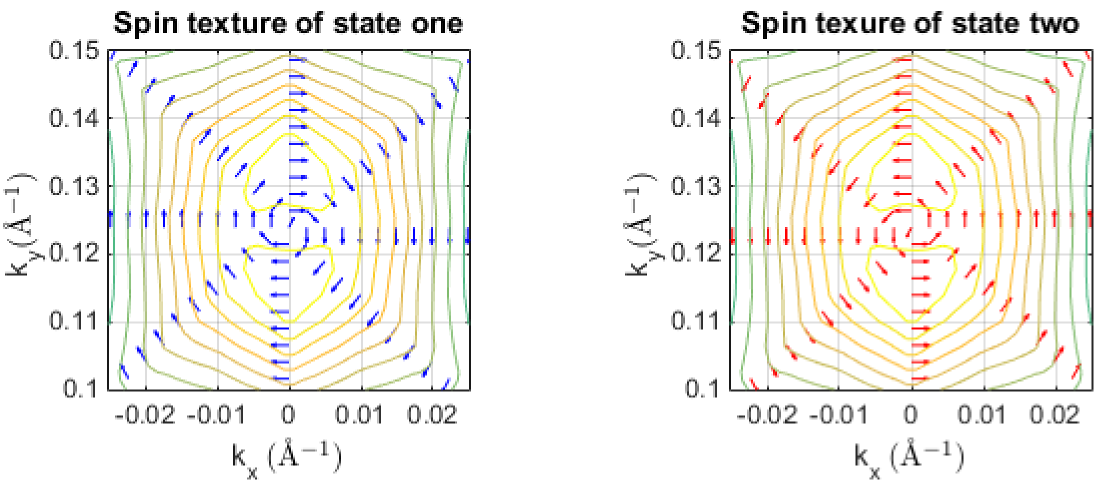

Figure 4.13: Projected energy band and spin vector field. The spin vector fields are plotted separately for the first and the second state. Clear Rashba spin texture is visible for both states.

A clear difference with the conduction band is immediately visible. Each of the eigenstates of the conduction band showed Dresselhaus spin texture, here however a helical Rashba spin texture is visible for both eigenstates, each with opposite sign. This result is a first indication that the valence band shows R-2 spin-orbit interaction. As with the previous case, these spin textures could be a coincidence because it is not a priori clear if they originate from localized states.

To verify this, the localization of both states have to be investigated in the same manner as was done for the conduction band eigenstates. First, consider for both of the eigenstates their spin texture corresponding to the entire unit cell, as depicted in figure 4.13. Then by the use of Matlab for handling the VASP data, the contribution to the spin texture of each atomic layer is plotted. The result is given by figure 4.14.

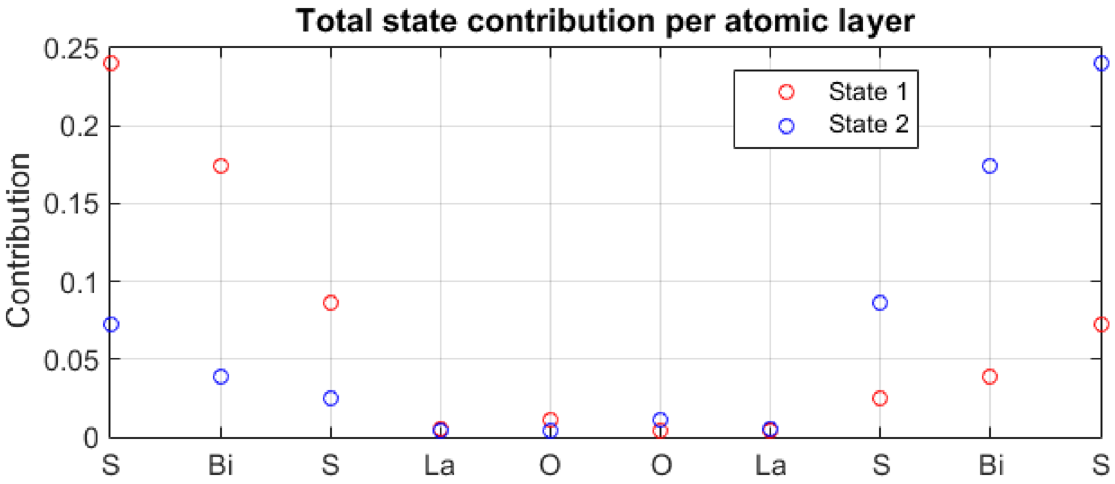

Figure 4.14: Contribution per atomic layer to both degenerate states of the valence band. Localization of state one on the bottom BiS_2-layer.

A clear localization of each state on opposing inversion sectors is clear. The first state is mainly localized on the bottom BiS_2-layer (red) whereas the second state is mainly localized on the top BiS_2-layer. There is a small overlap of contribution between the layers which can be attributed to the interlayer coupling, as the model suggests. For both states however it is clear that the LaO-layer does not contribute to the spin texture.

These results are a firm indicator for the presence of the R-2 hidden spin polarization for the $LaOBiS_2$ bulk valence band. This is in agreement with the model that predicted both the D-2 effect and the R-2 effect to be present, be it on different bands.

The second method considers the spin texture of each sector separately. This is a direct way to obtain the localization of the spin texture from both states. The results are presented in figures 4.15, 4.16 and 4.17, which are the summed spin textures of both eigenstates, localized on respectively the top BiS_2-, LaO- and bottom BiS_2-layer.

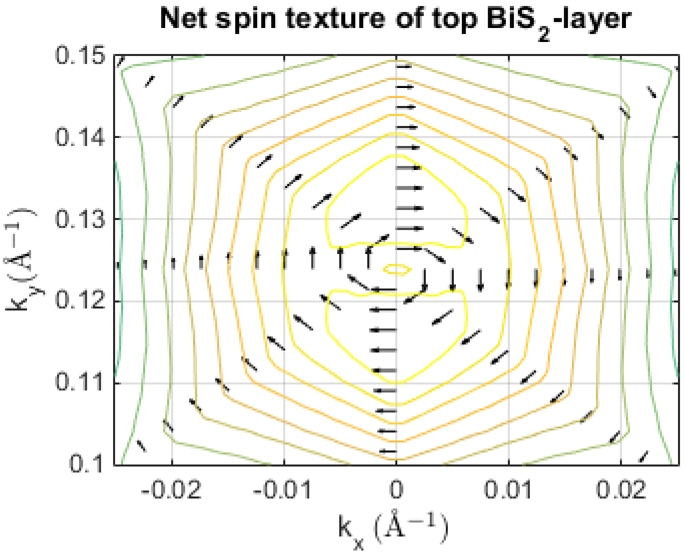

Figure 4.15: Summed spin texture of both degenerate valence band states attributed to the top BiS_2-layer of the unit cell. Clear Rashba spin texture can be seen corresponding to the first state, figure 4.13, left panel.

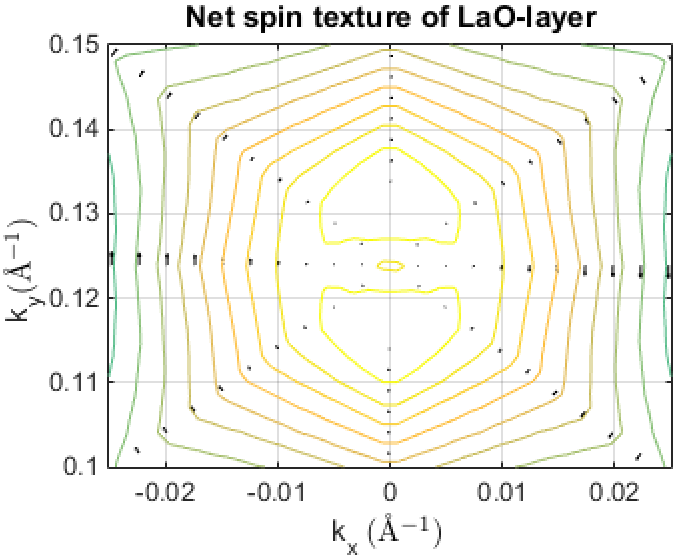

Figure 4.16: Summed spin texture of both degenerate valence band states attributed to the LaO-layer of the unit cell. Both states have zero contribution so this layer is not spin polarized.

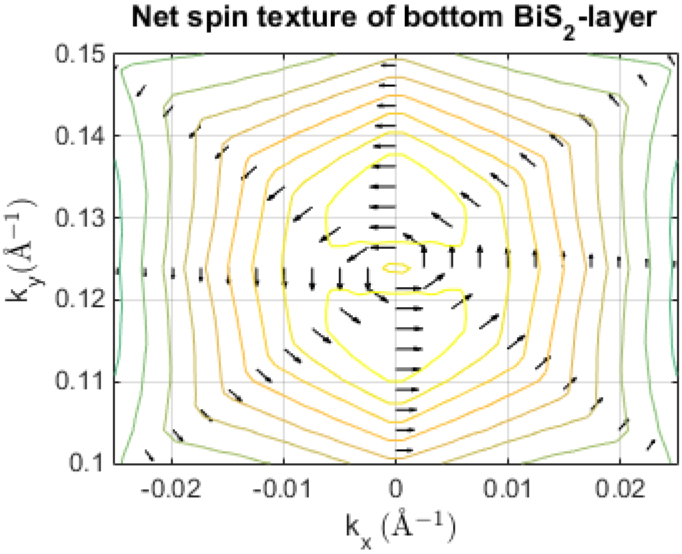

Figure 4.17: Summed spin texture of both degenerate valence band states attributed to the top BiS$_2$-layer of the unit cell. Clear Rashba spin texture can be seen corresponding to the first state, figure 4.13, right panel.

Again, a clear localization of both states is visible. Thus these results establish spatially separated Rashba spin textures with opposite sign, localized on opposing inversion sectors. Likewise with the conduction band, this is what the constructed model predicts. In order to have a pure R-2 effect the spin textures of both states have to cancel each other out when summed over the entire unit cell. This is indeed the case, as shown by figure 4.18.

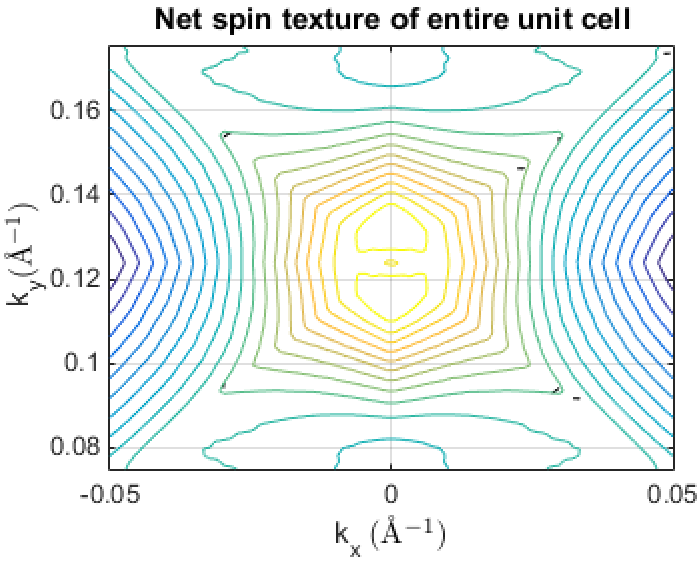

Figure 4.18: Net spin polarization when summed over the spins of both degenerate states belonging to the valence band. It is clear that both spin textures cancel each other perfectly.

4.2 Conclusion on the bulk LaOBiS$_2$ system

It has thus been shown through DFT calculations that the constructed model is correct in predicting both hidden Dresselhaus and Rashba spin textures (D-2 and R-2 respectively) in LaOBiS$_2$. These effects stem from the interaction between the BiS$_2$ inversion pair layers, which have C_{2v} atomic site symmetry. The model only predicts the presence of both the R-2 and D-2 effect, however says nothing about the ratio of both. In the case of LaOBiS$_2$ it turns out that the conduction band exhibits a clear Dresselhaus spin texture, whereas the valence band shows Rashba spin texture.

In the next chapter the extension of the model will be tested by looking at the topological insulator Bi$_2$Se$_3$, where coupling on both sides of the inversion partners is taken into account.

Chapter 5

First-principle studies for Bi_2Se_3

In this part of the thesis DFT studies are performed on the Bi_2Se_3 system which is modelled in section 3.6. In this layered material the active inversion partners are mutually opposing $BiSe_2$-layers. As an extension to the previous chapter of the thesis, these inversion partners are coupled on both sides. Consequently, as the model suggests, two coupling strength parameters determine whether the spin polarization of each layer survives the coupling and brings about localized spin textures.

Bi_2Se_3 is also an interesting material because it is shown both experimentally[21],[24] and theoretically[25] to have topologically protected surface states. Because of this feature, DFT calculations will be performed on the bulk crystal this chapter and a slab system of several QLs which simulates a surface in the next chapter. The spin texture of both systems will be investigated to check whether the model holds in predicting hidden spin polarization. Because the active inversion layers have C_{3v} symmetry, the hidden spin polarization should manifest itself only in the form of Rashba spin textures (R-2 effect).

As was the case for $LaOBiS_2$, the VASP parameters used for the Bi_2Se_3 bulk system are given in appendix III.

5.1 The bulk Bi_2Se_3 system

The bulk Bi_2Se_3 crystal can be described by the supercell depicted in figure 3.5. This is not the primitive unit cell but it is a unit cell that preserves the layered structure of the material. It turned out that when searching for layer-by-layer compensating spin textures, it is convenient to choose a unit cell that contains the layered structure of the crystal. The supercell contains fifteen atomic layers which form in total three complete QLs.

Finding the lattice parameters and atomic positions for the Bi_2Se_3 crystal is done in the same manner as for $LaOBiS_2$. The initial values are abstracted from literature[26] and starting from these, the lattice is relaxed iteratively while the atomic position are predetermined by symmetry. The following table is the result and contains the relaxed lattice parameters and atomic positions.

Lattice parameters in Å			
a=b	4.24		
c	29.29		
Atomic position in relative coordinates			
Bi_1	(0,0,0.398)	Bi_2	(0,0,0.602)
Bi_3	(0.667,0.333,0.731)	Bi_4	(0.667,0.333,0.935)
Bi_5	(0.333,0.667,0.065)	Bi_6	(0.333,0.667,0.268)
Se_1	(0,0,0)	Se_2	(0.667,0.333,0.333)
Se_3	(0.333,0.667,0.667)	Se_4	(0,0,0.212)
Se_5	(0.,0,0.789)	Se_6	(0.667,0.333,0.545)
Se_7	(0.667,0.333,0.122)	Se_8	(0.333,0.333,0.878)
Se_9	(0.333,0.667,0.455)		

Table 5.1: Table with converged values of the bulk Bi_2Se_3 supercell. Values truncated.

The Brillouin zone of this specific hexagonal unit cell, figure 3.5, is itself hexagonal and depicted in figure 5.1 together with the projected Brillouin zone along the b_3-axis. This axis corresponds to the unique anisotropic axis in the crystal which facilitates the net polar field inducing Rashba spin-orbit coupling effect. The projected Brillouin zone will be used later on for the study on the slab-system.

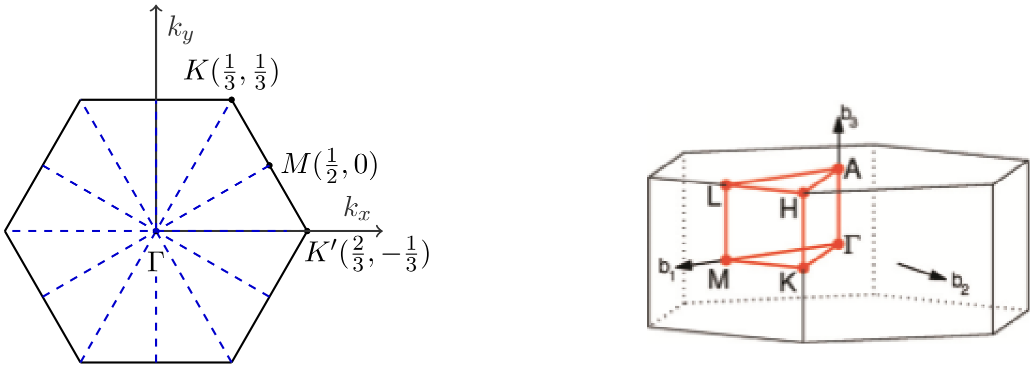

Figure 5.1: Both the 3D (right) and projected (left) Brillouin zone of the hexagonal supercell of the bulk Bi_2Se_3 crystal. The projected Brioullin zone will be used as the Brillouin zone of the slab Bi_2Se_3 system representing a surface and is discussed in the next chapter. The paths along which the energy dispersion and spin vector field are calculated are represented by blue dashed lines.

5.1.1 Band structure

To get an indication of which paths in $\vec{k}$-space will give useful information about the spin texture of the material, the band structure along the A-Γ-K-Γ-M-L path is calculated. The result is shown in figure 5.2 and indicates that the band gap is situated around the Γ point.

Because the expected Rashba spin texture relies on the presence of the unique anisotropic z-axis in real space, the paths in a plane parallel to the the K-Γ-M plane in $\vec{k}$-space will

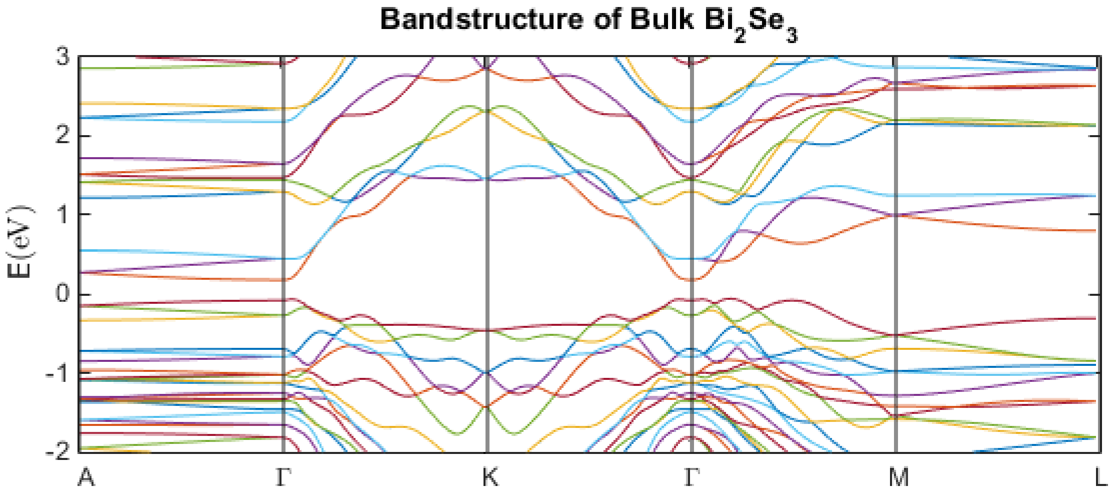

Figure 5.2: Band structure of bulk Bi_2Se_3 using the hexagonal supercell. Band gap is situated at the time reversal invariant Γ-point. The zero of energy is chosen to be the fermi energy level at the top of the valence band.

be studied. This is because the spin texture of interest is the one inside the atomic sectors, perpendicular to the real space z-axis. Different parallel (k_x-k_y)-planes are possible, all with different b_3 values.

However, because the conduction electrons are of interest, the plane in which the band gap is the smallest will be chosen. To check this, the band structure along the K-Γ-M path will be calculated for $b_3 = 0$ and $b_3 = 0.5$ in relative coordinates, see figure 3.5. This results in figure 5.3 left and right panel, respectively.

From these band structures it can be seen that in the case where $b_3 = 0$, the band gap is the smallest. Thus, for the following analysis, the K-Γ-M path at $b_3 = 0$ will be considered in the calculations.

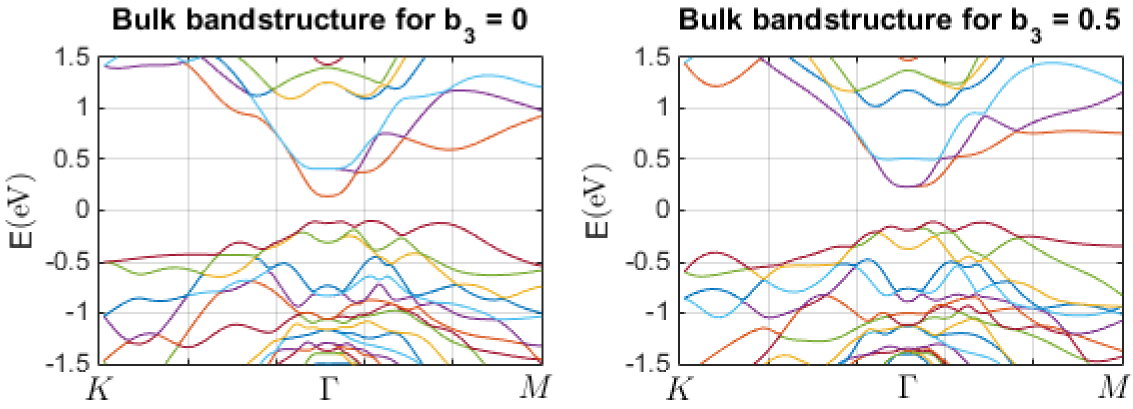

Figure 5.3: Band structures of bulk Bi_2Se_2 along the K-Γ-M path at $b_3 = 0$ (left panel) and $b_3 = 0.5$ (right panel).

5.1.2 Conduction Band

Now that the different paths in $\vec{k}$-space are determined, a two-dimensional band-surface is obtained in the same manner as before. The energy of each point along the BZ-paths will be calculated and plotted on a three-dimensional figure. The spacing in between the $\vec{k}$-point samples is interpolated by means of linear interpolation.

From the DFT calculations it follows that the band-surface is doubly degenerate. To check whether these degenerate states have opposite spin and to get a first hint of how the spin texture looks like, the spin vector field is plotted onto the band-surface for each of the degenerate states. This vector field represents the direction of the spin of a certain state along the sampled $\vec{k}$-points by means of a three-dimensional vector. This procedure results in figure 5.4.

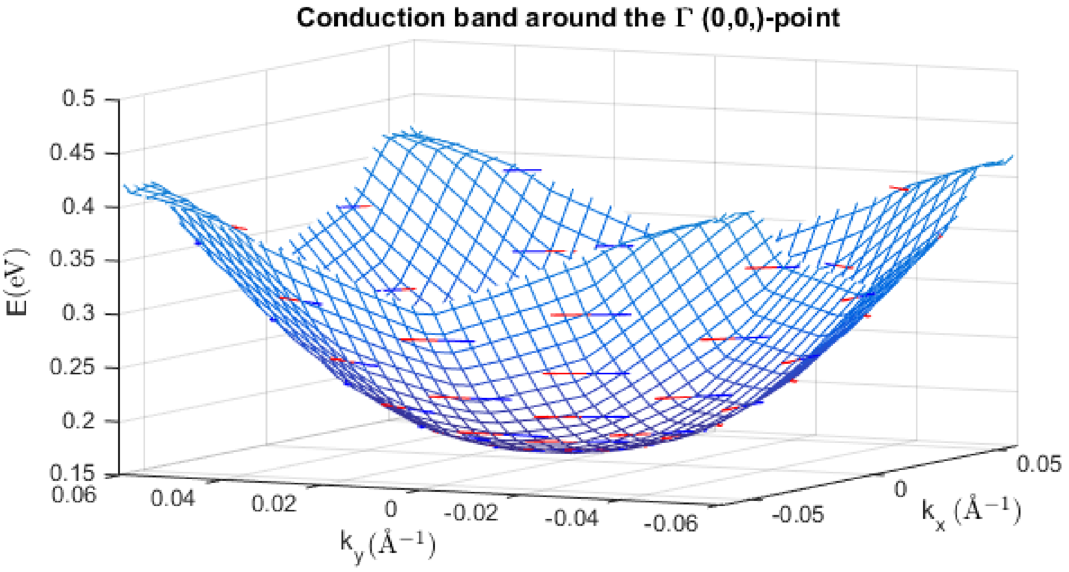

Figure 5.4: Three-dimensional band-surface for the conduction band around the Γ-point with the spin direction of each sampled state plotted onto in.

As a verification, this representation shows the spin degeneracy of the band-surface and is helpful to give a first impression of how the spin texture looks like. By rotating the three-dimensional figure in a matlab environment it is clear that near the Γ-point a Rashba spin texture emerges for each of the degenerate states. To get a better and more detailed insight in the spin vector field, the band-surface and the vector field are projected onto the (k_x-k_y)-plane. The band surface becomes a contour plot and the three-dimensional spin vector field becomes two-dimensional.

As before, it needs to be checked that the spin direction in the area under consideration does not have a z-component in order not to lose valuable information by projecting. This might not be clear from the static figure 5.4 but it can be seen that it is the case by rotating the surface in a Matlab environment.

For both of the degenerate states this projection is done and results in the following figure 5.5.

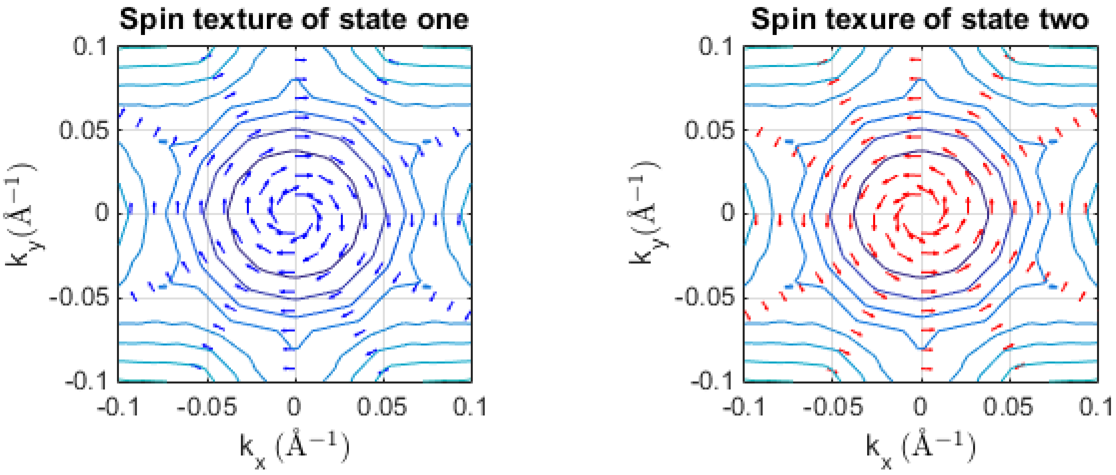

Figure 5.5: Projected spin vector fields of both degenerate states summed over the entire unit cell. Both states clearly show their own Rashba spin texture.

The objective is to find compensating, localized Rashba spin textures. Thus far for Bi_2Se_3 two degenerate states have been identified with each having its own, opposite in sign, Rashba spin texture. This is clearly seen from previous figure 5.5. However, these spin textures could originate from linear combinations of two states that are not at all localized on one of the two real space sectors. Consequently to determine whether Bi_2Se_3 exhibits R-2 behaviour, as the model predicts it is able to, the real space localization of both degenerate eigenstates has to be checked.

To do this, the contribution of each atomic layer to both of the degenerate eigenstates is plotted. This gives an indication of which atomic layers contribute the most to the Rashba-type eigenstates, and thus determine the localization of both states inside the supercell. The result, per state, is depicted in figures 5.6 and 5.7.

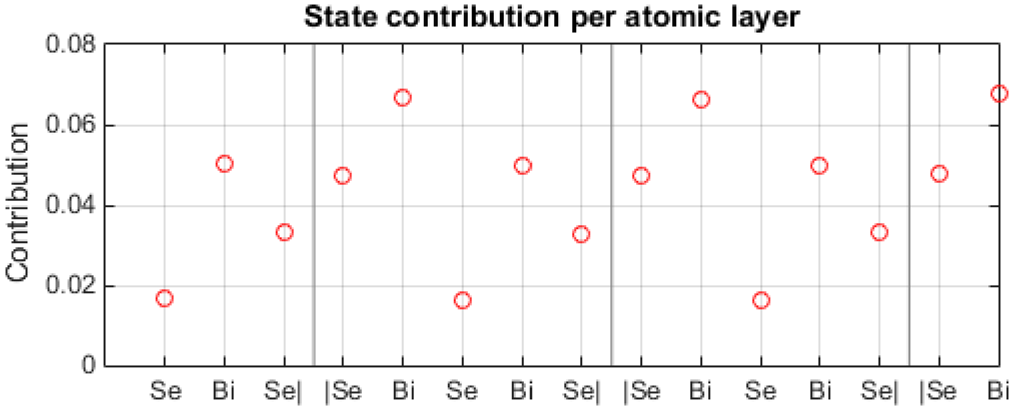

Figure 5.6: Contribution to the first state per atomic layer throughout the unit cell. The grey lines indicate separation between the QLs through Van Der Waals interaction between neighbouring Se-atoms.

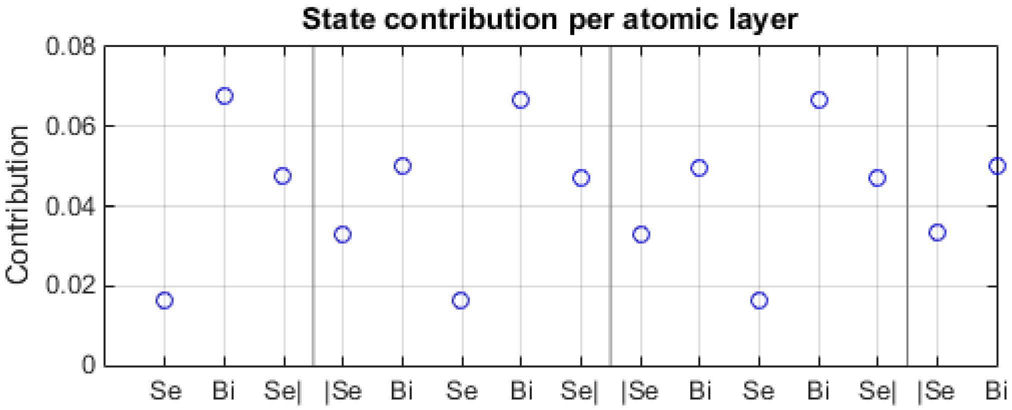

Figure 5.7: Contribution to the second state per atomic layer throughout the unit cell. The grey lines indicate separation between the QLs through Van Der Waals interaction between neighbouring Se-atoms.

At first sight and in comparison to the corresponding figures of the $LaOBiS_2$ case, both the degenerate states seem not to be localized as much. Even linear combinations of the degenerate states cannot result in localization of both states. This can be understood by considering that the inversion partners in Bi_2Se_3 are more strongly bound to each other through the single-atomic Se-layer than the inversion partners of the $LaOBiS_2$ material where the coupling was mediated through Van Der Waals interaction.

As the model predicted, when the coupling between two inversion partners increases, the states will mix and localization will be partly lost. However, despite this mixing of states, and thus of spin textures, it is still possible that the sector's total spin still exhibits a characteristic texture albeit much weaker.

So the idea that the model puts forward is that even though there is some mixing between both degenerate states, the bi-atomic inversion layers still maintain a weak spin polarization under the form of Rashba spin texture. To verify this, the total spin texture is calculated by summing for each $\vec{k}$-point the spin expectation values of both degenerate states. The results are represented for both sectors A and B, resp. upper and lower layers, (see figure 3.5) and the coupling Se-layer, in figures 5.8 - 5.10.

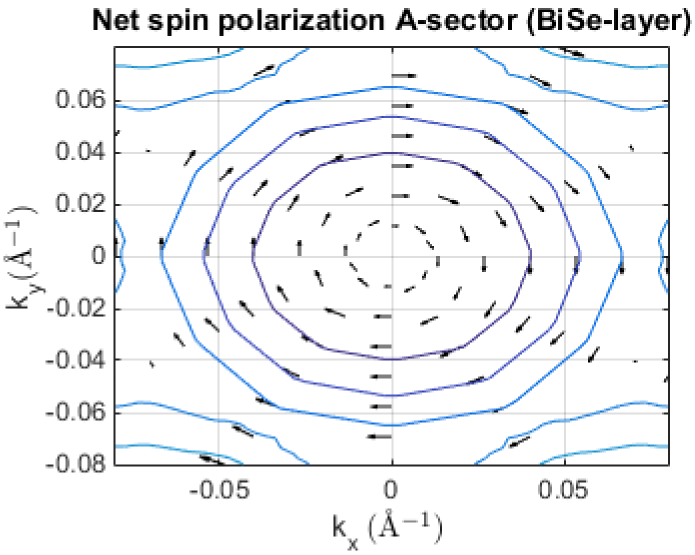

Figure 5.8: Total net spin expectation values, localized on the A sector of the inversion pair (BiSe-layer). Clear Rashba spin texture is visible, corresponding to state one depicted in figure 5.5, left panel.

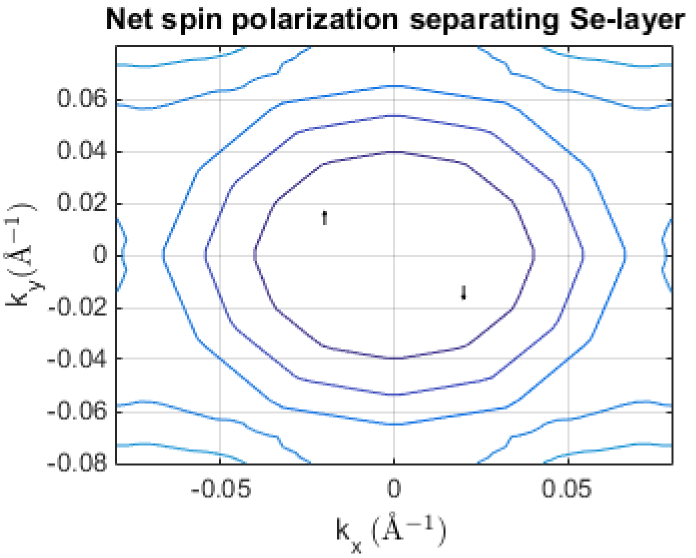

Figure 5.9: Total net spin expectation values, localized on the separating single Se-atomic layer. No spin texture is visible.

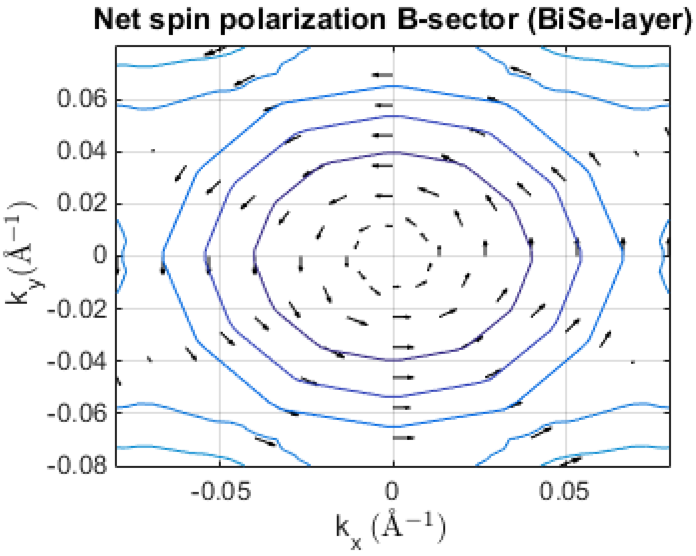

Figure 5.10: Total spin net expectation values, localized on the B sector of the inversion pair (BiSe-layer). Clear Rashba spin texture is visible, corresponding to state one depicted in figure 5.5, right panel.

These figures show that both sectors A and B each still have their own spin polarization in the form of Rashba spin textures, each with opposite sign. However, compared to the magnitude of the polarization in the $LaOBiS_2$ system, figures 4.7 - 4.9, these are much weaker. As anticipated, this is due to the fact that both states mix with each other and spin textures partly compensate on a point-by-point basis on the real space sectors which consequently lowers the net spin polarization per sector.

So, localized spin polarization in the form of Rashba spin texture is present in the bulk Bi_2Se_3 material. The final criterion of the R-2 effect that needs to be verified is whether the spin polarization vanishes when all the spins are summed over the entire unit cell. Moreover, the way the crystal is modelled (figure 3.5) the total spin should also vanish when summed over a full QL. Both cases are easily calculated and represented in figure 5.11.

Both spin polarizations turn out to vanish and all the criteria for the R-2 effect are met. This discussion showed that in the case of strong coupling between the two inversion partners, even though both degenerate states overlap, hidden spin polarization still takes place albeit in a weaker form.

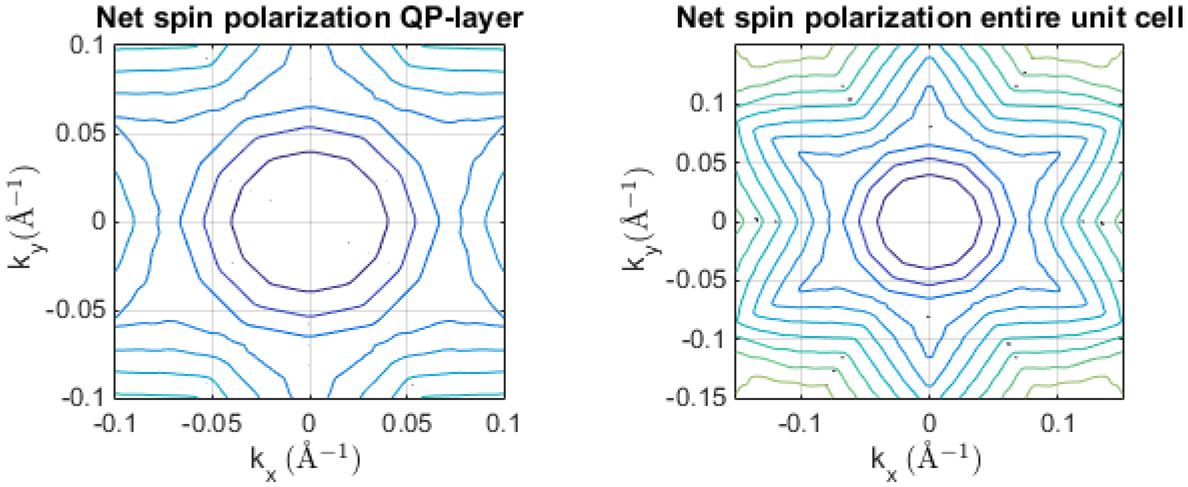

Figure 5.11: Total spin vector field summed over one QL (left panel) and the entire unit cell (right panel). All the spins cancel each other out and no net spin polarization is present.

5.1.3 Valence Band

The previous analysis can be performed in an analogous way for the valence band. Because of this, the now familiar representations and figures will need little explanation. The sampled $\vec{k}$-points in the Brillouin zone that are used to construct the band-surface are the same as the ones used for the conduction band and can be seen in figure 5.1. These are used to create the valence band-surface.

The valence energy surface will be used to visualize the spin vector field in order to get a first impression of its nature. A three-dimensional vector represents the spin associated with each degenerate state corresponding to each of the sampled $\vec{k}$-points. This results in a vector field that describes the spin texture, depicted in figure 5.12.

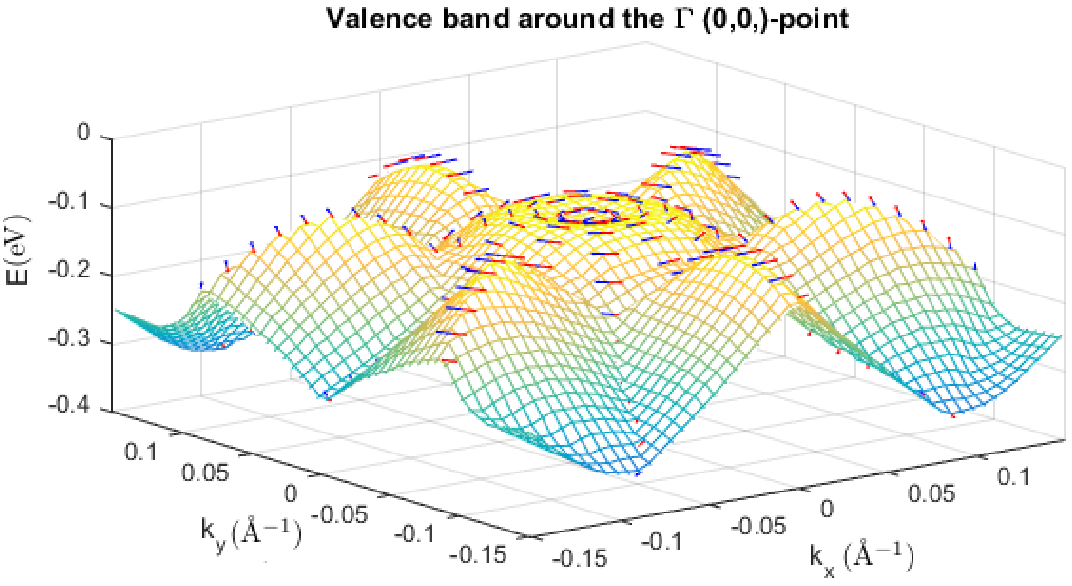

Figure 5.12: Valence Band surface with the spin expectation values for each $\vec{k}$-point plotted onto it.

From this figure it can be seen that the energies are indeed, again, spin degenerate and that each degenerate state produces its own helical Rashba spin texture, both with opposite sign. However, as mentioned several times now, these spin textures are not necessarily localized on the inversion partners. They could very well be obtained by taking a specific linear combination of degenerate states.

To check whether the spin textures are indeed localized on the inversion partners in real space, the spin vector fields of each sector separately are calculated by summing the spin expectation values of both degenerate states and plotted in the now familiar projected representation. As usual, it is verified that no information about the spin components is lost due to projection by confirming that in the region around the Γ-point the spins have no z-component.

The following figures 5.13-5.15 show the spin textures of respectively the A-sector, separating mono-atomic Se-layer and the B-sector in one of the QLs in the unit cell. They are obtained by summing the spins of both degenerate states, weighed by the contribution of the specific atomic layers to the corresponding state.

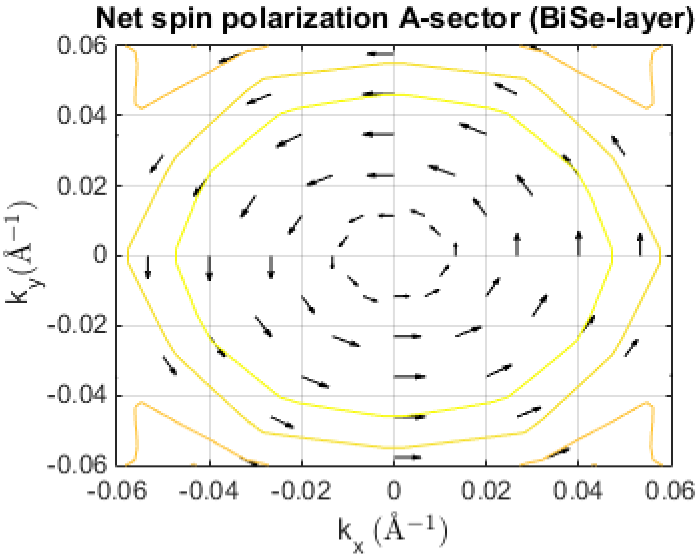

Figure 5.13: A two-dimensional projected representation of the net spin texture that is localized on the A-sector of one of the two QLs in the unit cell. A clear Rashba spin texture is visible around the Γ point.

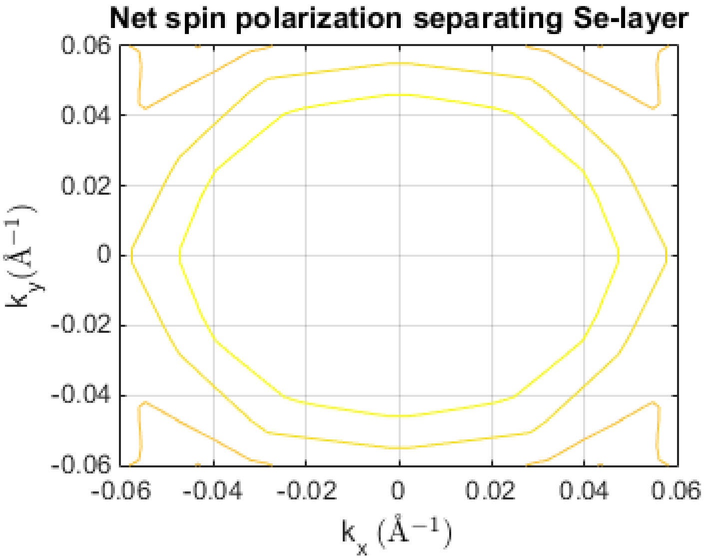

Figure 5.14: A two-dimensional projected representation of the net spin texture that is localized on the single atomic Se-layer that functions as a separating layer between the two inversion layers of one of the two QLs in the unit cell. This atomic layer has a spin texture that is negligible.

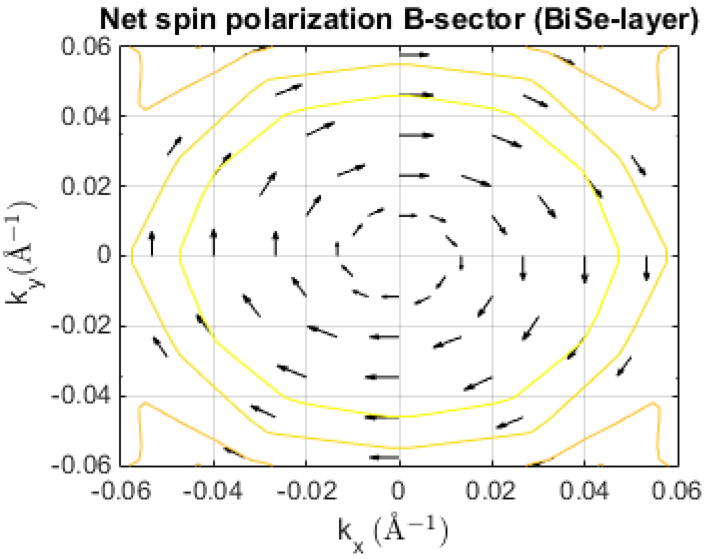

Figure 5.15: A two-dimensional projected representation of the net spin texture that is localized on the B-sector of one of the two QLs in the unit cell. A clear Rashba spin texture is visible around the Γ point which is opposite in sign than that of the corresponding inversion partner (B-sector).

From these figures the spacial separation of Rashba spin textures of opposite sign can be clearly seen. So again, even though the degenerate eigenstates are mixed due to the stronger coupling between the inversion layers, still a net spin polarization remains that is localized on each one of the real space sectors.

The last criterion of the R-2 effect that needs to be verified is whether the total spin polarization of the crystal is zero, and thus hidden. This can be easily checked by summing the spin textures of each degenerate state over the entire unit cell. Moreover, because of the way that Bi_2Se_3 is built up by QLs, the model predicts that each QL itself has a vanishing net spin polarization. In figure 5.16 both the spin polarization of the QLs and the entire unit cell is plotted.

5.1.4 Conclusion for the Bi_2Se_3 system

In this chapter the results of DFT calculations on a bulk Bi_2Se_3 system show that this material exhibits hidden Rashba spin polarization that is localized on real space sectors A and B, separated by a single Se atomic layer on one side and by Van Der Waals interaction on the other side. Consequently all of the characteristics of the R-2 effect are present. Moreover, when more energy bands are investigated, only Rashba spin textures are obtained, which the model predicted as a consequence of the C_{3v} atomic site symmetry of the sectors.

The strong coupling between the layers results in a mixing of the degenerate states which leads to an overlap in contribution to each atomic layer. Nonetheless localized spin textures survive and hidden spin localization remains present in the form of the R-2 effect, albeit with less strength than for the $LaOBiS_2$ crystal.

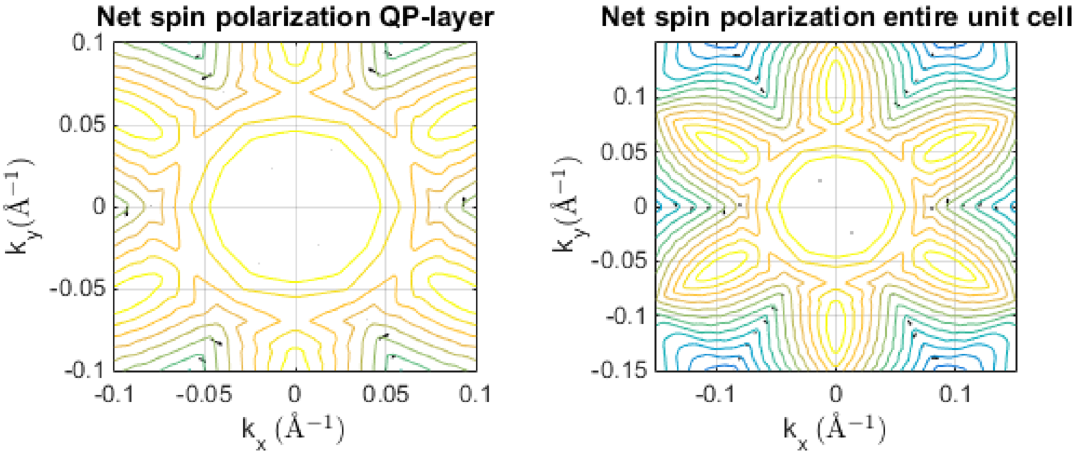

Figure 5.16: The net spin polarization of the QL (left panel) and the entire unit cell (right panel). Both show vanishing spin polarization, as predicted by the model.

Chapter 6

First-principles studies for surface systems

In the previous chapters of this thesis the hidden spin polarization in centrosymmetric bulk materials in the form of D-2 and R-2 effect has been modelled theoretically and verified with DFT calculations on both LaOBiS_2 (C_{2v}) with its weakly coupled inversion partners and Bi_2Se_3 (C_{3v}) with its strongly coupled inversion partners. In this chapter, finite systems are studied to see whether the presence of surfaces will in some way influence the hidden spin polarization characteristics of the bulk. These finite systems consist of several units, in the case of Bi_2Se_3 those will be quintuple layers (QLs) and in the case of LaOBiS_2 the units will consist of two BiS_2 sectors separated by a LaO_2 layer. In this way a slab system is obtained with two surface layers and several bulk layers in between. Because of the absence of a corresponding model that incorporates surfaces, this chapter will be treated more heuristically.

6.1 The Bi_2Se_3 slab system

As mentioned before, it is well established that Bi_2Se_3 has topologically protected surface states. Even though the model constructed in this thesis only covers bulk systems, it is nonetheless interesting to study its surface states and see how well the bulk characteristics of the R-2 effect remain visible and compare them later on with non-topological states.

A topological insulator has two main characteristics and thus two aspects that should be looked for with first-principles studies on the slab system. The first characteristic is that a topological insulator acts like an insulator in the bulk but has conducting surface states. The bulk insulator is already verified by the previous sections on the bulk Bi_2Se_3 system which showed a band gap around the Γ-point. The band structure of the slab system should exhibit a closing of the band gap at the Γ-point, indicating that conducting states are present. To check whether these conducting states are localized on the surface of the slab system, the tools from previous sections will be used to visualize the contribution of each atomic layer to each of these conducting states.

The second aspect is the presence of spin-momentum locking. As explained in section (2.5) of this thesis, this property links the direction of crystal momentum $\vec{k}$ of the electrons with the direction of their spin. In other words, around the Dirac point, the electrons with opposite crystal momentum have opposite spin, as depicted in figure 2.5.

Along with these typical topological insulator characteristics, it is then interesting to study the local spin texture of the conduction band bulk slab to look for a possible link between the spin textures of the surface states and those belonging to the bulk states as described in the previous chapter.

6.1.1 Band structure

Since the slab system does not have periodicity in the stacking direction, the corresponding Brillouin zone is the projected Brillouin zone of the bulk system. The projected Brillouin zone is depicted in figure 5.1 in section (5.1), which also shows that the K-Γ-M path describes the irreducible Brillouin zone and thus is representative to describe the slab band structure.

The goal is to simulate the surface states as truthfully as possible while keeping the number of QLs as low as possible. The latter poses a restriction due to the fact that the more atomic layers are present in the super cell, the heavier the computational calculations become. Also, because the local spin textures are studied on an atomic layer scale, it is advantageous to have a low number of QLs to make it more feasible to process and interpret the data.

A good indication to probe whether the number of layers is adequate and the surface states are present, is to increase the number of QLs until the band gap at the Γ-point closes, or is sufficiently small. In figure 6.1 the band structure of the slab system is plotted for a four, five and six QL slab system.

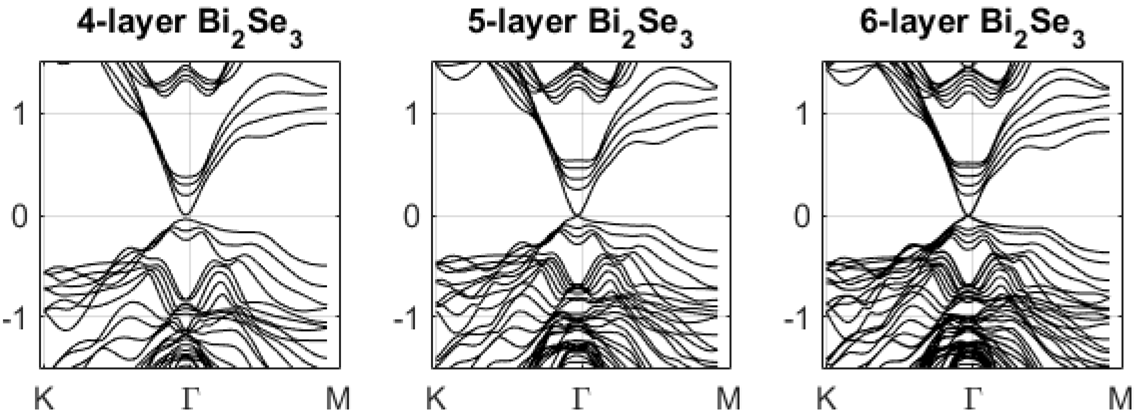

Figure 6.1: The band structure of the slab system with four, five and six QLs (from left to right). These give an indication of how many layers are needed to simulate the surface states truthfully. The zero of energy is chosen to be the fermi energy level at the top of the valence band.

The band structures show a clear evolution concerning the closing of the band gap when the number of QLs increases. The system with four QLs still has a band gap while for the five and six layered system the band gap seems to close. However, zooming in around the Γ-point reveals that there is still a very small band gap in the range of meV but this will be considered as numerical negligible.

The explanation of this evolution of the band gap between surface bands as a function of number of QLs goes as follows. If there are too little QLs separating the surface layers, the states that should be localized on the surface extend through the bulk to the other surface, overlapping in the process and opening the band gap due to creation of bonding and anti-bonding levels. Only when the spacial separation between the surfaces is large enough, by increasing the number of QLs, the surface states do not overlap and the bands remain closed at the Γ-point.

Figure 6.1 also shows that there are several conduction- and valence bands that can be considered as bulk bands. This is most clear for the bands just above and below respectively the conduction and valence band. These bands are similar to the bands of the bulk system in figure 5.3. Moreover, it can be seen that each time a QL is added to the system, another bulk band of the same form is added to the band structure.

To avoid confusion some terminology is introduced concerning the different bands. The bands that correspond to the surface states will be referred to as the surface conduction (valence) band. The lowest (highest) conduction (valence) band corresponding to bulk states will accordingly by called the bulk conduction (valence band).

Now that the closing of the band gap is established, the second aspect of topological insulation can be looked for. This means that the localization and spin textures of the states that correspond to the surface conduction and valence band need to be visualized in order to get more insight. This is done with the same tools used in the previous chapter. The discussion of both the localization and spin textures together will show a deviation from the bulk model that has proven its validity up until now.

Due to the band gap in the four-layer system and the convergence problem for the six layer system, the five-layer system will be used as proto-type example for the Bi_2Se_3 slab system.

6.1.2 Surface conduction state

In this section the spin texture and localization of states corresponding the the surface conduction band around the Γ-point in figure 6.1 will be studied. This will be done in the same manner as before by first visualizing the conduction band-surface as an interpolation of the sampled $\vec{k}$-points along the paths in the projected Brillouin zone. The result is depicted in figure 6.2.

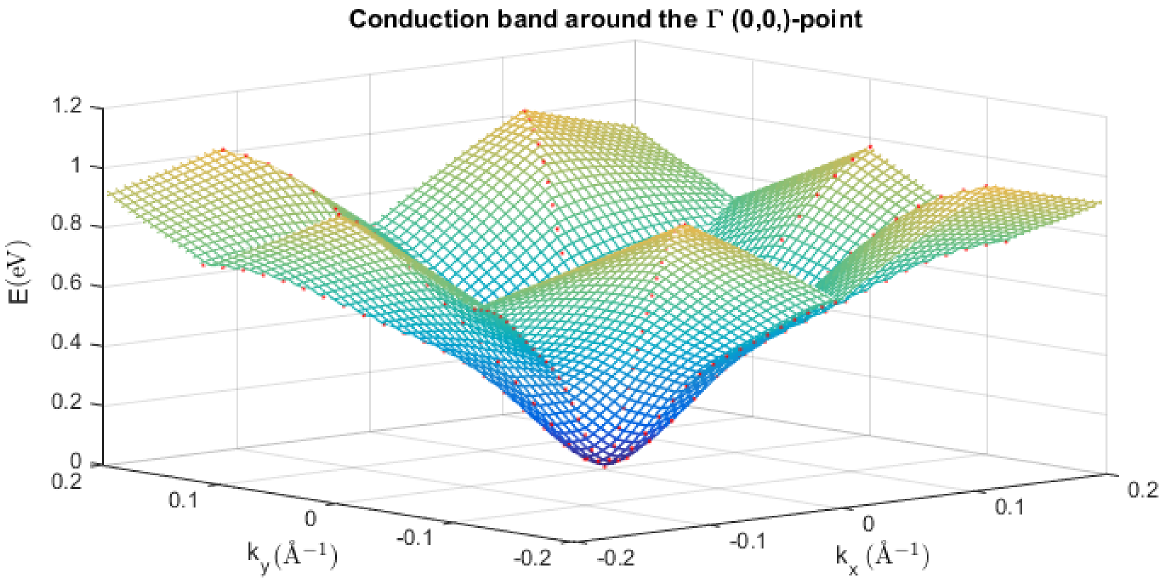

Figure 6.2: Surface conduction band-surface around the Γ-point for the Bi_2Se_3 slab system. It is obtained by plotting the energy for each $\vec{k}$-point along the paths crossing (k_x, k_y)=$(0, 0)$. The spacing between the points is linearly interpolated.

To get a first insight of how the spin texture looks like the same procedure as before is followed. For each $\vec{k}$-point a three-dimensional spin vector is plotted onto the band-surface, resulting in the spin vector field depicted in figure 6.3.

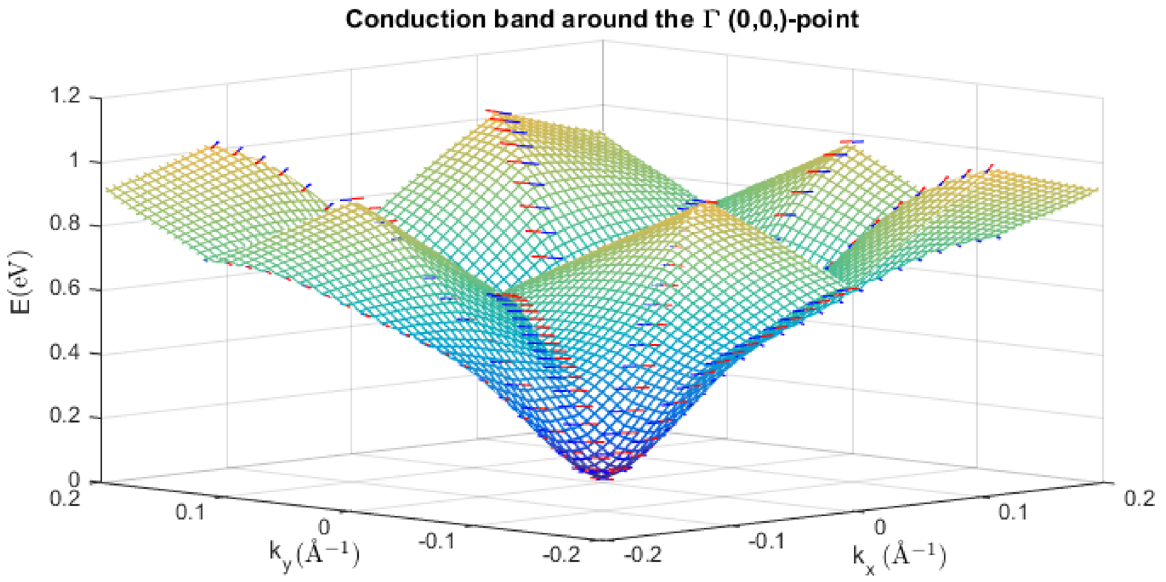

Figure 6.3: Surface conduction band-surface around the Γ-point with the spin vector field of the corresponding eigenstates plotted onto it.

Figure 6.3 shows that the conduction band-surface is spin degenerate and that both degenerate states exhibit their own Rashba spin texture, each with opposite sign. To make this more visible, and because the spin vector field does not have a z-component in the region of interest, the band-surface and its spin vector field is projected onto the (k_x-k_y)-plane. This operation results in figure 6.4 for both degenerate states separately.

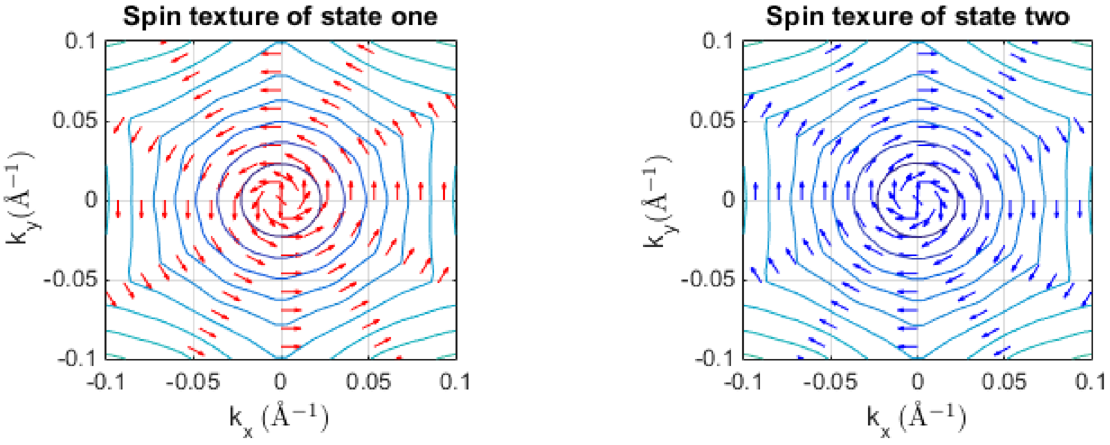

Figure 6.4: Projected representation of the surface conduction band-surface and its spin vector field, plotted for both degenerate states separately.

Now the Rashba spin texture of both eigenstates is even more clear. However, as in the previous chapter, caution is needed here because this specific spin textures could just as well be obtained by taking a linear combination of two other degenerate eigenstates. Consequently, on its own figure 6.4 does not give much conclusive information about the spin texture. To give this figure its value, it needs to be accompanied by a figure that shows the localization of both degenerate eigenstates. This can be done by showing the contribution of each state per atomic layer of the system, depicted in figure 6.5.

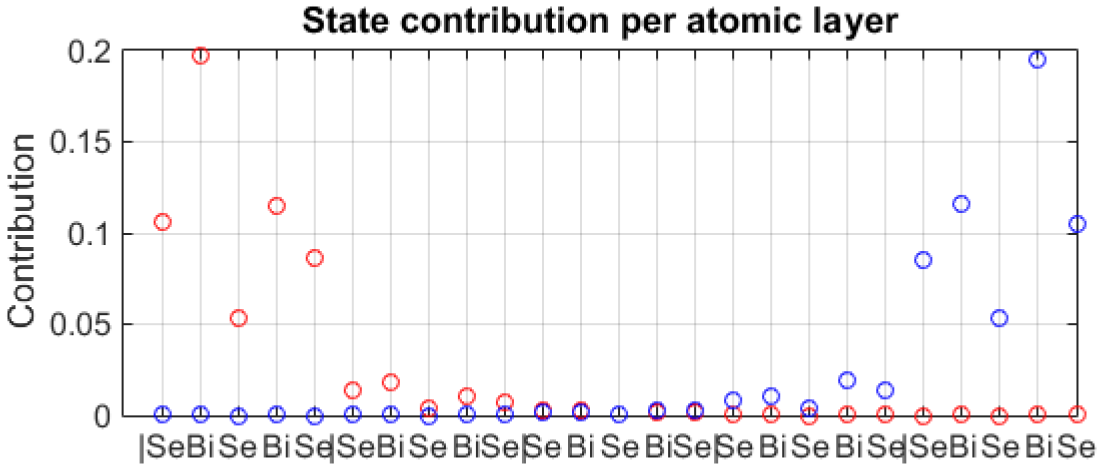

Figure 6.5: Contribution of each atomic layer to both degenerate states exhibiting the Rashba spin textures. A clear localization at the surface QLs is visible, a first deviation from the bulk system that was studied.

Figure 6.5 indicates a first deviation of the model constructed for the bulk Bi_2Se_3 system. It shows for both degenerate states a strong localization, each on opposite surfaces of the slab system. The QLs that are not situated at the surface hardly contribute to neither of the degenerate states. This is in contrast to the bulk system where each QL as a whole contributed equally to the eigenstates. Moreover, as the model predicted, each equivalent sector (BiSe-bilayer) contributed equally to each state, as was visible in figures 5.6 and 5.7.

It seems that the presence of a surface suppresses the bulk contribution and enhances the surface contribution to both degenerate states. It is also clear that any linear combination of the two eigenstates will result in localized surface states. This founding, together with the closing of the band gap shows the topological insulator character of Bi_2Se_3 as in the presence of conducting states which are localized at the surface. Moreover, it can be seen that these surface states exhibit spin polarization in the form of Rashba spin textures. This is the previously discussed spin-momentum locking.

6.1.3 Spin Texture of the surface conduction state

It is clear from figure 6.5 that the contribution of each atomic layer to the degenerate eigenstates is different from those of the bulk system. Naturally it is to be expected that the spin localization per atomic layer will also differ. As a reminder, in the bulk system each QL on its own has hidden spin polarization, i.e. each QP shows no net spin polarization. In other words, each five-layer system consists of two bi-layer sectors that have localized Rashba spin texture of opposite sign. The separating Se-atomic layer had negligible spin texture.

For the slab system this is different. From figure 6.5 it was found that the states exhibiting Rashba spin texture are localized almost entirely on the surface QLs. This indicates that the entire QLs on the surface have a net spin polarization. Also, the QLs separating the surface layers show close to no contribution to the spin texture.

To make this all more visible the local spin textures are calculated at different scales. First at an atomic layer scale, where the local spin texture is calculated for each atomic layer that constitutes one of the surface QLs. The result for the bottom QL is depicted in the different plots of figure 6.6.

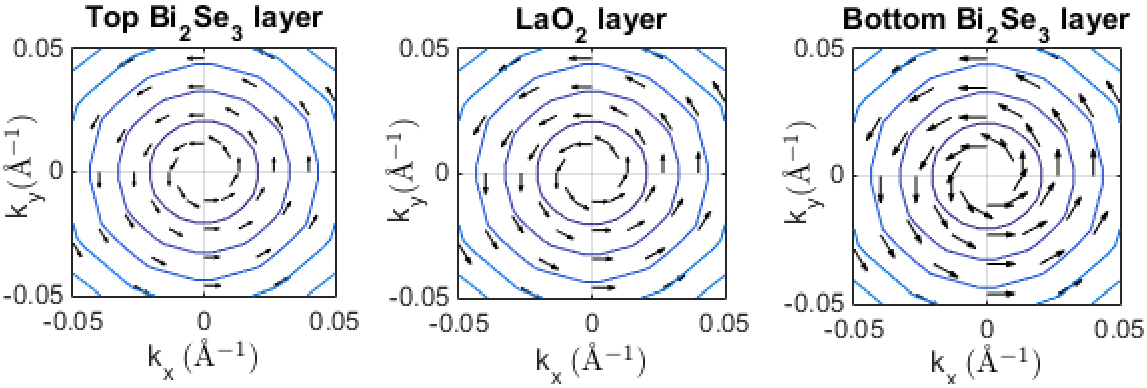

Figure 6.6: Local spin textures per inversion sector of the bottom surface QL obtained by summing over the spin expectation values of both degenerate conduction states.

These results show the clear difference with the bulk system (figures 5.8-5.10). Every sector constituting this surface QL shows a Rashba spin texture with the same sign. There is no mutually cancelling of spin textures within one QL and thus the whole QL has a net spin polarization in the form of Rashba spin texture. So near the surface of the material, the surface states seem to force hidden spin polarization to be diminished.

However, figure 6.5 hints, due to its symmetry, that nonetheless the total spin of the entire slab system should vanish. To investigate this, the local spin textures are calculated at a larger scale, namely for each QL as a whole. Figure 6.7 shows the spin textures of each of the QLs in the slab system, from bottom to top. These are obtained by summing over all the spin contributions of the atomic layers constituting a QL.

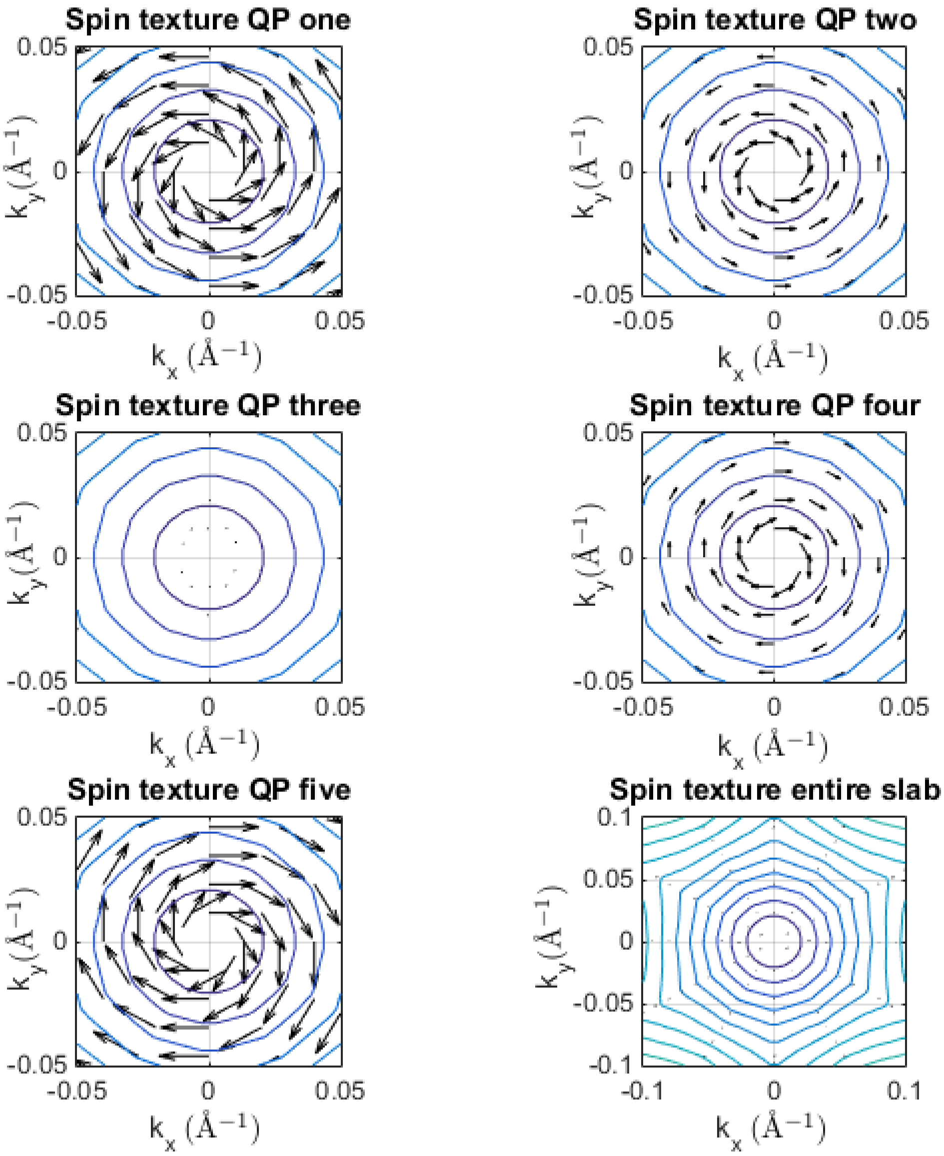

Figure 6.7: Local spin textures per QL, quintuple layer one to five from bottom to top. The total sum of all the spins over the entire slab system depicted in the lower right panel.

The lower right of figure 6.7 shows that indeed the total spin polarization of the entire slab system vanishes. The other panels show the mutual cancellation of spin textures between entire QLs. The middle QL shows no spin polarization at all and further study shows that in fact each of the atomic sectors constituting this QL have negligible spin polarization.

These findings show that instead of hidden spin polarization *within* one QL by mutually cancellation of spin textures on atomic sectors, for the slab system each QL can have a net spin polarization and these will mutually cancel with other QLs to result in hidden spin polarization for the entire system. Note that the spin polarization of the entire system should indeed vanish as it is a centrosymmetric system with time-reversal symmetry, as discussed in chapter one.

The results also show that the spin textures of the conducting states on opposite sides of the slab system are opposite in sign. This indicates that spin-momentum locking is present on both surfaces of the slab system, but with opposite sign.

6.1.4 Surface valence state

For the surface valence band the same procedure is followed and similar results are obtained. Consequently in this section the figures are rather briefly discussed since no new insights are obtained except for the verification of previous results.

The energy is calculated along the same paths in the projected Brillouin zone as for the conduction band. The valence band-surface is obtained by linearly interpolating between these points. To get an impression of the spin vector field, the spin vector of each sampled $\vec{k}$-point along the chosen paths is plotted onto the band-surface. This results in figure 6.8.

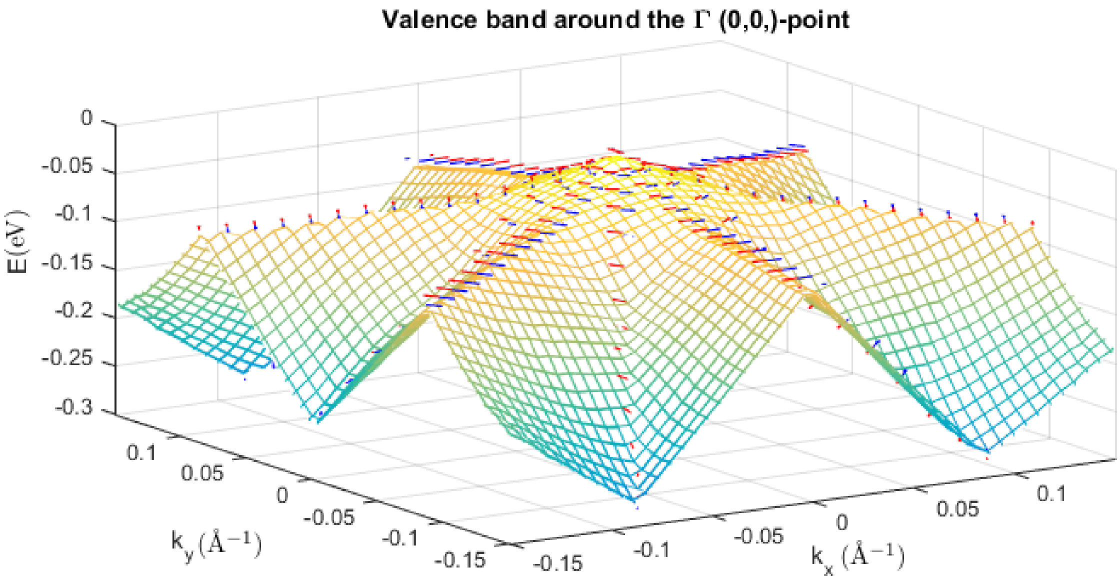

Figure 6.8: Surface valence band-surface that is obtained by linear interpolation between the calculated energies of each of the sampled $\vec{k}$-points. Onto the surface the spin vector field is visible.

This figure immediately shows that the valence band is spin degenerate and each degenerate eigenstate exhibits its own Rashba spin texture. To make this more visible the three-dimensional representation is projected along the $E(k)$ axis. Due to the fact that the spin vectors have zero z-components in the region of interest, no information is lost. The result is shown in figure 6.9.

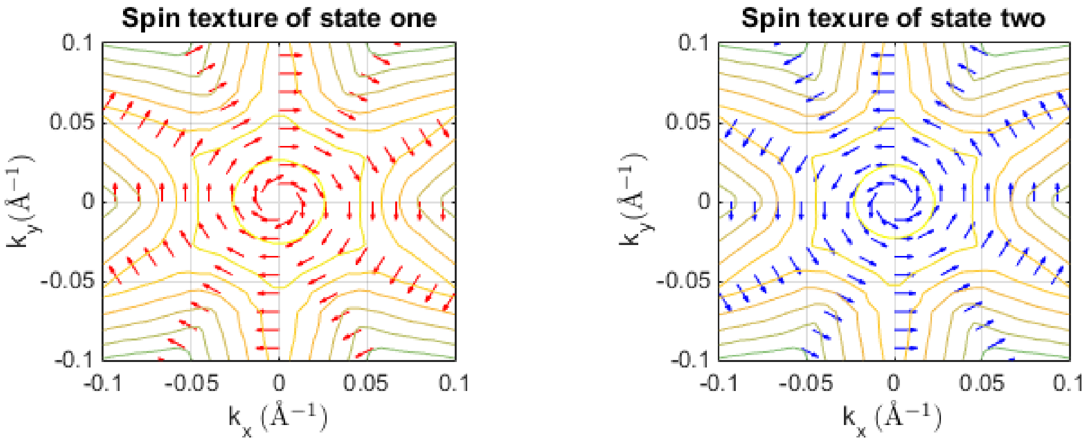

Figure 6.9: Projected band-surface and spin vector field for each degenerate eigenstate separately. These show clear Rashba spin textures with opposite sign.

As expected, clear Rashba spin texture is visible for both eigenstates but as mentioned before this could be a coincidence by a clever choice of linear combination of degenerate eigenstates. To verify that the states exhibiting these spin textures are effectively localized, the contribution of each atomic layer to both of the eigenstates is calculated and plotted in figure 6.10.

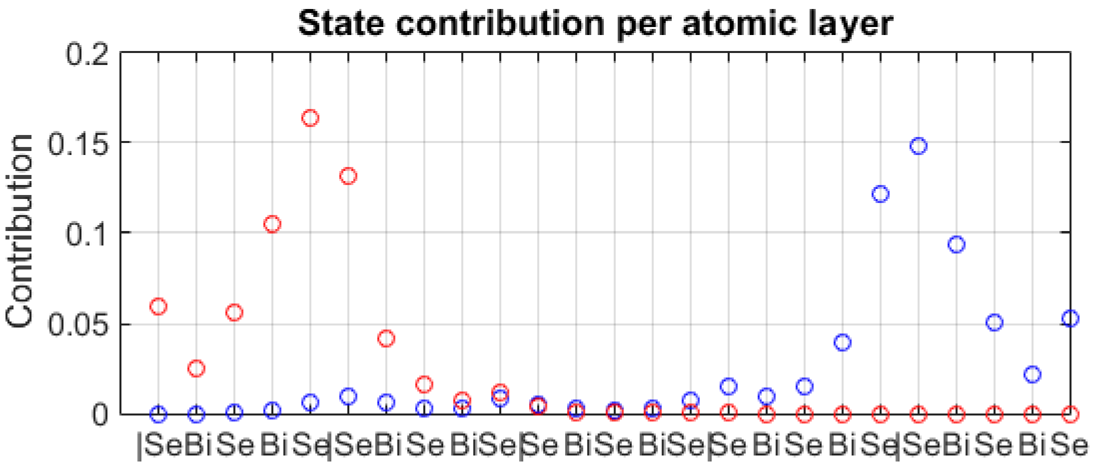

Figure 6.10: A plot representing the contribution of each atomic layer in the slab system to both of the eigenstates that exhibit the compensating Rashba spin texture.

Figure 6.10 shows that the eigenstates under consideration are indeed strongly localized on the surface QLs of the slab system. It needs to be noted that given these contribution, no linear combination of eigenstates can be found where the resulted states are not localized. This contribution of atomic layers to the eigenstates is again not what is predicted by the bulk model and seen in the chapter about the bulk system. Here, entire QLs seem to have spin polarization and the middle QL does not show any contribution the the spin at all.

This localization of both eigenstates on the surfaces of the material, together with the absence of a band gap indicates the presence of topologically protected surface states in the Bi_2Se_3 slab system.

6.1.5 Spin textures of the surface valence state

To get more insight in the spin textures of the slab system, and to see whether mutual spin cancellation takes place, the local spin textures are again calculated on two different scales. The first one is at atomic layer scale. In the bulk system this is the scale where mutual cancellation of the spin polarization takes place. Here however, this will not be the case since from figure 6.10 it is clear that one entire QL has a net spin polarization.

The local spin polarization of each atomic layer in the lower, surface QL is plotted in figure 6.11.

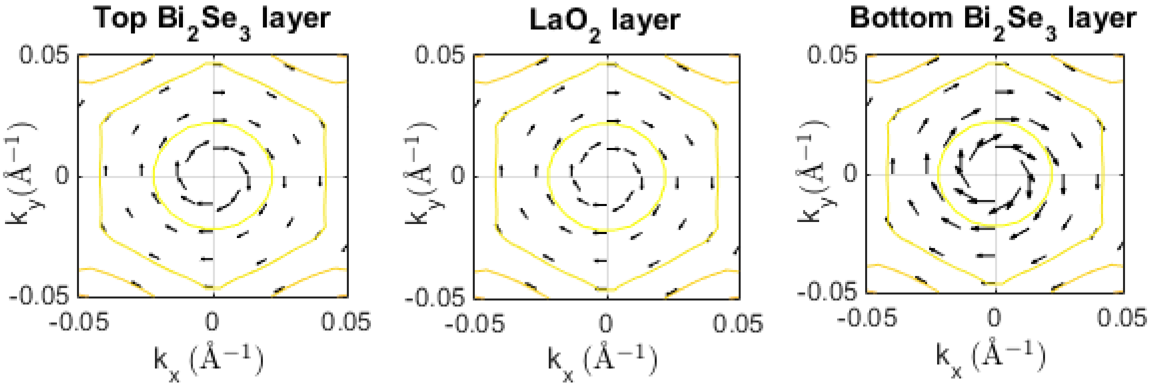

Figure 6.11: Local spin textures per inversion sector of one of the surface QLs obtained by summing over the spin expectation values of both degenerate states corresponding to the the valence band.

These results confirm that the spin textures in the slab system are distinct from the ones in the bulk system. Here, the atomic layers do not have opposite sign and consequently do not mutually cancel, leading to a net spin polarization over the entire QL.

The second scale at which the local spin texture will be calculated is for the different QLs that build up the entire slab system. The results are depicted in figure 6.12.

It is clear that on this scale, spin textures do in fact mutually compensate each other when summed over the entire slab system. This leads to the absence of spin polarization of the entire slab system, visible in the bottom right panel of figure 6.12. The mutually cancelling of spin textures however, takes place on a different scale than for the bulk system. Here, entire QLs exhibit net spin polarization. Consequently in the slab system, the QLs as a whole make sure the total spin of the system vanishes, as it should for centrosymmetric systems.

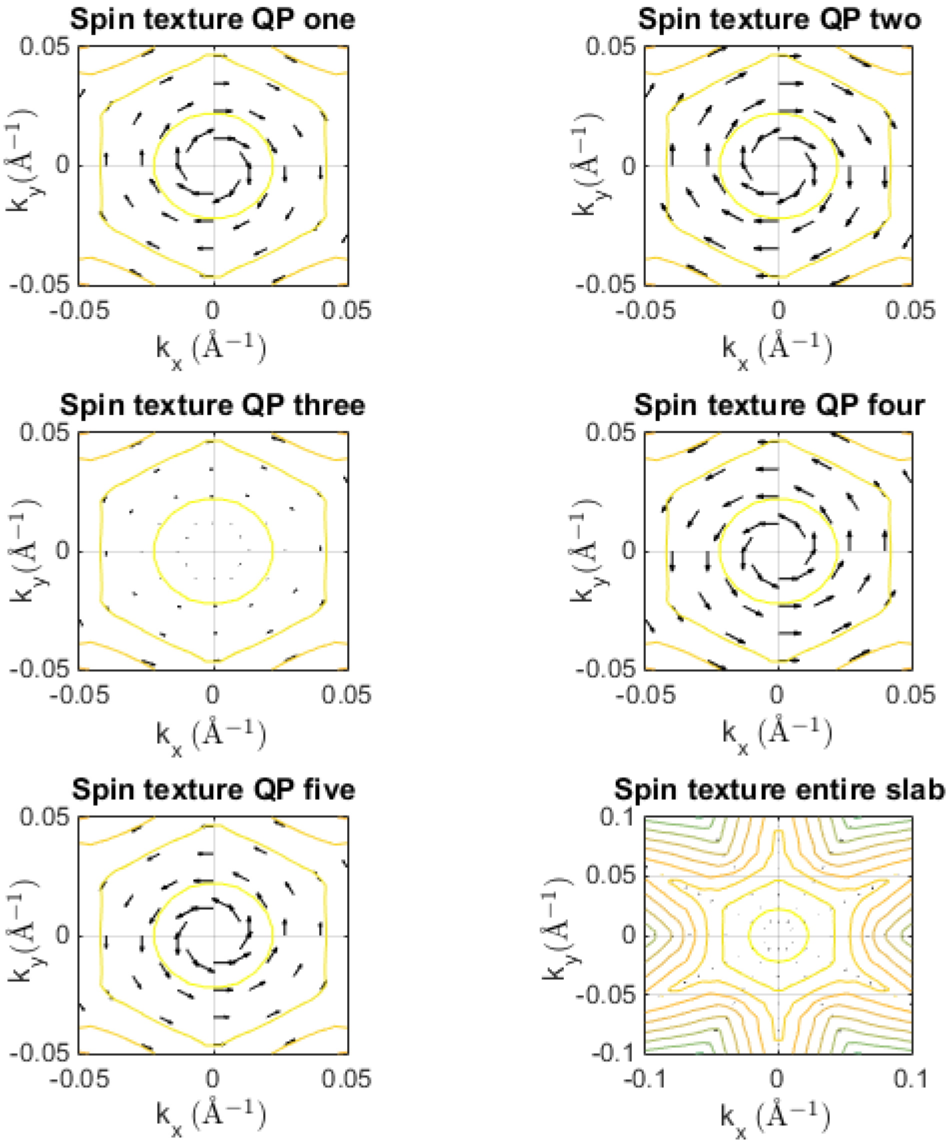

Figure 6.12: Net spin textures of the five QLs (from bottom to top) constituting the entire slab system obtained by summing the spin expectation values of both degenerate states corresponding to this specific band and localized on each QL. The bottom right panel shows the net spin texture for this band, summed over the entire slab system.

6.1.6 Discussion on the Bi_2Se_3 surface states

The results from the DFT calculations on the slab Bi_2Se_3 system are in agreement with the characteristics of topological insulation. The presence of band-closing conducting states which are localized on the outer QLs of the system is retrieved. The spin textures per layer also show strong spin-momentum locking on each of the two surfaces, with opposite sign.

As was already briefly mentioned, the R-2 bulk spin texture that was obtained for the bulk system has vanished. For the slab system, entire QLs exhibit spin polarization, something that was not the case for the bulk system where BiSe sectors *within* one QL exhibit mutually cancelling spin. Also note for later in debt discussion that for both the valence and conduction surface band, the spin texture of the top QL has the same sign as the spin texture of the top sector in the bulk system (figures 5.8-5.10) and the spin texture sign of the bottom QL corresponds to the spin texture of the bottom sector in the bulk system (figures 5.13-5.15). This correspondence will turn out to be crucial to understand the spin textures of slab systems.

It can be concluded that these topologically protected surface states do not exhibit hidden spin polarization since they are spin polarized states that are localized on the surface of the system. Following this reasoning, it is expected that bands of the slab system that belong to *bulk* states, should exhibit the bulk spin textures as obtained in the previous chapter and thus the R-2 effect must be seen. This claim will be investigated in the next section.

6.2 Bulk states in the slab system

In this section the bands above the surface conduction band and below the surface valence band will be analysed. It can be argued that these bands correspond to the bulk electronic states due to their shape characteristics and the fact that for each QL that is added to the slab system, one extra band appears. The latter is best seen for the conduction and valence bands in figure 6.1.

It can also be seen directly by looking at the distribution which shows how much each atomic layer contributes to the specific state. The band that will be analysed here is the first conduction band above the topological surface state, which will be called the bulk conduction band. The contribution distribution of this band is depicted in figure 6.13 and shows a clear bulk character.

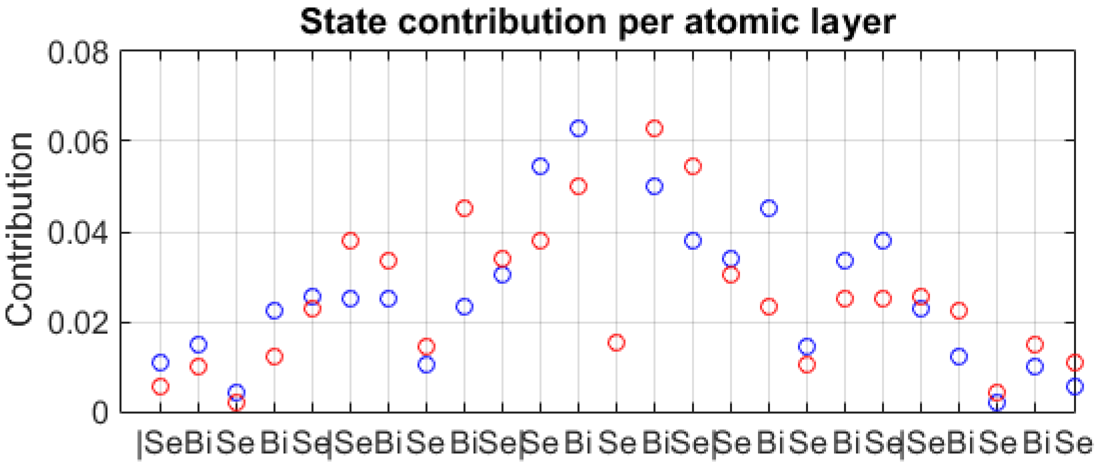

Figure 6.13: Contribution distribution of the bulk conduction band of the Bi_2Se_3 slab system.

Since this shows that the states are mainly localized on the bulk QLs, it is expected that the bulk spin texture will be retrieved and consequently a hidden spin polarization within the QLs will be present.

To get an understanding in the local spin texture of these bulk states in the slab system, the same analysis as before is performed. This means, projecting the spin expectation values of the degenerate states onto each atomic layer. Afterwards, the spin expectation values of both states can be added for each specific atomic layer to see if the layers exhibit any net spin textures. First the spin texture of entire QLs is visualized to see whether they exhibit a net spin polarization or not. The results are given in figure 6.14.

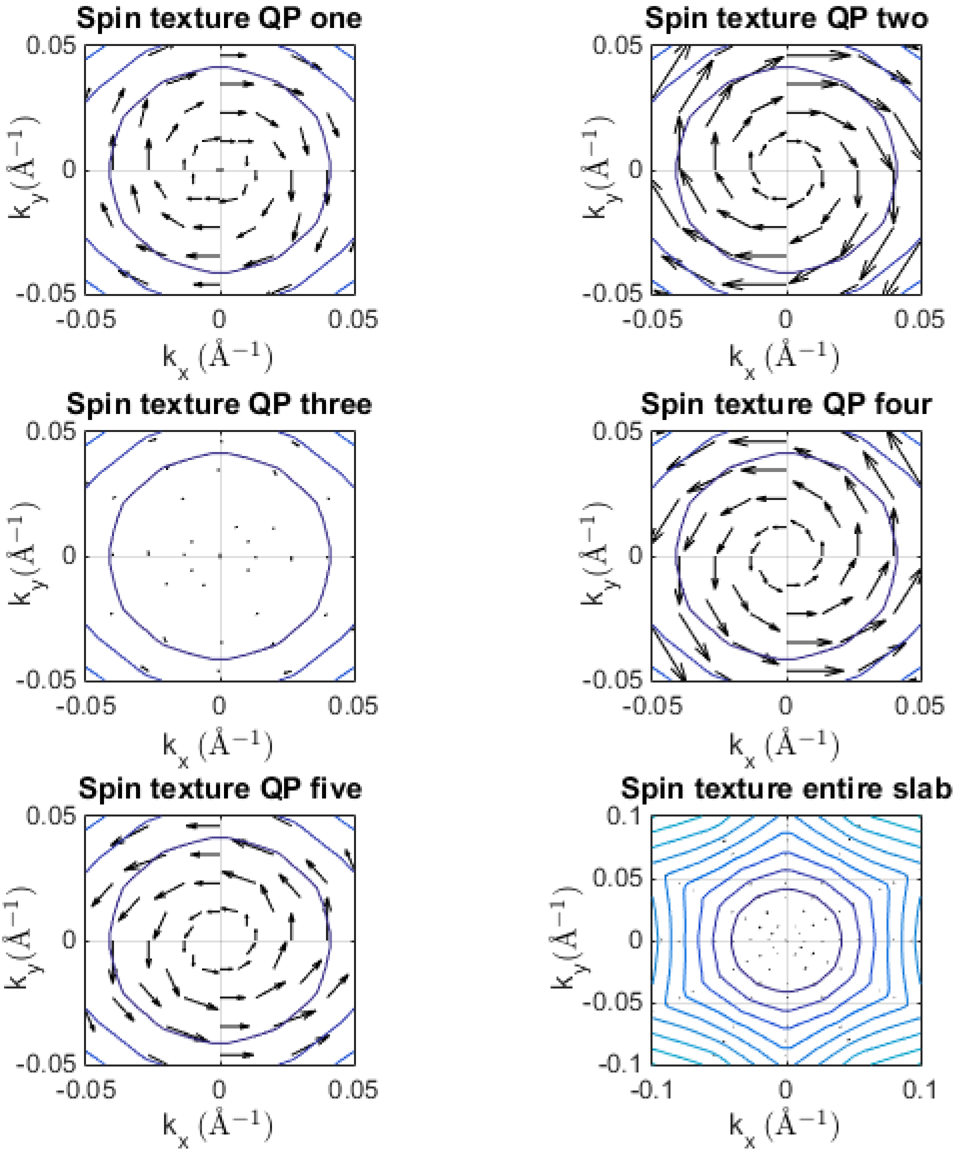

Figure 6.14: Net spin textures of the five QLs (from bottom to top) constituting the entire slab system obtained by summing the spin expectation values of both degenerate states corresponding to this specific band and localized on each QL. The bottom right panel shows the net spin texture for this band, summed over the entire slab system.

This is a surprising result which shows that also for the bulk states, entire QLs show spin polarization. This means that the symmetry within the QLs is broken and that the R-2 effect that is present in the bulk system, has vanished.

However, the next figure, 6.15, shows the local spin texture of the atomic sectors constituting the middle QL . This QL has negligible spin polarization as a whole, and internal spin compensation could still be possible.

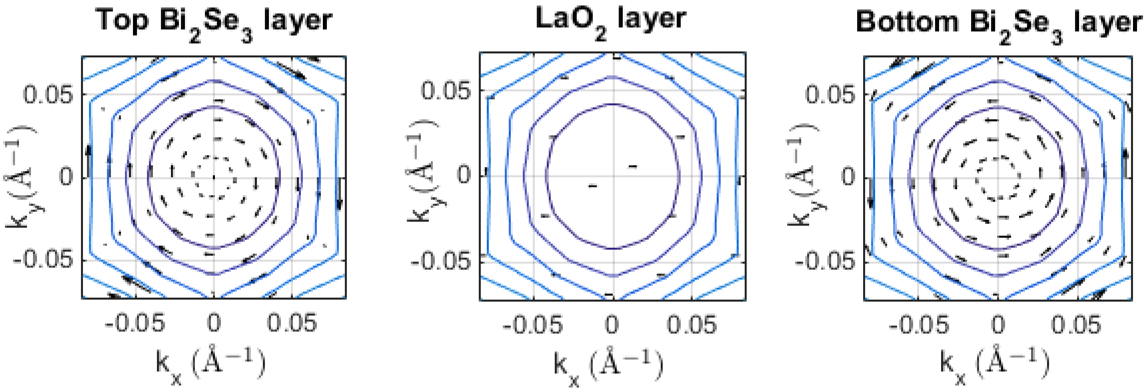

Figure 6.15: Spin textures localized on each inversion sector within the third (middle) QL in the slab system.

The spin textures are very small, but they do show opposite in sign Rashba behaviour, localized on inversion partners. It seems that this middle QL does show hidden spin polarization in the form of the R-2 effect and that the spin textures are of the same sign as in the bulk system. The results show that even for the bulk states, the R-2 within the QLs vanishes except for the middle QL in the slab system. Possible explanations will be given at the end of this section, after the same analysis is done for the bulk valence band.

To check whether the bulk valence band also corresponds to a bulk state, the contribution distribution is calculated and results in figure 6.16.

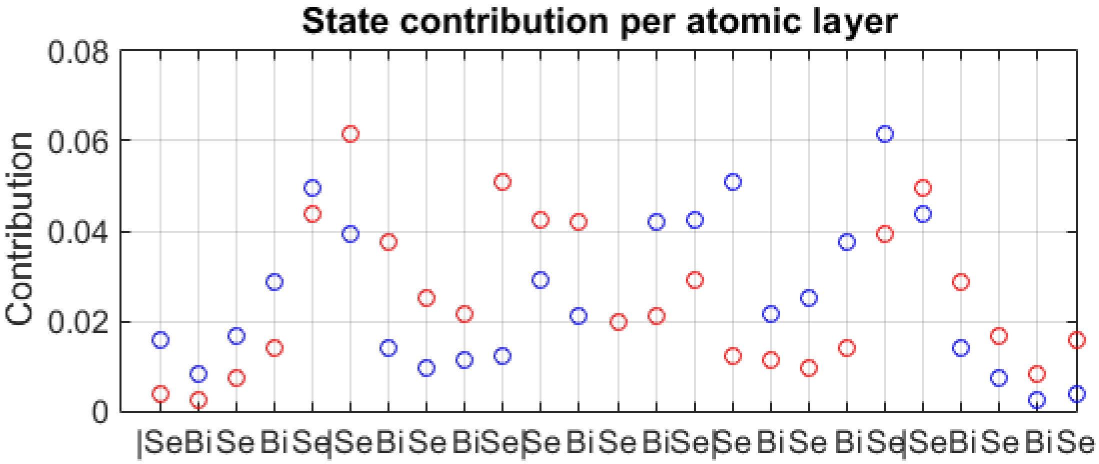

Figure 6.16: Contribution distribution of the bulk valence band of the Bi$_2$Se$_3$ slab system.

The result shows that these degenerate states are mainly localized on the bulk slabs. As before, the expectation is that since they belong to bulk slabs, the bulk spin textures of the previous chapter are present in the form of the hidden spin polarization for each QL. However, this turns out not to be the case as can be clearly seen when the spin texture for each QL is plotted in figure 6.17.

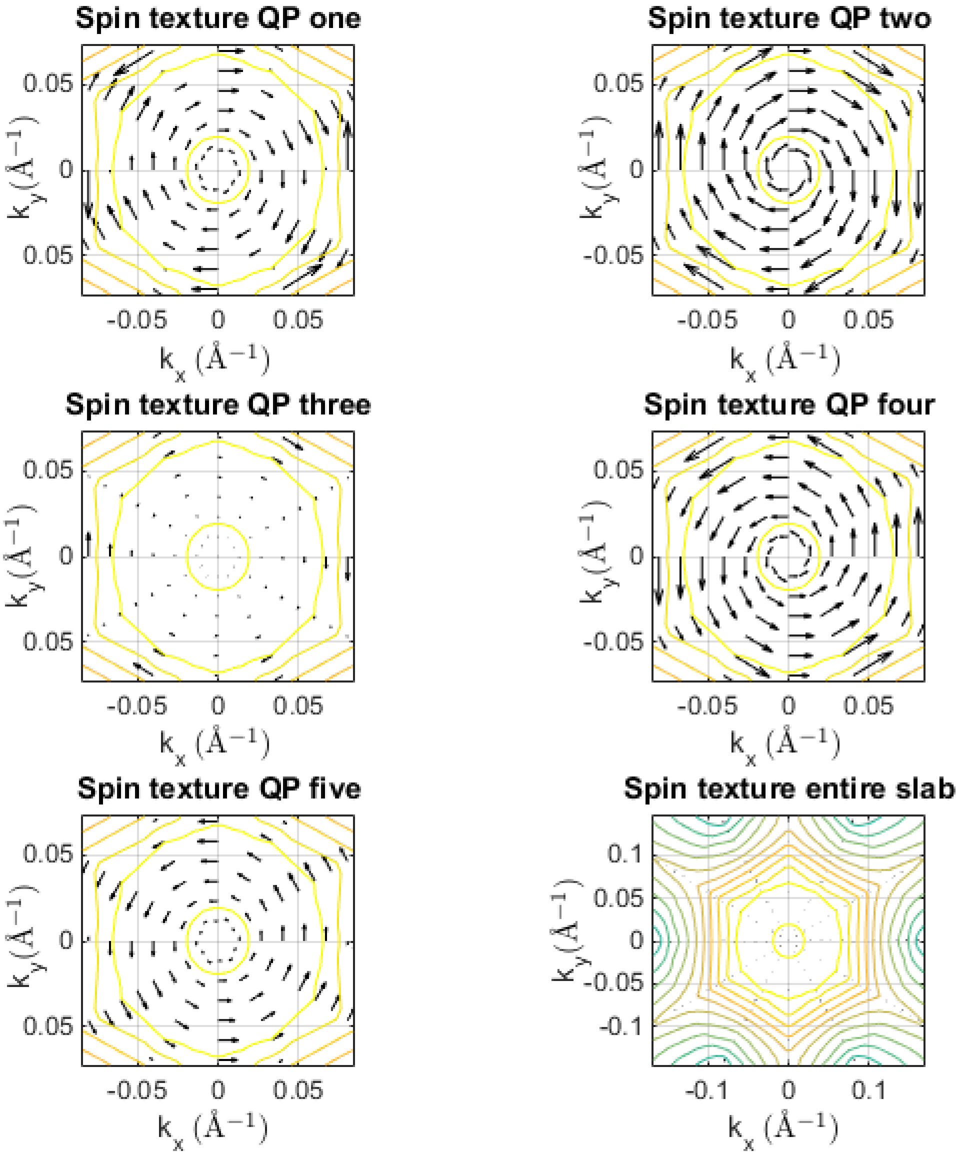

Figure 6.17: Net spin textures of the five QLs (from bottom to top) constituting the entire slab system obtained by summing the spin expectation values of both degenerate states corresponding to this specific band and localized on each QL. The bottom right panel shows the net spin texture for this band, summed over the entire slab system.

These plots show that also for the bulk-valence band, entire QLs show net spin polarization, which is not in line with the R-2 effect as described for the bulk system. Only the middle QL shows negligible spin, meaning that for this layer, internal spin cancellation can still be present. The spin textures of each sector in this QL is plotted in figure 6.18.

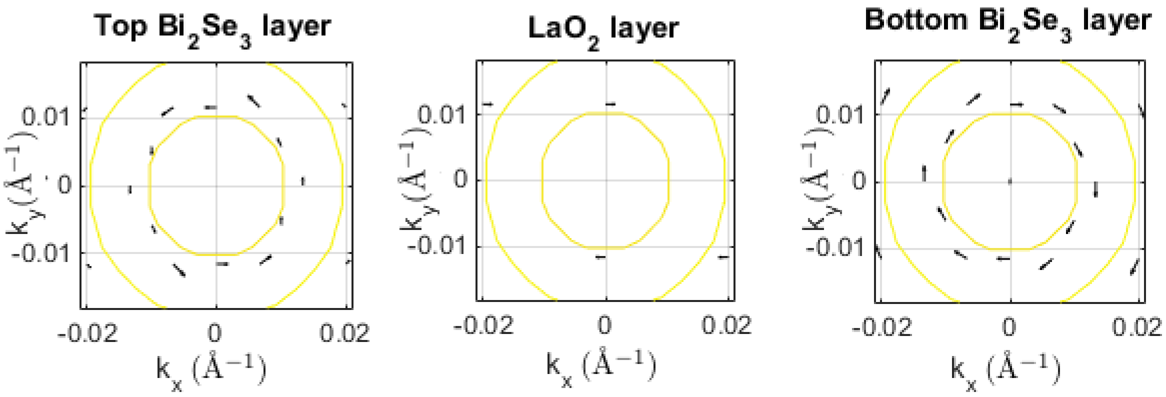

Figure 6.18: Spin textures localized on each inversion sector within the third (middle) QL in the slab system.

For the bulk valence band, the spin texture of each sector in the middle QL is very small. However, the Rashba spin textures on opposing layers of the inversion partners are opposite in sign and cancel each other out. This means that the R-2 effect is present in this QL, albeit very small.

6.2.1 Discussion of the results of the Bi_2Se_3 slab system

The DFT calculations on the Bi_2Se_3 slab system clearly show the topological nature of the surface states. These states close the bulk band gap and are strongly localized on the surface QLs of the material. The spin polarization of entire QLs is in contrast with the bulk system, where each QL had a zero net spin polarization. It has also been shown that these surface states have opposite in sign, Rashba spin textures. This leads to the coupling of the motion and spin of the conducting electrons which is referred to as spin-momentum locking.

Further analysis reveals that also the bulk states of the slab system show a net spin polarization of entire QLs. Consequently, hidden spin polarization within these QLs cannot be present, as was the case in the bulk system. Only the middle QL shows no net spin polarization and it turns out that this specific QL does show mutually cancelling, local spin textures, a clear R-2 signature.

This behaviour, and especially the vanishing of the R-2 effect in the bulk states, is in strong contrast with the obtained results for the bulk system. The discrepancy can be attributed to the fact that Bi_2Se_3 is a topological insulator and is expected to have spin polarized surface states. It could be so that the topological character of the system exhibits its effects on bulk states. This would need a deeper understanding in the concept of topological insulation.

Another explanation could be that the mere presence of a surface in a system influences the electronic properties of atomic layers that are in the vicinity of the surface. For instance, the presence of a surface could lead to a charge redistribution in the outer layers of the crystal, resulting in an additional electric field. This electric field breaks the symmetry within the surface slabs and destroys the mutually cancelling spin textures, leading to a vanishing of the R-2 effect.

To test whether it is indeed the presence of a surface that leads to the vanishing of the hidden spin polarization or if it is only a property of topological insulation, two slab systems that do not exhibit topological surface states will be analysed in the same manner as before. The first system is strained Bi_2Se_3 of which it is shown that it loses its topological character[27]. The second system will be a slab of $LaOBiS_2$ because those results can be readily compared to the bulk analysis of this material in chapter four.

6.3 Non-topological slab systems

As mentioned, this section will entail the study of two non-topological slab systems in order to check whether the surface effects on the bulk hidden spin polarization in Bi_2Se_3, studied in the previous section, are only due to its topological character, or if it is a general phenomenon that is attributed to the presence of a surface.

6.3.1 Strained Bi_2Se_3 system

The first non-topological slab system that will be investigated is Bi_2Se_3, strained along the z-direction. Recently, it was shown that Bi_2Se_3 loses its topological non-trivial character if the material undergoes strain in the uniaxial z-direction[27]. Consequently, by comparing the surface effects on the the spin texture in the strained Bi_2Se_3 slab system with the unstrained (topological) system, information about the influence of the topological character can be gained.

The paper states that the topological phase of Bi_2Se_3 vanishes around the point where the c-parameter, along the z-direction, increases above 30.3 Å. To model the strained system, the c-parameter is put at 31.5Å and the atoms within the new unit cell are relaxed through self-consistent calculations. The resulting crystal structure is then used in further first-principles analysis, analogous to those of previous sections.

6.3.2 Analysis of the bulk system

Before the spin textures of the slab system are studied, it is checked whether the strained Bi_2Se_3 system indeed loses its topological insulating character. To do this, the band structure along the K-Γ-M path is calculated and plotted in figure 6.19. As mentioned in section (2.5), a typical character for topological insulation is the presence of band inversion around a time-reversal point. In the unstrained Bi_2Se_3 this could be seen in figure 5.3, around the Γ-point. Thus, this is a good indicator on whether the system exhibits topological characteristics.

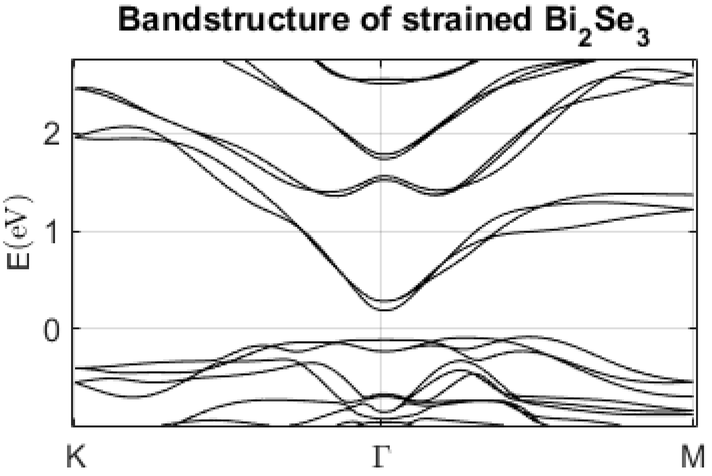

Figure 6.19: Band structure along the K-Γ-M path of the strained Bi_2Se_3 bulk system, where the c-parameter has been increased to 31.5 Å, which results in the vanishing of the topological character.

The band structure shows that the curvature of the top of the valence band is zero such that indeed the band inversion is not present any more. This indicates that for this choice of c-parameter value, the topological character is gone and the system is considered as topologically trivial. Consequently it is expected that the slab system will not show a Dirac cone with corresponding topological surface states. This non-topological slab system is studied in the next section.

6.3.3 Analysis of the slab system

First the bandstructure is calculated along the K-Γ-M path in reciprocal space, see figure 5.1, to see whether indeed the Dirac cone has vanished meaning that the system has no topologically protected surface states. The bandstructure is shown in figure 6.20.

The bandstructure exhibits a bandgap at the Γ-point and no Dirac cone is present. Also, when compared to the bandstructure of the unstrained topological Bi_2Se_3 (figure 6.1), the band inversion of the valence band has vanished. Consequently it is concluded that the strained Bi_2Se_3 system does not have topologically protected surface states. This is what is needed to check whether the spin polarized surface states found in the previous section are due to the topological character of Bi_2Se_3, or just a consequence of the presence of a surface in centrosymmetric R-2/D-2 materials. The spin textures of the conduction and valence band, and their localization are treated next.

6.3.4 Bulk conduction state

In order to study the spin textures the same analysis as before is done. The energy along different paths that cross the Γ-point (see figure 5.1) are calculated to obtain a contour plot of the energy surface. Onto this contour plot, the spin texture is visualized as a two-dimensional vector on each sampled $\vec{k}$-point, for one specific, degenerate eigenenergy. The localization of the different spin textures within the slab system is obtained by projecting the eigenstate onto different atomic layers.

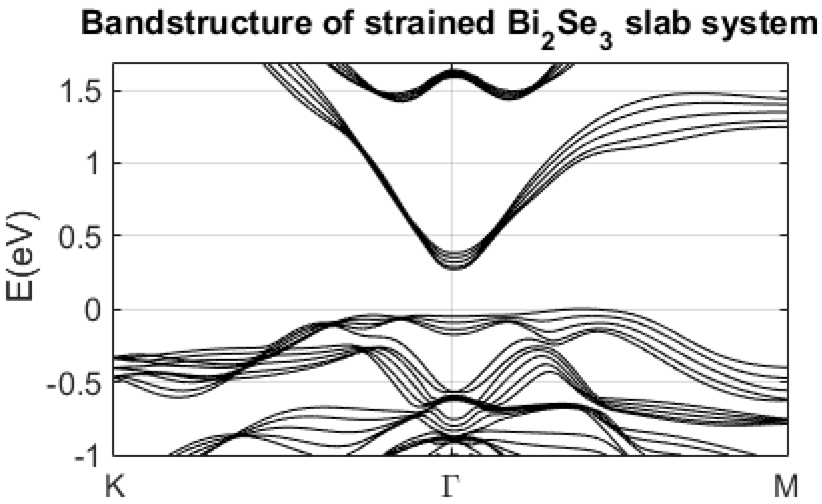

Figure 6.20: Band structure along the K-Γ-M path of the strained Bi_2Se_3 five QL slab system, where the c-parameter has been increased to 31.5 Å, which results in the vanishing of the topological edge states.

First the density distribution of the degenerate eigenstates corresponding to the conduction band is plotted along the stacking direction of the crystal, figure 6.21.

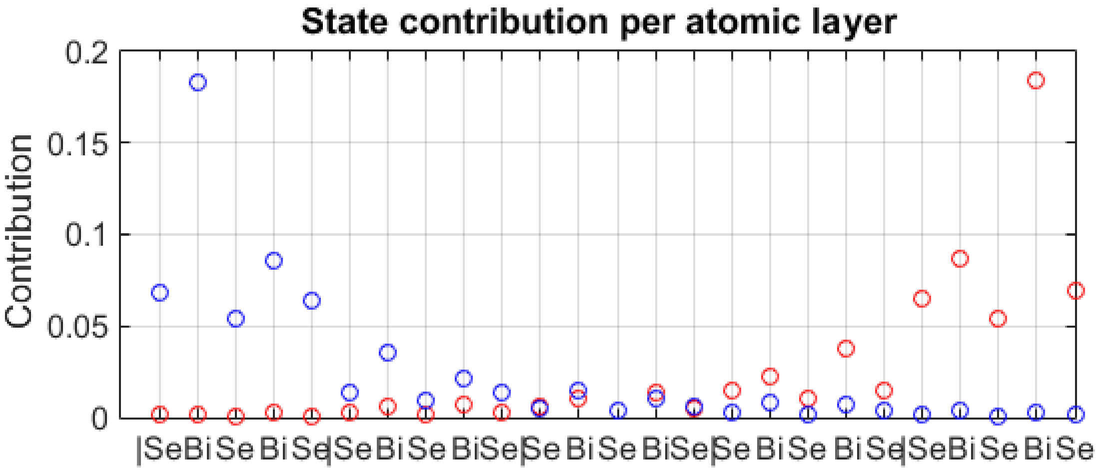

Figure 6.21: State density distribution of both degenerate states along the z-direction of the strained Bi_2Se_3 conduction band.

This figure shows that even though the topological character of the system has vanished and no Dirac cone is present, the conduction state is still mainly localized on the surface of the slab system. It is clear that, compared to the bulk system, the symmetry of the state distribution within each QL is broken. To see the effect of the surface on the hidden spin polarization of the bulk system, the spin texture localized on each QL is plotted in figure 6.22.

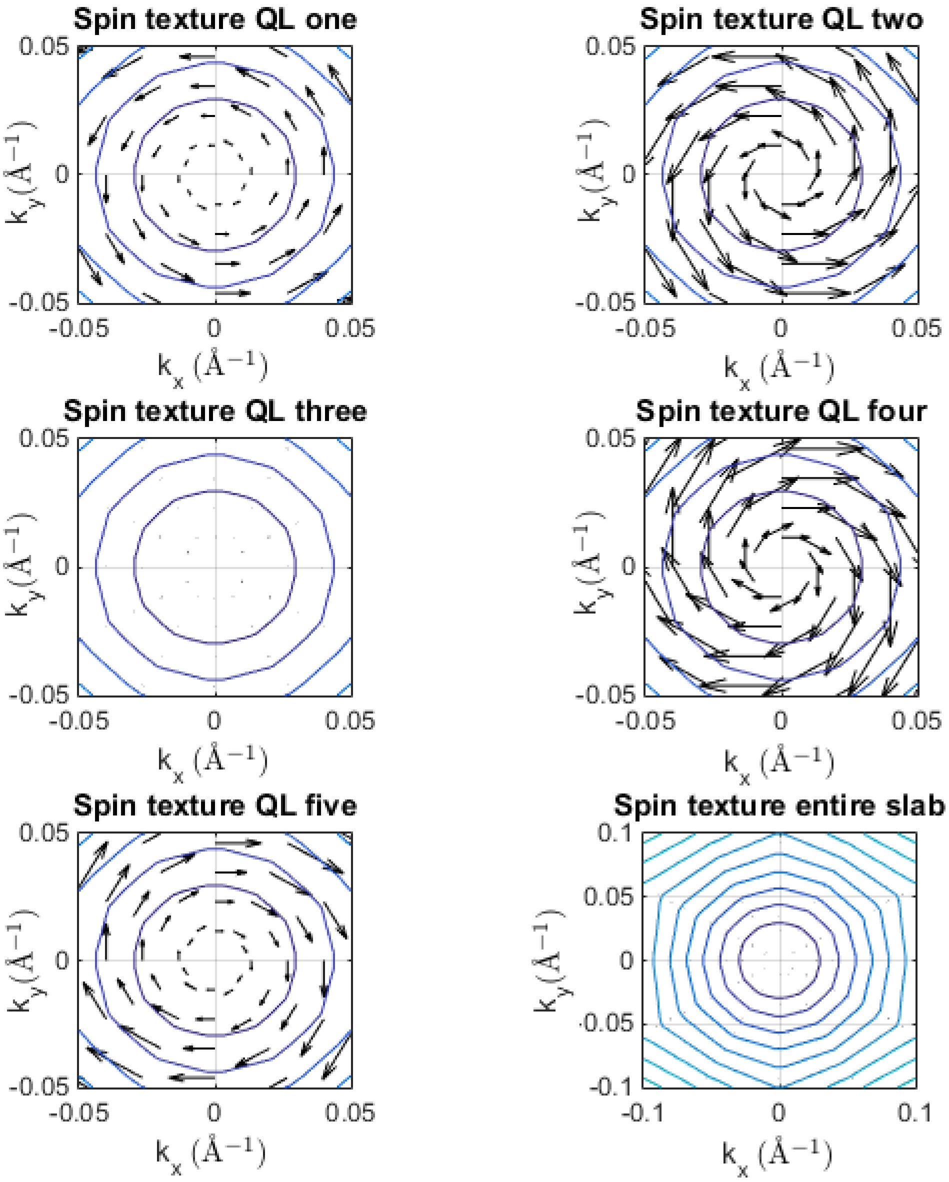

Figure 6.22: Net spin textures of the five QLs (from bottom to top) constituting the entire slab system obtained by summing the spin expectation values of both degenerate states corresponding to the conduction band and localized on each QL. The bottom right panel shows the net spin texture for this band, summed over the entire slab system.

It is immediately clear that entire QLs are spin polarized and that the hidden spin polarization in the form of the R-2 effect has vanished. So the same net spin polarization that was visible for the non-strained topological Bi_2Se_3 system is present here. This indicates that the polarized surface states cannot be attributed to the topological character of a material but rather to the presence of a surface.

The same analysis is done for the valence band of the strained slab system. The results are visualized in the same manner and similar results for the spin texture are obtained.

6.3.5 Bulk valence state

To get a first insight of where the valence state is localized, its state density distribution is plotted along the stacking (z)-direction of the crystal. The result is shown in figure 6.23.

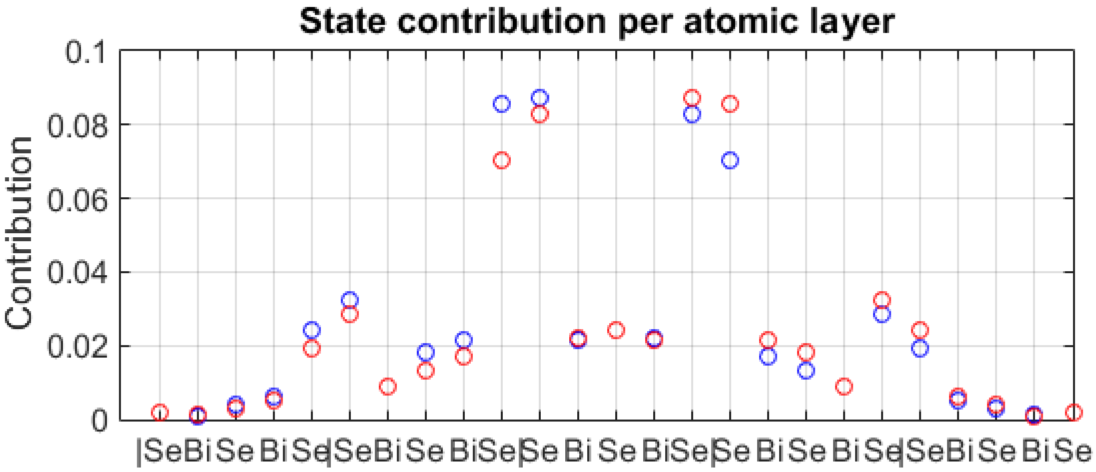

Figure 6.23: State density distribution of both degenerate states along the z-direction of the strained Bi_2Se_3 valence band.

It can be seen that the valence band is mainly localized within the middle QLs of the system, which is in contrast to obtained distribution for the conduction band. However, the symmetry of the density distribution within single QLs is nonetheless broken compared to the bulk system. Again, this indicates a vanishing of the R-2 effect and with it the hidden spin polarization. However, caution is needed since this specific density distribution could be a linear combination of other eigenstates. To verify the symmetry breaking, the spin textures on the different QLs is explicitly calculated.

The valence band spin textures localized on each QL are plotted in figure 6.24 together with the spin polarization of the entire slab system. Similar spin textures as for the conduction band are retrieved. It is clear that entire QLs have a net spin polarization instead of mutually cancelling spins within one QL. So without the presence of topological surface states, a net spin polarization at the surface of the slab system is still observed.

6.3.6 Conclusion on strained Bi_2Se_3 system

First-principles studies on strained Bi_2Se_3 show that by putting strain on the crystal, elongating its c-parameter, the Dirac cone vanishes and its topological character is lost. Nevertheless, by introducing surfaces in the system, the R-2 effect of hidden spin polarization vanishes and entire QLs that in the bulk system showed no net spin polarization now show clear Rashba spin textures. These results suggest that the net spin polarization of the surface QLs cannot be attributed to the topological character of the system, but instead to the mere presence of the surface. The mechanism behind this is explained at the end of the chapter.

In the next section the $LaOBiS_2$ slab system is studied. This crystal is another non-topological system and can be compared to its bulk analysis in previous chapters.

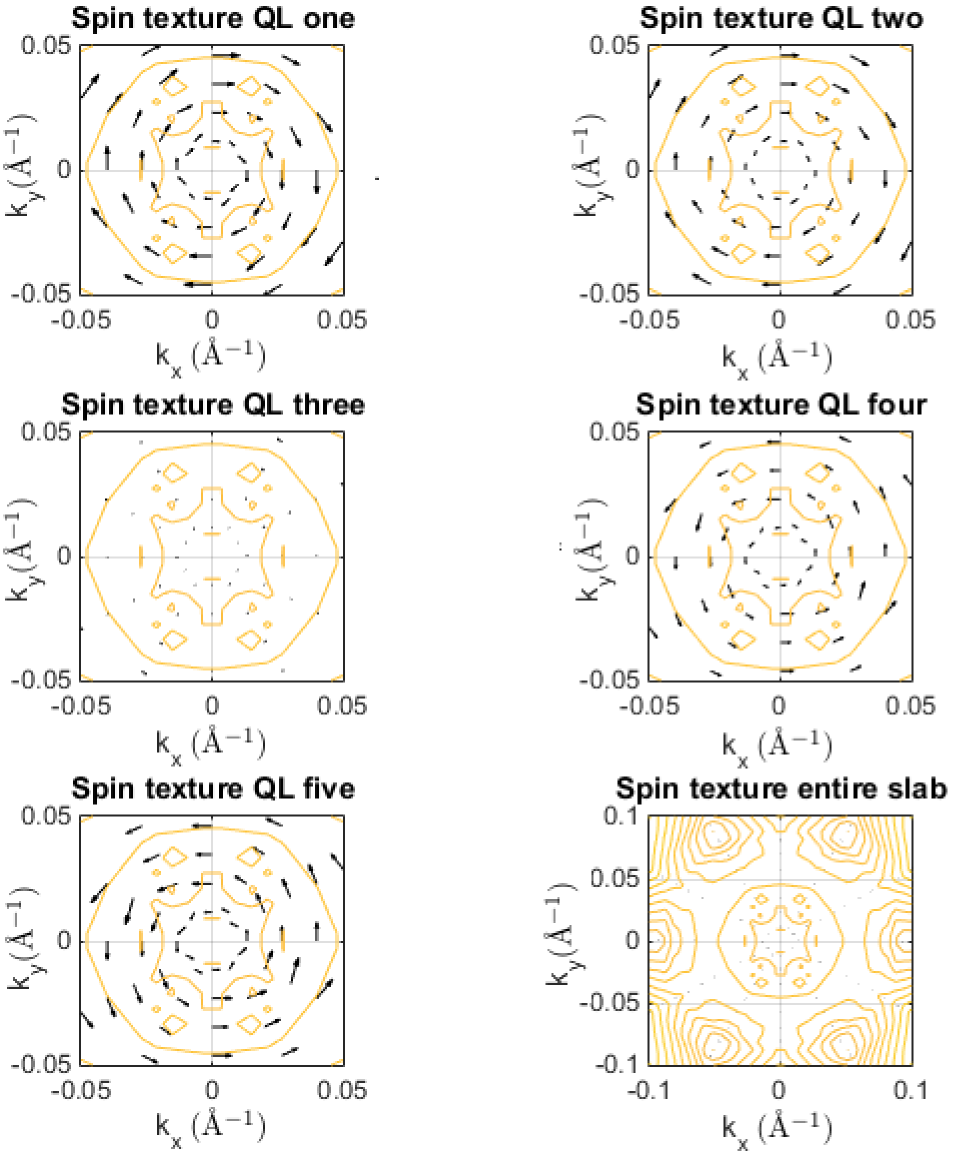
Spin texture QL one

Spin texture QL two

Spin texture QL three

Spin texture QL four

Spin texture QL five

Spin texture entire slab

Figure 6.24: Net spin textures of the five QLs (from bottom to top) constituting the entire slab system obtained by summing the spin expectation values of both degenerate states corresponding to the valence band and localized on each QL. The bottom right panel shows the net spin texture for this band, summed over the entire slab system. Because the top of the valence band is very flat, small fluctuations can be seen the the contour plots.

6.4 LaOBiS$_2$ Slab system

Now that it is clear that it is the presence of the surface that leads to the vanishing of the hidden spin polarization and induces net spin polarization, a second non-topological slab system is studied to investigate a possible explanation of this surface effect. Bulk LaOBiS$_2$ has been extensively analysed in chapter 4 and therefore it convenient to study the slab system of this compound in order to make a detailed comparison between the spin textures of the bulk and slab system.

Since the LaOBiS$_2$ crystal is not built up of QLs, the terminology needs to be adapted. The slab system consists of a finite number of units in which each unit consists of ten atomic layers. Such a unit represents in fact the same unit as the QL does in Bi$_2$Se$_3$.

These units can be divided into two inversion partner sectors and one middle LaO$_2$ layer, as depicted in chapter three of this thesis, figure 3.2.

The specific system being analysed here consists of three ten-layer units of which the two outer ones are considered the surface units. Since LaOBiS$_2$ is not a topological insulator, conducting surface states are not present. Consequently is suffices to study the conduction and valence band of this slab system.

6.4.1 Conduction state

The first band that will be looked at the is the conduction band. The same analysis as before can be made and the results are similarly presented. First, the net spin texture of each ten-layer unit is visualized in order to compare it with the spin textures of the bulk system in chapter four. The result is given by figure 6.25.

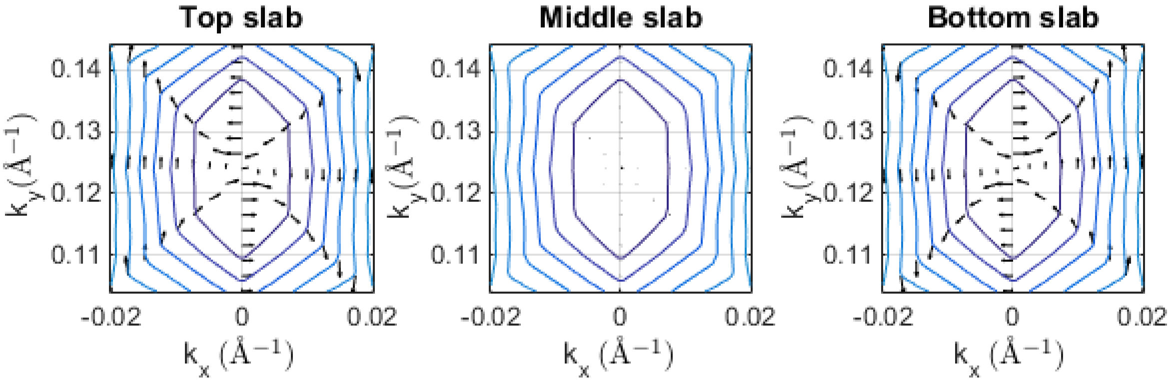

Figure 6.25: Net spin texture localized on each of the three units, obtained by summing the spin expectation values of both the corresponding degenerate states of the lower conduction band.

The state density distribution is also plotted to check where the conduction state is mainly localized inside the slab system which will be needed for later discussion, figure 6.26.

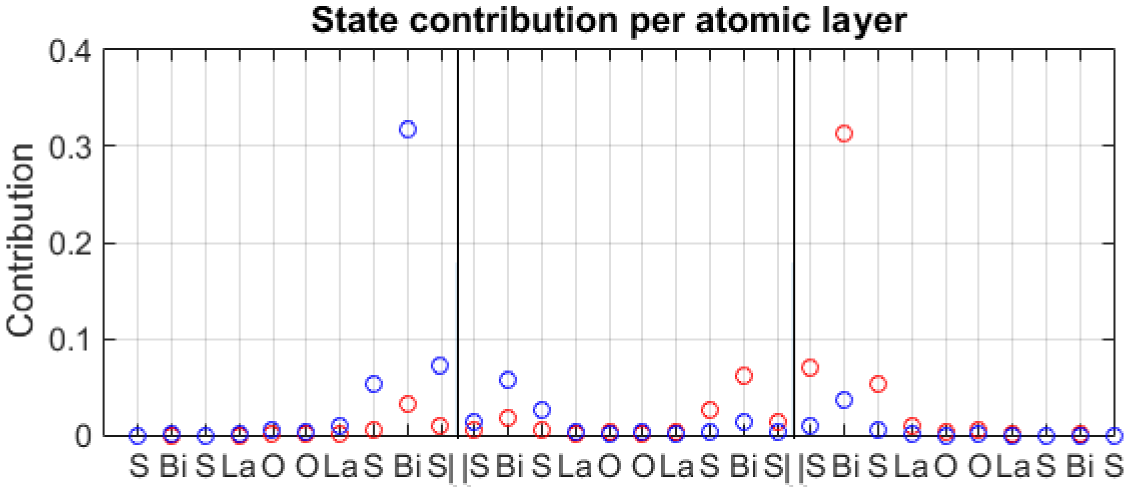

Figure 6.26: State density distribution of the states that constitute the conduction band.

Figure 6.25 shows that the also for the LaOBiS$_2$ slab system, entire units are spin polarized and exhibit clear Dresselhaus spin texture. Again, this is in contrast with the bulk system, where each unit on its own has no spin polarization due to the mutually cancelling of the spin textures within the unit, described as the D-2 effect. From figure 6.26 it can be seen that the probability distribution of the conduction state is not symmetrically within one unit. Both degenerate eigenstates, with their own spin texture, are localized on different sides of the slab system. However over the entire slab system, it is symmetrically distributed, which is necessary to satisfy the demand that centrosymmetric systems cannot exhibit a net spin polarization.

As was the case for the previous slab systems, figure 6.26 shows that the middle unit has a symmetric density distribution, consequently the middle unit exhibits no net spin polarization and thus is expected to, on its own, have hidden spin polarization as described by the bulk system. Figure 6.27 shows the spin texture of each atomic sector within this middle unit.

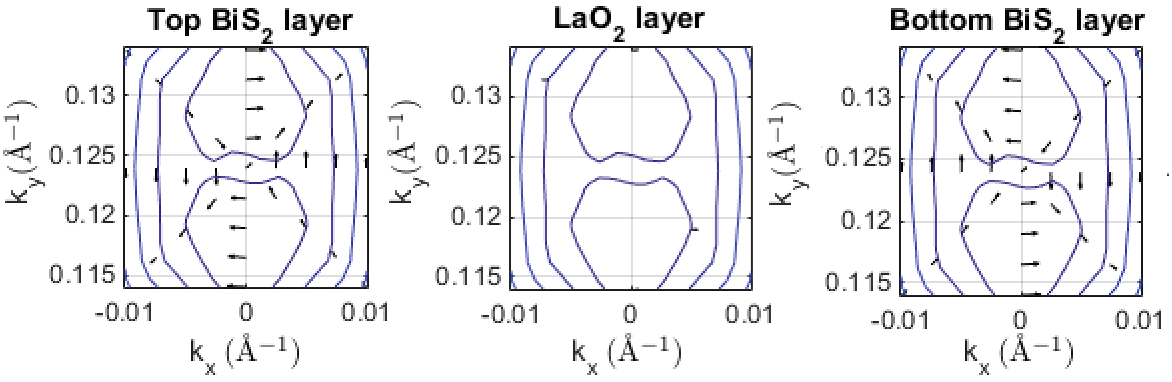

Figure 6.27: Net spin texture of the lower conduction band localized on the inversions sectors within the middle unit.

It is clear that this unit does indeed show hidden spin polarization in the form of the D-2 effect with the same sign as obtained for the bulk system. However, the magnitude of the spin expectation values are very small, which is apparent by the need to zoom in around the $X = (1/2, 0)$-point.

For later discussion, it needs to be noted that the spin texture of the top *unit* (figure 6.26) has the same sign as the spin texture of the bottom *sector* (figure 6.27). Vice versa, the spin texture of the bottom *unit* has the same sign as the spin texture of the top *sector*. As a reminder, this is different than the Bi_2Se_3 slab system, where the correspondence of spin texture-sign between QL and sector was top-top and bottom-bottom.

6.4.2 Valence State

For the valence band the same analysis is done and similar results are obtained. Note that for the bulk system, only Rashba spin textures are present for the valence band. Figure 6.28 represents the net spin texture for each of the three units.

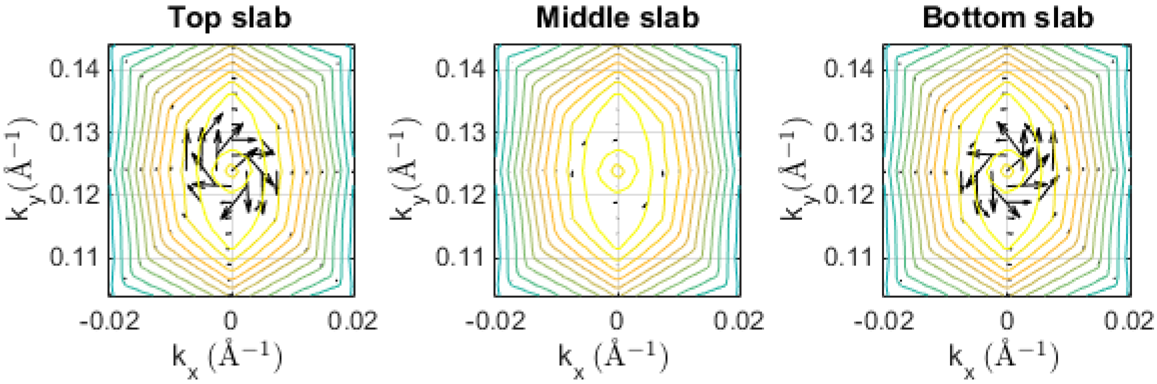

Figure 6.28: Net spin texture localized on each of the three units, obtained by summing the spin expectation values of both the degenerate highest valence band states.

Net spin polarization of entire units is again present together with clear Rashba spin textures. As before, the middle unit shows negligible spin polarization, indicating that mutually cancellation of spin textures within this unit is present.

The corresponding density distribution corresponding to the valence state is depicted in figure 6.29.

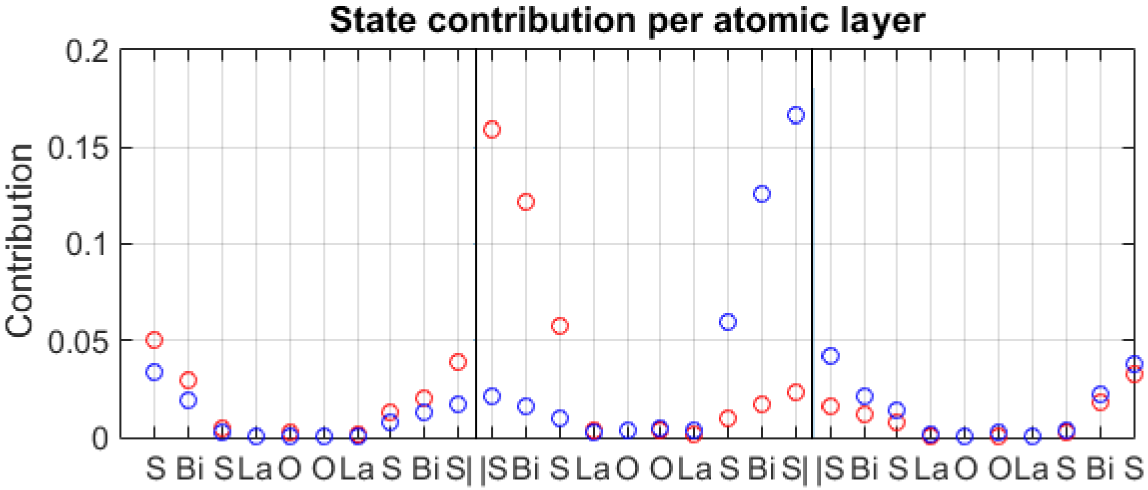

Figure 6.29: Net spin texture localized on the inversions sectors within the middle unit.

The asymmetry of probability density within the outer units is again present. However, compared to the conduction state, figure 6.26, the asymmetry is much less pronounced. Both the degenerate states have much more density localized on the middle slab. Another difference that is worth noting is that the probability density in the outer units, for both states, is higher on the outer atomic sectors.

As mentioned, it can also be seen that the middle unit retains its symmetric probability distribution. This leads to the survival of the local, hidden spin polarization within this unit. This can be verified by plotting explicitly the spin textures per inversion sector within the middle unit, figure 6.30.

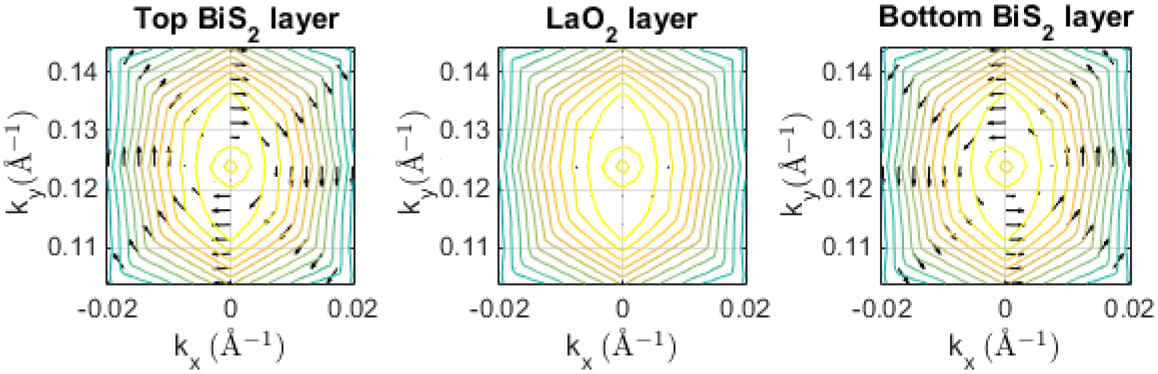

Figure 6.30: Net spin texture localized on the inversions sectors within the middle unit.

This result clearly shows mutually cancelling spin textures localized on the inversion sectors, a clear mark of hidden spin polarization in the form of the R-2 effect. Other than for the conduction band, the magnitude of the spin expectation values are comparable with the ones in the corresponding band for the bulk system. The latter could already be anticipated by looking at the density distribution, figure 6.29, which is mainly localized on the middle unit.

Again, it is important to look at the correspondence of the sign of the spin texture between the slab system and the bulk system. For the valence band, the spin texture-sign of the top *unit*, figure 6.28, corresponds to that of the top *sector*, figure 6.30. The same correspondence holds for the bottom unit and sector.

In the next section, a mechanism is proposed which explains the discrepancy between the spin textures of bulk systems and slab systems.

6.5 Discussion of the slab system results

From the DFT calculations on non-topological slab systems, it became clear that the discrepancies between bulk states in bulk systems and bulk states in slab systems can be attributed to the presence of a surface in the system, rather than the topological character of the material. Then it remains to find a mechanism that explains which spin texture is observed in the slab system compared to the bulk system.

In the slab systems, entire units (QLs) exhibit spin polarization and thus spin texture. Throughout the analysis of the systems in previous sections, the spin texture of the top and bottom unit (QL) was compared to the top and bottom atomic sector of the corresponding bulk system. In some cases, the top/bottom unit (QL) adopts the spin texture of the top/bottom atomic sector, for example the bulk conduction state in the slab Bi_2Se_3 system. In other cases it is the other way around, where the top/bottom unit corresponds with the bottom/top atomic sector. Both of the correspondences can occur within the same material, but for different states, for example the conduction and valence band in the slab $LaOBiS_2$ system.

Two effects will be present when introducing a surface in a bulk system and the resulting spin textures of the slab system will be due to a combination of both. The surface induces a redistribution of the total charge density of the electrons within the units close the the surface, leading to a net change of the electric field within these surface units. This breaks the symmetry and diminishes the possibility of mutually cancelling spin textures. It is important to note that the charge density redistribution is the same for all the energy bands and their corresponding states.

The presence of a surface will, on the other hand, lead to a change in density distribution of each particular state corresponding to different (Kohm-Sham) energy levels due to the fact that periodicity is broken. Consequently, different states can be localized on different atomic sectors, adopting the spin texture of the sector they are localized on.

The influence of both effects on the final spin texture per state will be analysed in the next part of this section.

6.5.1 Charge redistribution

In order to analyse the extend to which the charge redistribution due to the presence of the surface has an influence on the spin textures, two cases will be compared. First the total charge density along the z-axis of the bulk system is calculated and visualized for both the bulk Bi_2Se_3 and bulk $LaOBiS_2$ system. This one-dimensional charge distribution is obtained as a sum of the total charge in the (x-y)-plane for each z coordinate. The result is given in figure 6.31.

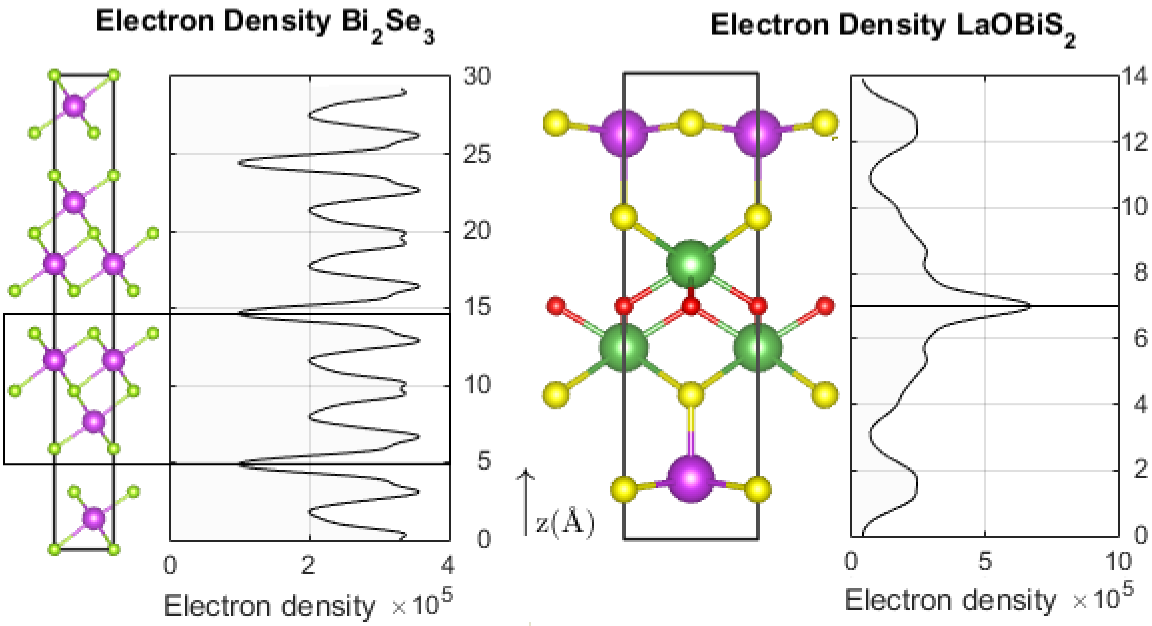

Figure 6.31: Total charge distribution of the bulk Bi_2Se_3 (left) and bulk $LaOBiS_2$ (right) system along the z-axis for the bulk unit cell.

For both materials, the charge distribution within units (QLs) is symmetric around the middle atomic sector. This is a confirmation of the statement made in the theoretical modelling of the crystal in chapter 3, namely that each of the inversion partners within a unit feels an equal in magnitude but opposite in sign electric field. This induces a R-1 or D-1 effect on each inversion partner sector with opposite in sign spin texture, leading to the manifestation of the R-2 or D-2 effect when the crystal is considered in its entirety.

The same visualization can now be made for the Bi_2Se_3 and $LaOBiS_2$ slab systems, to see whether the presence of a surface indeed induces a redistribution of charge that leads to a breaking of the symmetry within the units (QLs). The result is depicted in figure 6.32.

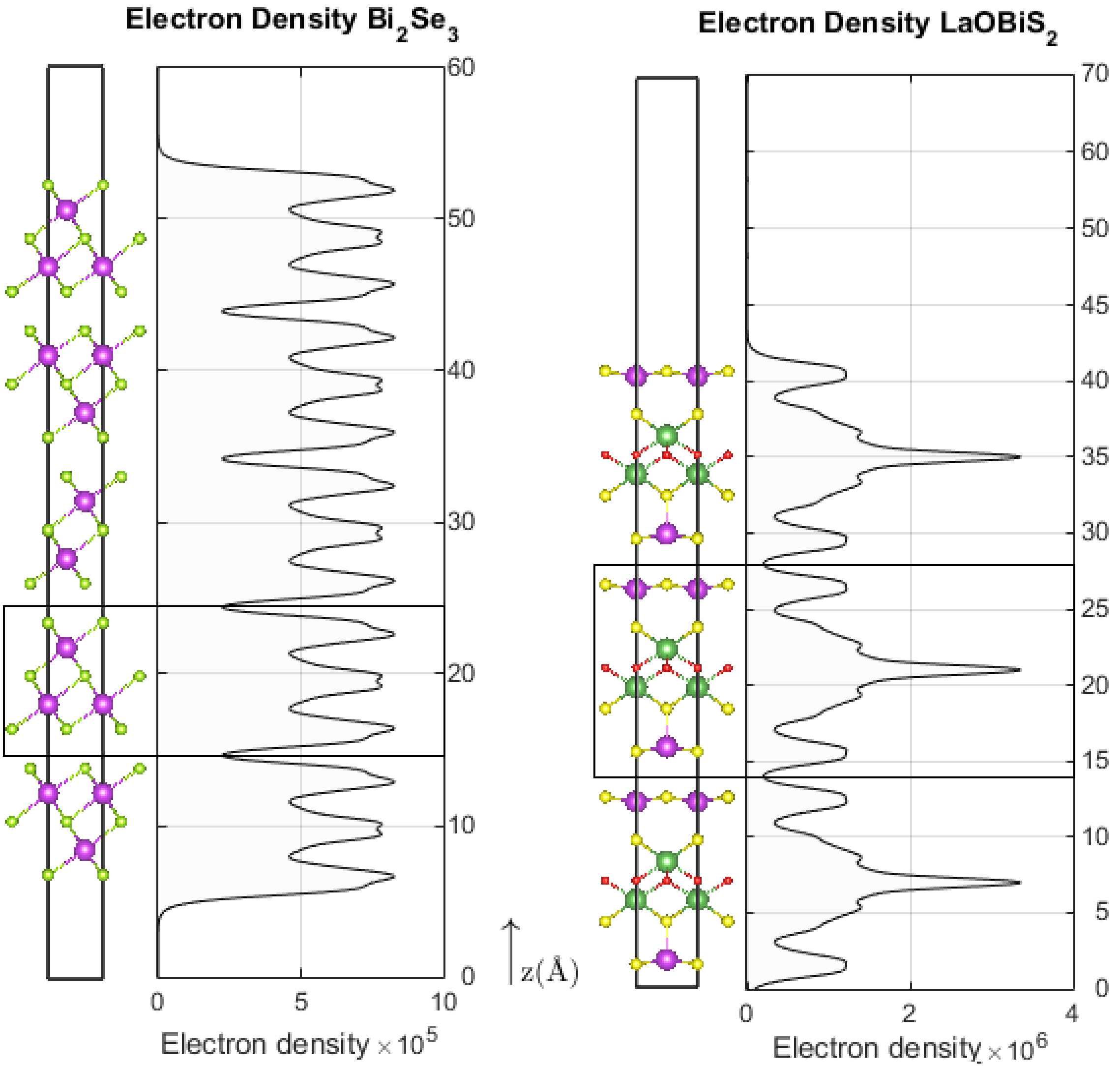

Figure 6.32: Total charge distribution of the slab Bi_2Se_3 (left) and bulk $LaOBiS_2$ (right) system along the z-axis.

From figure 6.32 it seems that the introduction of a surface in the system does not influence the charge distribution at all. The distribution profile along the z-direction of the units for both systems is the same as for the bulk systems in figure 6.31. However, when the different units (QLs) of the slab systems are compared in detail, a difference of one part in thousand between the surface units and the bulk units is observed.

This seems very small, nonetheless it is enough to diminish the hidden spin polarization of the bulk. This is understood by noting that the R-2 and D-2 effect in bulk systems is only present due to the exact symmetry in charge distribution within the units. The electric fields that the inversion partners (atomic sectors) experience are exactly opposite to each other, leading to mutual cancellation when summed over the entire unit. Consequently, even a very small asymmetry in the charge distribution will perturb the mutual cancellation and a net electric field remains.

The net electric field that is induced by the presence of the surface will be parallel to the initial electric field of one of the two inversion partner atomic sectors. The spin texture of the sector of which the initial electric field is parallel to the surface induced electric field will be enhanced.

For example, it can be seen on figure 6.31 that the total charge density distribution for the $LaOBiS_2$ bulk system is largest in the centre of the ten atomic layer unit. Thus, the electric field that is experienced by the inversion partners will point to the middle of the unit. This can be compared with the observation that for the slab system, the charge distribution is slightly more localized on the middle of the three units, leading to a net electric field, pointing to the middle of the slab system. Thus, when the entire slab system is considered, the surface induced electric field within the surface units points in the direction of the outer sectors and enhances the corresponding spin textures. This means that for the top unit, the spin texture of the top sector is adopted and for the bottom unit, the spin texture of the bottom sector is adopted.

This situation is schematically depicted in figure 6.33

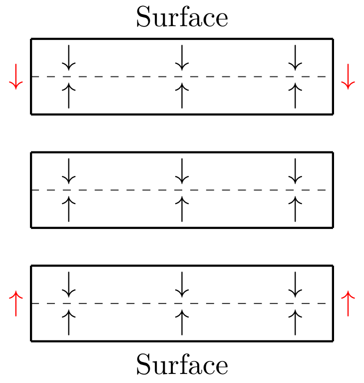

Figure 6.33: schematic representation of the $LaOBiS_2$ slab system. The internal (bulk) electric fields are depicted by black arrows and the surface induced electric fields are depicted by red arrows. Note that the scale of the red arrows is not representative compared to the black arrows.

However, the discussed correspondence of spin textures that this effect would induce, is not in agreement with the DFT calculations. Consequently, the total charge redistribution due to the presence of a surface cannot on its own explain the resulting spin textures of the slab system. As mentioned at the beginning of this section, the localization of the states will turn out to play a much greater role in explaining the net spin polarization in slab systems.

6.5.2 Re-localization of the states

If in the bulk system a surface is introduced, the periodicity of the system will vanish. Because of this, the slab system will have different electronic eigenstates which do not necessarily exhibit the symmetry of the crystal lattice. This can be seen for all the analysed slab systems by looking at the contribution distribution figures throughout previous sections. These figures depict for a specific state, corresponding to one Kohn-Sham level, the contribution of each atomic layer to that state. In other words, they depict the state density in the z-direction of the system. They show on which atomic layers specific states are localized.

For the slab system it can then be argued that the surface units adopt the spin texture of the atomic sector on which it is mainly localized. This localization would overrule the fact that the spin texture of a certain atomic sector is suppressed by the surface induced electric field. This effect explains the discrepancies of the previous section between expected and observed spin textures.

As an example, the slab $LaOBiS_2$ system is again investigated. According to the previous section, for the conduction state, the top unit should adopt the spin texture of the top atomic sector and the bottom unit should adopt the spin texture of the bottom atomic sector. However, comparing figure 4.7-4.9 with figure 6.25 it is clear this is not the case. The reason why this is not the case becomes clear by looking at the density distribution for this state in figure 6.26. It shows that the conduction state is very localized on the inner atomic sectors of the slab units.

This re-localization due to the presence of the surfaces explains why the top/bottom unit adopts the spin texture of the bottom/top atomic sector, respectively. For the valence band the spin texture correspondence is the other way around because it is more localized on the outer atomic sectors, as can be seen on figure 6.29.

The same analysis can be done for the Bi_2Se_3 system with similar results. In this case however, very small deviations from a symmetric charge density distribution over the whole crystal can be observed, which could be ascribed to convergence issues during the calculations.

6.6 Conclusion on slab systems

In this chapter the effect of a surface in a system that shows hidden spin polarization, R-2 and D-2, in its bulk has been investigated. DFT calculations on non-topological slab systems show that the presence of a surface diminishes the R-2 and D-2 effect and consequently induces a net spin polarization within units that lay at the surface of the material. The mechanism behind the vanishing of the hidden spin polarization relies on the breaking of symmetry within the units that contain the inversion partner sectors.

Two effects come into play when a surface is present. The total charge distribution that has a symmetric profile for bulk systems, is influenced by the surface in a way that it becomes asymmetric. This asymmetry within the surface units induces a net electric field that enhances one of the spin textures of the inversion partner sectors.

However, this induced electric field turns out to be three orders of magnitude smaller than the already present electric fields on each of the inversion partners. Nonetheless, the broken symmetry leads to an enhancement of one of the spin textures.

This effect on its own did not predict which spin texture was adopted on either side of the slab system. After some analysis, it is concluded that it is the localization of the specific state on one of the two inversion partner sectors that is decisive on which spin texture is adopted. The predictions by this effect matches the DFT data.

In general both effects will have to be taken into account to explain deviations that cannot be explained by only considering one of the two separately.

An important insight from this chapter is the fact that centrosymmetric materials will exhibit hidden spin polarization inside their bulk in the form of the R-2 or D-2 effect and at the same time show spin-momentum locked surface states. This could be an enormous advantage in the search for spintronic materials.

Chapter 7

Experimental observation and possible applications

Since the publication of the initial papers that predicted hidden spin polarization inside centrosymmetric materials[5],[6], there is a wide interest in experimental detection of this new phenomenon. The first paper about observing these effects reported the detection of large spin polarization in the centrosymmetric MoS_2 bulk crystals[7]. During the writing of this thesis two new papers were published reporting experimental verification of hidden spin polarization in centrosymmetric materials[8],[9].

Here, W.Yao et al.[9] report experimental observation, using spin- and angle-resolved photo emission spectroscopy, of helical spin texture in a monolayer, centrosymmetric $PtSe_2$ film without the characteristic in the conventional Rashba (R-1) effect. However, because they used a monolayer film, surface effects could not be studied and no experimental report has yet been made about surface effects on the R-2 and D-2 effect.

In this rather short part of the thesis some experimental detection techniques will be briefly explained. These techniques are widely used in solid state experiments to directly visualize the band structure of a given material and thus its electronic properties. Since spin plays a crucial role in the R-2/D-2 effects, some techniques to measure spin polarization in solids are also touched upon.

Afterwards some promising applications of spin-orbit effects in spintronics are explored and possible advantages of the R-2 effect over the R-1 effect are stated.

7.1 Observing band structure and spin polarization

To describe the electronic properties of a material in the solid state two main characteristics of its electrons need to be observed. The first is the relation between the electron's (crystal) momentum and its energy, called the dispersion. This leads to the well known band structure of the material from which a great deal of information can be derived. This momentum-energy relation can be experimentally obtained by several methods, though the most commonly used one is ARPES and thus will be explained in more detail.

The second main characteristic of solid state electrons is their spin. The detection of the electrons' spin is even more important concerning the topic of this thesis. One of the main properties of the hidden spin polarization described in this work, is the fact that the spin textures of the electrons are localized on real space sectors within the crystal and are opposite in sign. Consequently, to experimentally verify the existence of these effects, spin polarization detection is needed.

The search for new methods to detect spin polarization of electrons is an active research topic with new papers published frequently[28], however most techniques are based on electron scattering with spin-orbit active atoms such as Au-atoms in gold films. One of these techniques is Mott scattering and will be explained later on.

7.1.1 Angle resolved photoelectron emission spectroscopy

ARPES stands for Angle Resolved Photo Emission Spectroscopy and is a specific type of spectroscopy to produce the band structure of a solid state material by mapping the energy-momentum dispersion of the material's electrons.

The idea behind the technique goes as follows[29] and is depicted in figure 7.1: a beam of photons of known frequency (e.g. synchrotron radiation) impinges the surface of the material. The photo-electric effect states that if the photon's energy $h\nu$ is larger than the electron's work function ϕ, it can knock out the electron from the crystal, where the electron can then be called a photo-electron:

$$E_B = h\nu - \phi - E_k \quad , \tag{7.1}$$

where E_B and E_k are respectively the binding and kinetic energy of the photo-electron. The binding energy of the photo-electron can be calculated by experimentally measuring the kinetic energy of the knocked out photo-electron, once the work function is known.

In order to obtain the electron's initial crystal momentum $(\hbar k_{\|}, \hbar k_{\perp})$ as a function of its energy E_B the polar angle θ of the emitted photo-electron needs to be taken into account. The emitted photo-electron has its initial momentum $(\hbar k_{\|}, \hbar k_{\perp})$ changed when travelling through the surface of the crystal to $(\hbar K_{\|}, \hbar K_{\perp})$ due to the change in potential energy U_0. Here, $(\hbar K_{\|}, \hbar K_{\perp})$ denotes the electron's crystal momentum once it has left the crystal and U_0 is the called the inner potential and is typically defined as the valence band bottom. However, because the crystal has translational symmetry in the direction parallel to its surface, $\hbar k_{\|}$ will not change and thus

$$\hbar k_{\|} \quad \rightarrow \quad \hbar K_{\|} = k_{\|} \tag{7.2}$$

$$\hbar k_{\perp} \quad \rightarrow \quad \hbar K_{\perp} \tag{7.3}$$

With this knowledge and using the fact that $E_k = (\hbar k)^2/2m$ together with (7.1), it is easy to obtain

$$k_{\|} = \sqrt{\frac{2m(h\nu - \phi - E_B)}{\hbar^2}} \sin(\theta), \tag{7.4}$$

and completely analogue for the perpendicular direction, taking U_0 into account:

$$k_{\perp} = \sqrt{\frac{2m(h\nu - \phi - E_B)\cos^2(\theta) - U_0}{\hbar^2}}. \tag{7.5}$$

With these relations it is possible to obtain a relation between the electron's crystal momentum $(\hbar k_{\|}, \hbar k_{\perp})$ and the electron's energy E_B once the kinetic energy E_k and angle of emittance θ are measured.

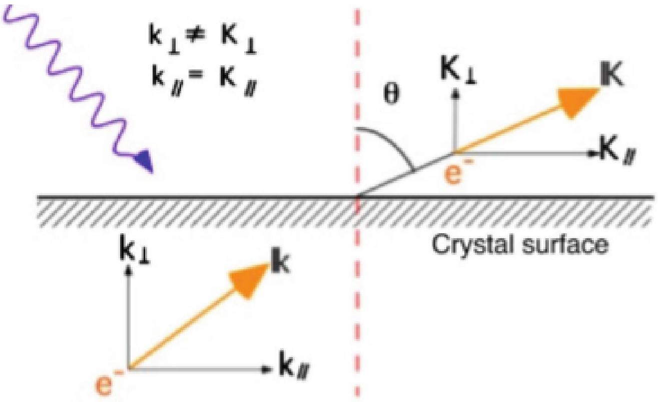

Figure 7.1: A schematic representation of the mechanism behind ARPES[29].

At first sight ARPES seems to only probe to surface of the material, making it a surface technique. This is not something that can be used specifically to experimentally verify the local separation in spin polarization in R-2 materials. However,it has been shown that the mean free path of the electrons inside the material is linked to their kinetic energy[30]. This means that ARPES can be used to probe electrons at tunable debts inside the material, which is needed to verify the localization of spin textures on specific crystal layers.

It needs to be noted that the description of the ARPES mechanism outlined here is a very simplified one. In reality many-body effects need to be taken into account due to the fact that extracting an electron from a crystal will induce an absence of charge which influences not only nearby electrons but also the photo-electron itself while travelling to the surface. These subtleties are extensively documented in corresponding literature[29],[31].

7.1.2 Detecting spin-polarization

As mentioned before, the second main characteristic of electrons in a solid material, and one that is of specific importance when trying to detect the hidden spin polarization effects, is the spin polarization. The photo-electrons emitted by the surface of the material during ARPES should carry information of their spin inside the crystal. Consequently a method is needed to analyse the spin polarization of a beam of electrons.

The Stern-Gerlach experiment with electron beams leads to some troubles which makes it infeasible as a spin splitter device. These troubles arise from the fact that, in contrary to neutral atoms, the electrons will experience a Lorentz force that will deflect the electrons heavily from their initial trajectory.

Instead, the most commonly used technique to split electron beams according to their spin is by scattering them on atoms that exhibit strong spin-orbit effects. Within the spin-obit based detectors two classes can be made, one for high electron energies ($\sim 70keV$) such as the Mott detector and low energetic electron beams ($10 - 100eV$) such as SPLEED and diffuse scattering [29]. Because the photo-electron beams produced by ARPES are usually in the high energy range, the Mott detector is most suitable.

As mentioned, the Mott detector makes use of a spin-orbit effect based scattering process, called Mott scattering, in which the electrons scatter off Au-atoms. These heavy atoms exhibit a large spin-orbit field which interacts with the incoming electrons leading to an asymmetry in scattering angle depending on the electron's spin. This can be understood as follows[29]:

As explained in section 2.1, the incoming electrons experience a Lorentz transformed $\vec{B}$ field due to their motion within the electrostatic field $\vec{E}$ of the Au-atom. This magnetic field can be written as

$$\vec{B} = -\frac{1}{c}\vec{v} \times \vec{E} = \frac{Ze}{cr^3}\vec{r} \times \vec{v} = \frac{Ze}{mcr^3}\vec{L} \quad , \tag{7.6}$$

with Z, e, $\vec{r}$ and $\vec{L}$ respectively the atomic number, electron charge, distance electron-atom and the angular momentum. Here, spherical symmetry of the coulomb potential of the Au atom is explicitly used.

The spin of the incoming electrons will interact with the magnetic field they experience. The magnetic moment associated with the electron's spin is

$$\mu_e = -\frac{g_s e}{2mc}\vec{S} \tag{7.7}$$

with $\vec{S}$ the spin vector of the electron. Consequently, the spin-orbit interaction (V_{LS}) between the electron's spin and the experienced magnetic field can be written as

$$V_{LS} = -\mu_e \cdot \vec{B} = \frac{g_s e}{2mc}\vec{S} \cdot \vec{B} \tag{7.8}$$

Thus, depending on the alignment of the spin and the experienced magnetic field, the electrons will feel a attractive or repulsive interaction potential when scattering on the Au atoms:

$$\begin{aligned} V_{LS} &< 0 \qquad \vec{S} \text{ anti-parallel with } \vec{B}\text{, attraction.} \\ V_{LS} &> 0 \qquad \vec{S} \text{ parallel with } \vec{B}\text{, repulsion. .} \end{aligned} \tag{7.9}$$

Of course the attractive coulomb interaction is still present and will suppress the case where the spin-orbit interaction is attractive.

Due to the vector-product in (7.6), depending on which site of the Au-atom the electron is coming in, it will experience a different $\vec{B}$-field. Taking this into account and the sign of the spin-orbit interaction (7.9), figure 7.2 shows a schematic representation of the scattering process and how the incoming beam of electrons gets spin split.

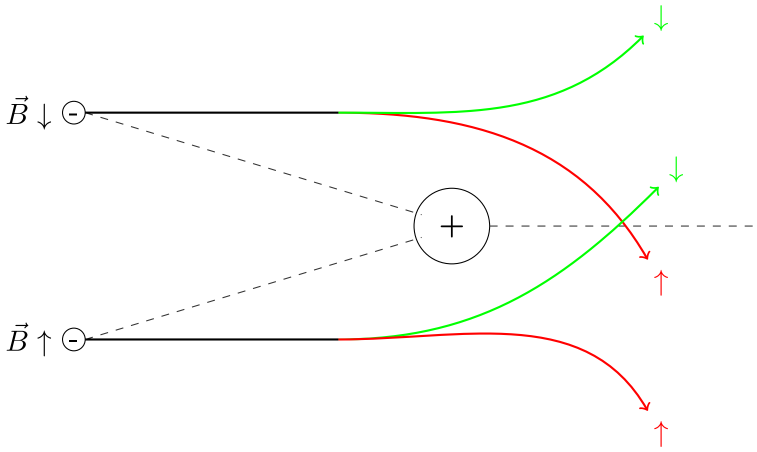

Figure 7.2: Schematic picture of Mott scattering. Here, only the spin-orbit interaction is taken into account. The present attractive coulomb interaction will suppress the repulsive spin-orbit interaction.

7.2 Experimental observation

As mentioned earlier in this chapter, the first experimental observations of the hidden spin polarization in centrosymmetric materials are recently published. In this section those results are briefly discussed.

In the first paper by Gehlmann et al.[7] bulk MoS_2 crystals are experimentally analysed by spin-resolved ARPES measurements. MoS_2 is a layered crystal that consists of weakly bound trilayers consisting of S-Mo-S atomic layers. Gehlmann et al. focussed on the valence band and specifically around the $\bar{K}$ and $\bar{K}'$ points in the projected Brillouin zone because these points are at opposite sides of the BZ and are distinct valleys.

The results show that the band structure of the bulk MoS system is very similar to reported band structures of MoS_2 mono-layers. Gehlmann et al. show that the electronic states are almost completely confined within the atomic layers, meaning that the valence state is strongly localized on those atomic layers. They also directly observed 65% spin polarization of the probed states. However, by taking into account the penetration debt of the probing beam, they argued that the observed spin polarization is a weighed sum of the spin polarization of three MoS_2 tri-layers. With this in mind, they calculated that the spin polarization of one atomic layer would be close to 100%.

Yao et al.[8] report the direct observation of the R-2 effect in a $PtSe_2$ mono-layer on a Pt substrate by means of spin-resolved ARPES. $PtSe_2$ is a layered semiconductor that exists of Se-Pt-Se tri-layers where the Se atomic layers can be considered as inversion partners. The Se atomic site symmetry is C_{3v} and as shown in this thesis, for this symmetry only Rashba spin textures are allowed.

The results show a strong spin polarization (50%) for the four bands along the tangential direction, whereas the spin polarization along the radial or out of plane direction is negligible. Yao et al. note that the helical spin texture cannot be ascribed to a possible structural asymmetry of the substrate, which would lead to a R-1 effect where the four observed valence bands are spin split. Consequently the observed helical spin texture is the signature that the R-2 effect is present.

In a paper published February 2017, Razzoli et al.[9] report a new observation method to directly probe the spin polarization in layered D-2 and R-2 materials. They demonstrate that the observed spin polarization by spin-resolved ARPES can be reversed by changing the handedness of circularly polarized probing photons. In this way, they link the handedness of the polarized light with the spin polarization of the photoelectrons. This gives a new way to selectively address different spin polarizations and thus different sectors inside the material.

7.3 Applications

The major application of spin polarized electrons inside materials is the promising field of spintronics, which could be an extension of the omnipresent field of electronics. Where electronic devices are based on the charge variable of the electrons in solid state materials, the goal of spintronics is to bring the spin variable into the picture.

One of the advantages of using the electrons spin instead of its charge as a working quantity is that spin flipping can occur at a much faster time scale than the motion of the electron as a whole [14]. This leads to faster computations and much less energy dissipation which is a major step forward towards green technology. Pragmatically, working towards feasible spintronic devices also anticipates the possible coming of quantum computers since the latter are build around the concept of superposition of, preferably, spin.

So what is ultimately needed is controllable spin polarization inside conduction materials. For a long time this was achieved by conducting electrons within ferromagnetic materials[32] where the spin is split due to internal magnetic fields. By applying external magnetic fields, the spin of the electrons can be manipulated. However, fine spin manipulation requires very precise magnetic fields, a drawback for these types of ferromagnetic materials.

7.3.1 Advantages of Rashba-spin splitting

A new approach in spintronics has emerged[14],[33] which focusses on the manipulation of spin inside materials by electric fields, instead of magnetic fields. This is realised by intrinsic spin-orbit coupling which couples the motion of the electrons to their spin. As discussed in the beginning of this thesis, in crystals that lack a center of inversion, this is known as the ordinary Rashba (or Dresselhaus) effect.

Using the Rashba effect in inversion asymmetric materials has some crucial advantages over the use of ferromagnetic materials. Because the Rashba effect is due to polar electric fields, it can be tuned by the use of electric fields. The use of electric fields instead of magnetic fields gives better stability, lower power use and possible manipulations at very small scales[14]. Moreover, using the electric Rashba effect enables a switch from magnetic metals to semiconductor materials which are already widely used in electronic devices.

Even though the Rashba spin-splitting in many semiconductors is very small (figure 2.2), leading to cryogenic operating temperatures, recently this obstacle is being overcome by the discovery of large Rashba spin-splitting in specific semiconductors such as Bi_2Se_3 [35].

7.3.2 Advantages of the R-2 effect

Having discussed the major advantages of using the R-1 spin splitting instead of magnetic fields to manipulate spin directions, it is self-evident to now take a closer look at what the advantages could be using the in this thesis analysed R-2 effect.

Most notably is the expansion of possible spintronic materials that can be used for spin splitting. Indeed, the R-2 effect is present in centro-symmetric materials, a class of materials that was hitherto overlooked concerning spin-splitting. The layered materials that are expected to exhibit this hidden spin polarization in the form of the R-2 effect have straightforward design principles[5],[34], making it easy for the experimentalists to search for suitable materials with large spin splitting.

As with the R-1 effect, the internal polar electric fields responsible for the spin splitting in the R-2 effect are at atomic level and can be very large. Since the spin splitting is directly proportional to the magnitude of these polar fields, the corresponding spin splitting will be large as well. For the R-1 effect this poses a problem, rather than a merit, since to influence the spins inside the material, an electric field has to be applied that competes with the strong internal fields. This makes it hard to manipulate the spins sensitively. However, for the R-2 effect this doesn't have to be the case. Since even very small electric fields, or small crystal distortions can lift the compensating character of the spin and thus create a net spin polarization over the whole crystal.

A last advantage of R-2 materials is that they do not produce any external electric or magnetic fields. This is important if such materials are used as components in larger systems, as they will not influence other components in their surroundings.

7.3.3 Advantages of creating a surface

From the analysis on surface systems it became clear that the presence of a surface breaks the R-2 and D-2 effect in the units located near this surface. Spin polarized surface states are induced while in the bulk the hidden spin polarization remains present. This means that if the Fermi level could be raised to conduction band, conducting surface states are obtained without the presence of any external fields. Moreover, the bulk states will remain insulating and the surface states exhibit spin-momentum locking. So, creating a surface effectively results in a centrosymmetric material that shows spin-momentum locking, spin polarized surface states and non-polarized bulk states.

Chapter 8

Conclusion

8.1 Conclusion of the thesis

In the first part of the thesis a theoretical model was constructed based on broad symmetry principles in the form of an effective Hamiltonian that describes C_{2v} and C_{3v} symmetry systems. Theoretical analysis of the model applied on $LaOBiS_2$ (C_{2v}) and Bi_2Se_3 (C_{3v}) confirmed that the model predicts hidden spin polarization for centrosymmetric crystals with a layered structure while maintaining the spin degeneracy of every state. The spin-orbit effects are expressed in the form of Rashba and Dresselhaus spin texture in C_{2v} systems whereas C_{3v} systems could only exhibit Rashba spin texture.

Then DFT calculations on bulk $LaOBiS_2$ and Bi_2Se_3 confirmed the predicted hidden spin polarization, localized on inversion partner sectors. For $LaOBiS_2$ the conduction band exhibited Dresselhaus spin texture whereas the valence band showed Rashba spin texture. Because of the C_{3v} symmetry of Bi_2Se_3 only Rashba spin textures are allowed which is indeed retrieved by the DFT calculations. This confirms that centrosymmetric materials show localized spin polarization on real space sectors. The total spin polarization of the material remains zero due to mutual cancellation between the sectors of the spin polarization.

After the verification of the R-2 and D-2 effect in bulk materials, surfaces were introduced to analyse their effect on the hidden spin polarization. For the topological insulator Bi_2Se_3 the spin-momentum locked surface states are observed through DFT calculations. Those spin polarized surface states meant a vanishing of the R-2 and D-2 effect. It turned out that this phenomenon is not limited to topological insulators but also non-topological slab systems show a vanishing of the hidden spin polarization due to the presence of a surface.

A mechanism that explains this surface effect is described as a combination of charge redistribution and re-localization of the electronic states onto different real space sectors. Both effects destroy the symmetry within unit layers that exhibit R-2/D-2 behaviour in bulk systems and thereby diminishing the hidden spin polarization. Consequently, the presence of a surface induces a net spin polarization at the surface of the material, whereas in the bulk, hidden spin polarization remains present.

During the work on this thesis, the first experimental observations of the D-2/R-2 phenomenon in bulk materials were published. This topic is clearly of great interest due to its possible applications in spintronic research. Hitherto only non-centrosymmetric materials were considered as materials that could be used to couple the spin of the electron to its motion without the use of external magnetic fields. Now, however, a whole new class of centrosymmetric materials becomes available.

8.2 Outlook

In this thesis, analysis of the effect of surfaces on the R-2 and D-2 effect showed that the presence of a surface destroys the hidden spin polarization near the surface of the material. This leads to polarized surface states which exhibit spin-momentum locking whereas the bulk remains to have a zero spin polarization. If the Fermi energy level could be increased to conduction band levels, then materials are obtained that show conducting, spin-polarized surface states and insulator bulk states. These characteristics are similar for topological insulators with the only difference that for the centrosymmetric materials, the surface states are not topologically protected.

The experimental search for this effect in centrosymmetric materials such as $LaOBiS_2$ is called for.

Appendix I

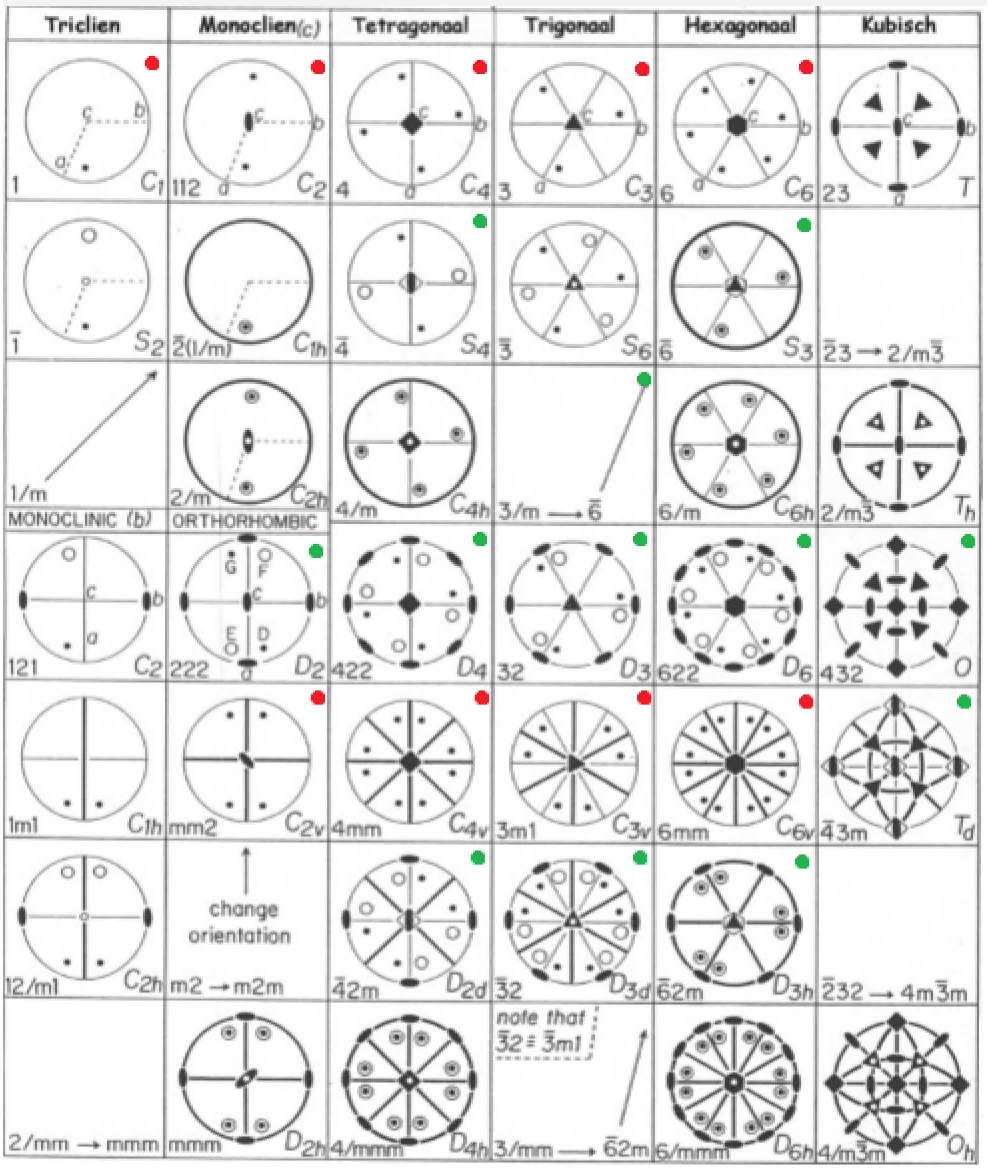

Figure .1: Stereographs of the different point symmetry groups. The symmetry groups that allow for an induced polar field are indicated by a red dot. The symmetry groups that do not allow for polar symmetry are indicated with a green dot.

Appendix II

Full Hamiltonians for LaOBiS$_2$ and its spectrum where both Dresselhaus and Rashba spin orbit effects are considered.

$$H_{BL} = \begin{pmatrix} \epsilon_k & \alpha_R(k_y+ik_x)-\gamma_D(k_y-ik_x) & t_k & 0 \\ \alpha_R(k_y-ik_x)-\gamma_D(k_y+ik_x) & \epsilon_k & 0 & t_k \\ t_k & 0 & \epsilon_k & -\alpha_R(k_y+ik_x)+\gamma_D(k_y-ik_x) \\ 0 & t_k & -\alpha_R(k_y-ik_x)+\gamma_D(k_y+ik_x) & \epsilon_k \end{pmatrix}$$

and

$$E(k) = \epsilon_k \pm k\sqrt{\alpha_R^2+\gamma_D^2+2\alpha_R\gamma_D(\cos(\varphi)^2-\sin(\varphi)^2)+t_k^2} \tag{.1}$$

The full written out 8 × 8 matrix Hamiltonian that models the Bi$_2$Se$_3$ system with coupling on both sides.

$$H_{BL} = \begin{pmatrix} \epsilon_k & -\alpha_R(k_y+ik_x) & u_k & 0 & 0 & 0 & t_k & 0 \\ -\alpha_R(k_y-ik_x) & \epsilon_k & 0 & u_k & 0 & 0 & 0 & t_k \\ u_k & 0 & \epsilon_k & \alpha_R(k_y+ik_x) & t_k & 0 & 0 & 0 \\ 0 & u_k & \alpha_R(k_y-ik_x) & \epsilon_k & 0 & t_k & 0 & 0 \\ 0 & 0 & t_k & 0 & \epsilon_k & -\alpha_R(k_y+ik_x) & u_k & 0 \\ 0 & 0 & 0 & t_k & -\alpha_R(k_y-ik_x) & \epsilon_k & 0 & u_k \\ t_k & 0 & 0 & 0 & u_k & 0 & \epsilon_k & \alpha_R(k_y+ik_x) \\ 0 & t_k & 0 & 0 & 0 & u_k & \alpha_R(k_y-ik_x) & \epsilon_k \end{pmatrix} \tag{.2}$$

Appendix III

To study the $LaOBiS_2$ bulk crystal the all-electron projected augmented wave (PAW) method with the La ($5d^1$), O ($2s^22p^4$), Bi ($6s^26p^3$) and S ($3s^23p^4$) electrons treated as valence electrons. The Perdew-Burke-Ernzerhof (PBE) approximation was used to describe the exchange and correlation interaction. Spin-orbit interaction is explicitly taken into account for the calculations.

The following calculation parameters are used in VASP in order to obtain reliable results. The detailed explanation of these parameters can be found in the VASP manual[22].

- ENCUT = 410, this parameter determines the cut-off energy of the plane-wave basis set in which the wave functions are expanded, in eV. Its value depends on the pseudopotential used for the different atoms in the crystal.
- EDIFF = 1E-10, this parameters is the break-off value which determines when convergence of the self consistent calculations for the charge density is reached. Its value is the difference in energy of two consecutive self consistent calculations.
- NBANDS = 88, this parameter indicates how many bands are calculated, starting with the lowest energy one. It is advised to calculate a few more bands than the highest energetic band that needs to be studied, in order to have proper convergence of the latter band.
- The number of grid points generated to perform the calculation on is important for the precision of the used $\vec{k}$-points. For bulk $LaOBiS_2$ in k_x-, k_y- and k_z-direction: $9 \times 9 \times 9$.

To study the Bi_2Se_3 bulk crystal the all-electron projected augmented wave(PAW)method with the Bi ($6s^26p^3$) and Se ($4s^24p^4$) electrons treated as valence electrons. The PerdewBurke-Ernzerhof (PBE) approximation was used to describe the exchange and correlation interaction. Spin-orbit interaction is explicitly taken into account for these calculations.

The following VASP parameters are used in order to obtain reliable results.

- ENCUT = 320 for the cut-off energy for the plane-wave basis.
- EDIFF = 1E-10 as energy difference cut-off for the self consistent calculations.
- NBANDS = 168 for the number of bands.
- $11\times11\times11$ grid to generate the k-points along the k_x-, k_y- and k_z-direction.

Bibliografie

[1] G. Dresselhaus, Phys. Rev. **100**, 580 (1955).

[2] E. I. Rashba, Sov. Phys. Solid State **2**, 1109 (1960).

[3] K. Ishizaka et al., Nature Materials **10**, 521–526 (2011)

[4] Gabriel Landolt et al., New Journal of Physics **15**, 085022 (2013)

[5] X. Zhang, Q. Liu, J.-W. Luo, A.J. Freeman and A. Zunger, Nat. Phys. **10**, 387 (2014).

[6] Q. Liu, X. Zhang, H. Jin, K. Lam, J. Im, A. J. Freeman and A. Zunger, Phys. Rev. B **91** 235204 (2015).

[7] Mathias Gehlmann et al. , Scientific Reports. **6**, 26197 (2016)

[8] E. Razzoli et al. , Phys. Rev. Letters. **118**, 086402 (2017)

[9] Wei Yao et al. , Nat. Communs. **8**, 14216 (2017)

[10] J. D. Jackson (1962). *Classical Electrodynamics.* New York, NY: John Wiley and Sons, Inc.

[11] J. D. Bjorken & S. D. Drell (1964). *Relativistic Quantum Mechanics.* New York, NY: McGraw-Hill Book Company.

[12] Martin Gmitra and Jaroslav Fabian, *First-principles studies of orbital and spin-orbit properties of GaAs, GaSb, InAs, and InSb zinc-blende and wurtzite semiconductors*, University of Regensburg, 93040 Regensburg, Germany. (2016)

[13] B. Partoens, Nat. Phys. **10**, 333 (2014).

[14] A. Manchon, H. C. Koo, J. Nitta, S.M. Frolov and R. A. Duine, Nat. Mat. **14**, 871–882 (2015)

[15] Yu. A. Bychkov, V. I. Mel'nikov and E. I. Rashba, Zh. Eksp. Teor. Fiz. **98**, 717-726 (1990)

[16] G. Bihlmayer, Lecture Notes of the 45th IFF Spring School *"Computing Solids - Models, ab initio methods and supercomputing"* (Forschungszentrum Jülich, 2014)

[17] J. Fu and J. C. Egues, Phys. Rev. B **91**, 075408 (2015)

[18] M. Gmitra and J. Fabian, Phys. Rev. B **94**, 165202 (2016)

[19] D. Bercioux, Notes on *Spin-orbit interactions in semiconductor nanostructures*

[20] M.S. Dresselhaus, G. Dresselhaus and J. Ado (2002). *Application of Group Theory to the Physics of Solids.* USA, Springer.

[21] Y. L. Chen et al., Science **10**, 325, 178-181 (2009)

[22] Jürgen Hafner, Georg Kresse, Doris Vogtenhuber and Martijn Marsman, Computational Materials Physics, Sensengasse 8/12 A-1090, Vienna, Austria.

[23] A. Miura, Y. Mizuguchi, T. Takei, N. Kumada, E. Magome, C. Moriyoshi, Y. Kuroiwa and K. Tadanaga, Solid State Commun. **227**, 19-22 (2016)

[24] P.D.C. King et al., Phys. Rev. Letters. **107**, 096802 (2011)

[25]H. Zhang,C.-X. Liu, X.-L. Qi, X. Dai, Z. Fang and S.-C. Zhang, Nat. Phys. **5**, 438 - 442 (2009)

[26] R.J. Cava, H. Ji, M.K. Fuccillo, Q.D. Gibson and Y.S. Hor, J. Mater. Chem. C, **1**, 3176-3189 (2013)

[27]H.Aramberri and M.C.Munoz, *Switchable Topological Interface State in Sb2Te3/Bi2Te3 Heterojunctions.* arXiv:1603.01268, march, (2016). [28] A. V. Pradeep et al. , Review of Scientific Instruments. **87**, 023906 (2016)

[29] A. Takayama (2015). *Basic Principle of Photoemission Spectroscopy and Spin Detector.* Tokyo, Springer Japan.

[30] M. P. Seah and W. A. Dench. Quantitative electron spectroscopy of surfaces: A standard data base for electron inelastic mean free paths in solids. Surface and Interface Analysis 1, 2 (1979)

[31] J. Osterwalder, Spin-Polarized Photoemission, Lect. Notes Phys. **697**, 95–120 (2006)

[32] S. A. Wolf, D. D. Awschalom, R. A. Buhrman, J. M. Daughton, S. von Molnar, M. L. Roukes, A. Y. Chtchelkanova and D. M. Treger8, Science mag. Vol. 294, Issue 5546, pp. 1488-1495, (2001)

[33] H. Maass, H. Bentmann, C. Seibel, C. Tusche et al., Nat. Commun. **7**, 11621 (2016)

[34] T. Das and A. V. Balatsky, Nat. Commun. **4**, 1972 (2013)

[35] Z.-H. Zhu et al. , Phys. Rev. Letters. **110**, 216401 (2013)